technische universität
dortmund

Measuring the b-tagging efficiency in ATLAS data at $\sqrt{s} = 8\,\text{TeV}$ and $\sqrt{s} = 13\,\text{TeV}$ using the $p_{\text{T}}^{\text{rel}}$-method

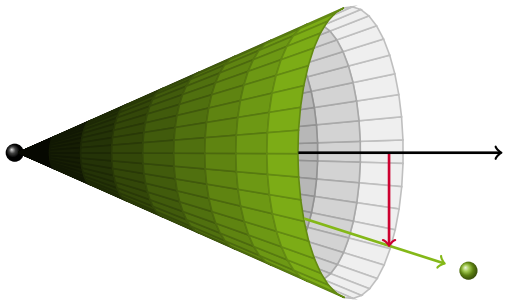

Dissertation
Zur Erlangung des akademischen Grades
eines Doktors der Naturwissenschaften
vorgelegt von:

Dipl.-Phys. Ingo Burmeister

Fakultät Physik
Technische Universität Dortmund
– Dortmund, 2017 –

1. Gutachter:	PD Dr. Reiner Klingenberg
2. Gutachter:	Dr. Johannes Albrecht
Leitung der Prüfungskommission:	Prof. Dr. Manfred Bayer
Wiss. Mitarbeiter in der Prüfungskommission:	Dr. Bärbel Siegmann

Abstract

This thesis presents the first measurement of the b-tagging efficiency ε_b with the $p_{\mathrm{T}}^{\mathrm{rel}}$-method under *Run 2* conditions at the ATLAS experiment. The measurement has been performed for semi-leptonically decaying b-hadrons with a muon in the final state. This has been achieved by selecting events with a muon associated to a jet by a cone based matching algorithm. The $p_{\mathrm{T}}^{\mathrm{rel}}$-variable is sensitive to the mass of the weakly decaying particle and is therefore sensitive to the jet-flavor. Exploiting this dependence, the flavor fractions are determined with a log-likelihood template fit to the $p_{\mathrm{T}}^{\mathrm{rel}}$-distribution in the tagged and untagged jet samples determined by the algorithm and operating point under study. The dataset used for this study corresponds to an integrated luminosity of $11.6\,\mathrm{fb}^{-1}$ of proton-proton-collisions taken with the ATLAS detector at $\sqrt{s} = 13\,\mathrm{TeV}$ center of mass energy.

In addition, ε_b has been measured for algorithms on trigger level using the $p_{\mathrm{T}}^{\mathrm{rel}}$-method. This has been conducted in a set of proton-proton-collisions recorded at the ATLAS experiment at $\sqrt{s} = 8\,\mathrm{TeV}$ center of mass energy. Here, a conditional calibration depending on off-line tagger decisions has been utilized.

Zusammenfassung

In dieser Dissertation wird die erste Messung der b-tagging Effizienz ε_b mit der $p_{\mathrm{T}}^{\mathrm{rel}}$-Methode am ATLAS Experiment unter *Run 2* Bedingungen präsentiert. Die Messung wurde durchgeführt mit semileptonisch zerfallenden b-Hadronen mit einem Myon im Endzustand. Dies wurde erreicht durch Selektion von Myonen in einem Jet Kegel. Die $p_{\mathrm{T}}^{\mathrm{rel}}$-Variable is dabei sensitiv auf die Masse des schwach zerfallenden Teilchens und damit auf den Flavor des Jets. Dieser Zusammenhang lässt sich mit einem log-likelihood Fit ausnutzen um die Flavor-Anteile zu bestimmen, in Datensätzen unterteilt von dem betrachteten Klassifizierungsalgorithmus und Arbeitspunkt. Dies wurde durchgeführt auf einem Datensatz, der einer integrierten Luminosität von $11.6\,\mathrm{fb}^{-1}$ an Proton-Proton Kollisionen entspricht, aufgenommen mit dem ATLAS-Experiment bei einer Schwerpunktsenergie von $\sqrt{s} = 13\,\mathrm{TeV}$.

Zusätzlich wurde die $p_{\mathrm{T}}^{\mathrm{rel}}$-Methode benutzt um ε_b auf Triggerlevel zu bestimmen. Dies wurde durchgeführt auf einem Datensatz von Proton-Proton Kollisionen, aufgenommen mit dem ATLAS-Detektor bei einer Schwerpunktsenergie von $\sqrt{s} = 8\,\mathrm{TeV}$. Hier wurde die Messung abhängig von einer off-line Klassifizierung durchgeführt.

Contents

0. Introduction

In jeden Quark begräbt er seine Nase.

MEPHISTOPHELES

The **S**tandard **M**odel (SM) of particle physics is the theoretical framework, describing our world on the smallest scales currently accessible to men. Characterizing matter and interactions on the most fundamental level, the SM has given us an incredible insight in the functioning of the universe. It has been providing some of the most precise predictions that have ever been experimentally tested. One of the remarkable achievements of the SM is the prediction of the Higgs-mechanism to explain the origin of mass[1] and associated with that the existence of the Higgs-boson [1, 2]. The experimental discovery of this particle and thereby the verification of the Higgs-mechanism is the most outstanding achievement of the LHC experiments so far.

Since the discovery of the Higgs-boson the measurement of its properties is one of the leading efforts of the ATLAS physics program. The detection was mostly driven by the decays into $\gamma\gamma$ and ZZ^* final states due to their clear signature in the detectors [3, 4]. To fully understand the nature of this new particle the direct coupling to fermions has to be measured. The decay channel with the highest **b**ranching **r**atio (BR) is the $b\bar{b}$ final state [5]. The high hadronic activity in the LHC makes this measurement extremely challenging for two reasons. First, the production of two b-jets is a very abundant signature from pure QCD processes. Second, the identification of b-jets is very challenging, because they have to be discriminated against other jet flavors. While the first point can be addressed by selecting processes with additional particles to reduce background, the second point is solved by the utilization of flavor tagging algorithms.

While the t-quark was already discovered at the Tevatron before the start of the LHC [6, 7], top-physics is a field of very broad interest. With the increasing center of mass energy and luminosity, increasingly precise measurements of its properties become achievable. An overview on t-quark physics and current results can be found

[1] This refers to the mass of fundamental particles while the mass of hadrons are largely generated by chiral symmetry breaking.

at [8] including multiple measurements performed by ATLAS in different decay channels. All of these measurements have in common that they exploit the high probability for the t-quark to decay into a b-quark, even before hadronization. Therefore, the top-physics program of the ATLAS experiment heavily relies on the capabilities of flavor-tagging algorithms and how reliably they can distinguish different jet flavors.

Despite the incredible achievements of the SM there are also some challenging issues like the hierarchy problem, the strong CP problem, the matter-antimatter asymmetry in the universe or the nature of Dark Matter or Dark Energy. Models with supersymmetry, **v**ector-**l**ike **q**uarks (VLQs) or extra dimensions are extensions to the SM that try to solve some of the remaining puzzles. There is a variety of **B**eyond **S**tandard **M**odel (BSM) theories with a preference of interactions with the third generation of matter particles for different reasons. As an example models containing VLQs have been proposed to solve the hierarchy problem while stabilizing the Higgs-mass at the same time. Dedicated searches mainly address final states with third generation quarks as discussed in e.g. [9] making flavor tagging capabilities[2] again a driving force of the discovery potential for many BSM models.

As discussed above, there are a lot of physics programs depending on the ability to identify and classify jets with respect to their origin. This is reflected by the extensive efforts put into developing and maintaining flavor tagging algorithms. Within ATLAS this is done by the flavor tagging group. A variety of flavor tagging algorithms has been developed by this group and efforts still continue to improve the existing capabilities. One crucial challenge for the usage of these increasingly complicated algorithms is to exactly evaluate their performance. While it is possible to assess the performance using **M**onte **C**arlo (MC) simulation it is of high importance to have in situ measurements. Within ATLAS dedicated measurements are in place to determine the tagging efficiencies for every algorithm and all flavor hypotheses. Due to the major importance of flavor tagging for a lot of analyses, the flavor tagging group has more than one measurement to determine the performance of tagging algorithms. For the b-tagging efficiency the methods can be separated into t-based and μ-based.

[2]Here classifying jets in boosted environments becomes additionally challenging while also allowing for t-tagging due to increasingly collimated decay products.

There are two μ-based techniques utilized within ATLAS. From the very beginning of data taking with the ATLAS-experiment the system8 and $p_{\mathrm{T}}^{\mathrm{rel}}$-methods have been utilized and are giving reliable measurements. During *Run 1* one outstanding feature of the $p_{\mathrm{T}}^{\mathrm{rel}}$-measurement was also the calibration of algorithms implemented within the **T**rigger and **D**ata **Aq**uisition (TDAQ) system itself. With increasing production rate of final states containing t-quarks, there is a growing amount of t-based techniques available. Due to the importance of flavor tagging for the ATLAS physics program it is important to have independent approaches that rely on different measurements and systematics. In *Run 2*, the $p_{\mathrm{T}}^{\mathrm{rel}}$-method is the only remaining measurement of the b-tagging efficiency not relying on the t-reconstruction, due to the discontinuity of the system8-analysis.

In this thesis, the basics of the $p_{\mathrm{T}}^{\mathrm{rel}}$-techniques are explained. Measurements have been performed in *Run 1* environments for standard off-line tagging algorithms as well as on-line tagging algorithms running on trigger level. One leading focus of this thesis lies on the adaptation of the $p_{\mathrm{T}}^{\mathrm{rel}}$-analysis to *Run 2* conditions and performing a first measurement with a center of mass energy of $\sqrt{s} = 13\,\mathrm{TeV}$. The thesis is structured as follows. In Chapter 1, the theoretical framework of particle physics and its implications with respect to flavor tagging is discussed. The LHC and ATLAS machines used to perform the measurements are described in Chapter 2, while the reconstruction of physics objects is discussed in Chapter 3. One important tool in particle physics are MC simulations which are described in Chapter 4. Chapter 5 is providing an overview on the flavor tagging efforts within the ATLAS Collaboration. This includes different techniques contributing to the measurement of the performance of flavor-tagging algorithms. The utilized event selection and the $p_{\mathrm{T}}^{\mathrm{rel}}$-method itself are discussed in Chapter 6 and 7, respectively. This includes a detailed description of the generation of templates for different flavor hypotheses as well as the fitting procedure. The first measurement performed under *Run 2* conditions and its results are presented in Chapter 8. The systematic limitations and their respective treatment in *Run 1* and *Run 2* are discussed in Chapter 9. Chapter 10 summarizes the efforts made in *Run 1* to calibrate on-line tagging algorithms deployed on trigger level. Finally, the results are summarized and discussed in Chapter 11.

Remarks

In this thesis the following conventions are used[3]:

- Natural units are used, meaning measurements are given in units of physical constants like $\hbar$ or c. Formally this means setting $\hbar = c = 1$ leading to e.g. energy, momentum and mass measurements all having the unit 1 eV.
- The ATLAS coordinate system is used defining a right-handed coordinate system based in the center of the experiment. The x-axis points to the center of the LHC ring, the y-axis points upwards perpendicular to the LHC plane and the z-axis points along the beam axis. Due to the cylindrical shape of the detector it is practical to introduce a respective coordinate system. In cylindrical coordinates the $\phi = \theta = 0$ axis coincides with the x-axis pointing towards the ring center. While the angle θ is defined as the angle in the LHC plane, ϕ represents the angle in the transversal plane around the beam-axis.
- Physics processes are visualized by Feynman-diagrams. In these diagrams the x-axis represents the time line while anti-particles are visualized as particles traveling in the reverse time direction as indicated by the attached arrows.
- The terms *Run 1* and *Run 2* are used throughout this thesis to describe different data taking periods. These are separated by a long shutdown and maintenance period from 2013 until 2014 in which the accelerator as well as the detector went through major upgrades as discussed later. *Run 1* refers to the early LHC data taking with $\sqrt{s} = 7 - 8\,\text{TeV}$ while *Run 2* describes the time after the shutdown with the increased center of mass energy of $\sqrt{s} = 13\,\text{TeV}$.
- In this analysis particles and anti-particles are treated in the same manner without any special separation.

[3] Also note that new chapters are introduced with a quote from Faust by J. W. v. Goethe.

1. The Standard Model of Particle Physics

Daß ich erkenne, was die Welt
Im Innersten zusammenhält

FAUST

The **S**tandard **M**odel (SM) of particle physics is a gauge theory including fundamental forces in form of gauge fields generated by symmetry groups. It is also a **q**uantum **f**ield **t**heory (QFT) describing particles as excited states of the underlying fields. Therefore fundamental matter particles are treated as half-integer-spin fermion states and their interactions are described by the exchange of integer-spin gauge bosons. The SM includes the electromagnetic, weak and strong interactions based on the symmetry groups $SU(3)_{\mathrm{C}} \otimes SU(2)_{\mathrm{L}} \otimes U(1)_Y$, as well as all known matter particles and their respective anti-particles. These particles can be characterized by their mass and quantum numbers as shown in Figure 1.1. The quarks, shown in yellow, as well as the leptons shown in red, are organized in a three-generation structure, also known as families. The gauge bosons are shown in green while the Higgs-boson is highlighted blue. A more detailed discussion can be found in many textbooks and papers like [10].

1.1. Interactions and Gauge Bosons

There are four fundamental forces observed in nature, as listed in Table 1.1. On typical energy scales for particle physics, gravity is much weaker than the other forces and is neglected in the Standard Model. It is expected to be mediated by a spin-2 graviton but neither has it been observed, nor has gravity been quantized in a consistent QFT approach yet. The electroweak and strong interactions are described by the $SU(3)_{\mathrm{C}} \otimes SU(2)_{\mathrm{L}} \otimes U(1)_Y$ symmetry groups. The generators of these gauge groups define the gauge-fields and therefore the properties of the interaction. The electroweak interaction is spontaneously broken $SU(2)_{\mathrm{L}} \otimes U(1)_Y \rightarrow U(1)_{\mathrm{QED}}$ by the Higgs-mechanism which thereby gives mass to the fundamental particles.

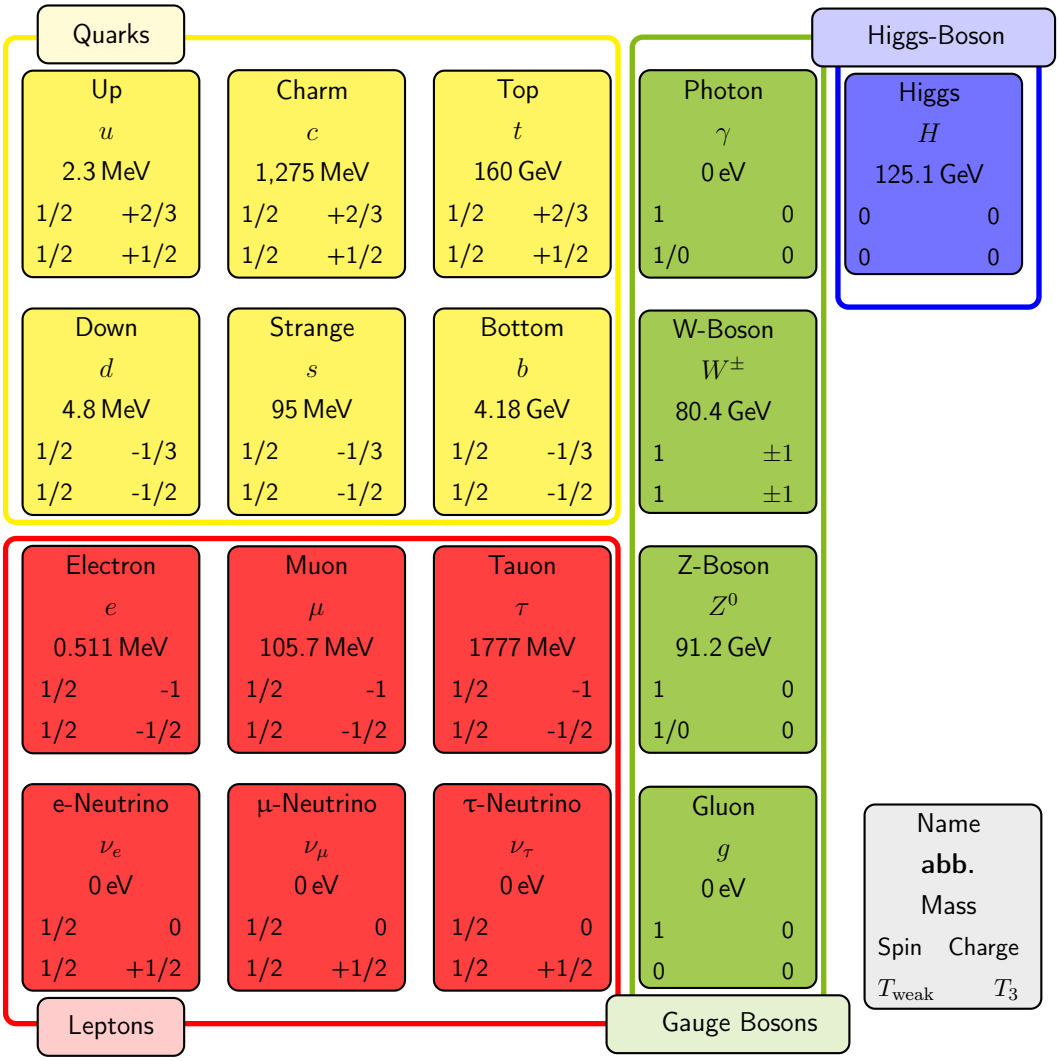

Figure 1.1.: Scheme of the different fundamental particles as described in the Standard Model. The particle name, mass, spin, electrical charge as well as the weak isospin and its third component are listed [11]. The quarks are shown in yellow, leptons in red, gauge bosons in green and the Higgs-boson in blue. The $\overline{\text{MS}}$-mass scheme is quoted for third generation quarks. Neutrinos as well as γ and g are massless in the SM. Uncertainties can be found in [11].

A detailed overview of the SM particles after the symmetry breaking is shown in Figure 1.1. Interactions are mediated by the spin-1 gauge bosons, shown in green, which couple to particles carrying the corresponding charges.

Table 1.1.: Overview over the four fundamental forces, the charge they mediate in between, the range, and their respective gauge bosons. The graviton is expected to be the field quantum of gravity.

Force	Charge	Range	Gauge Boson
gravity	mass / energy	∞	graviton G
electromagnetism	electric charge	∞	photon γ
weak interaction	weak isospin	nucleus	$W^{\pm}$- and Z^0- bosons
strong interaction	color charge	nucleon	gluon g

The electromagnetic interaction is the unification of the electric and magnetic forces and is described in **q**uantum **e**lectro**d**ynamics (QED). Its gauge group $U(1)_{\mathrm{QED}}$ is the remnant of the spontaneous breaking of the electroweak gauge groups. It is mediated by the photon γ which is a massless spin-1 particle coupling to the electric charge e. The vanishing photon mass causes the long range of the interaction.

The strong interaction is based on $SU(3)_{\mathrm{C}}$ and described by **q**uantum **c**hromo**d**ynamics (QCD). It is mediated between color charged objects by eight massless gluons g. There are three different color charges red, green and blue and their respective anti-colors. QCD is a non-abelian theory introducing self-coupling terms for the gauge fields. This means that gluons themselves are color charged objects, carrying a color and an anti-color. Due to this self-interaction, the strong interaction gets stronger for greater distances and weaker for short distances, leading to asymptotically free particles at high energies. For increasing distances the field strength between color charged particles rises up to a point where the energy of the field is high enough to create new color charged particles out of the vacuum. Subsequently generating two color neutral particles which are each built up from color charged partons. This means that color charged particles can only be observed in confined, color neutral hadrons. Among such color neutral hadrons there is still a remaining force based on the strong interaction, which, for example, is the force binding the nucleons in the nucleus.

The weak interaction is mediated by the massive $W^{\pm}$- and Z^0-bosons which couple to the third component of the weak isospin T_3. Since the exchange of off-shell particles is suppressed by the mass term in the propagator, the resulting force is short ranged and thus it appears much weaker than the other interactions.

Since the $W^{\pm}$-bosons carry an electric charge as well as a weak isospin, the weak **C**harged **C**urrent (CC) is the only interaction able to change the nature of a particle, by changing electric and weak charges and also causing family transitions. Left-handed fermions as well as right-handed anti-fermions form weak isospin doublets with $(T_{\text{weak}}, T_3) = (\frac{1}{2}, \pm\frac{1}{2})$ while the right-handed fermions and left-handed anti-fermions form weak isospin singlets $(0, 0)$. Due to this structure a combination of parity P and charge conjugation C has to be used to transform between particles and anti-particles

$$\begin{pmatrix} \nu_e \\ e^- \end{pmatrix}_{\mathrm{L}}, \left(e^-\right)_{\mathrm{R}} \quad \overset{CP}{\longleftrightarrow} \quad \begin{pmatrix} \overline{\nu}_e \\ e^+ \end{pmatrix}_{\mathrm{R}}, \left(e^+\right)_{\mathrm{L}}. \tag{1.1}$$

The weak interaction and the electromagnetism are remnants from the electroweak symmetry breaking of the electroweak interaction which is described by the weak isospin and hypercharge gauge groups $SU(2)_{\mathrm{L}} \otimes U(1)_Y$ with the respective gauge bosons $\mathrm{W}_{1,2,3}$ and B. This symmetry breaking results in the observed gauge boson states γ, Z^0 and $W^{\pm}$. The electroweak fields combine to the weak CC bosons

$$\begin{pmatrix} W^+ \\ W^- \end{pmatrix} = \frac{1}{\sqrt{2}} \begin{pmatrix} 1 & \mathrm{i} \\ 1 & -\mathrm{i} \end{pmatrix} \begin{pmatrix} W_1 \\ W_2 \end{pmatrix}, \tag{1.2}$$

as well as to the bosons of the electromagnetic interaction and the weak **N**eutral **C**urrent (NC)

$$\begin{pmatrix} \gamma \\ Z^0 \end{pmatrix} = \begin{pmatrix} \cos\theta_{\mathrm{W}} & \sin\theta_{\mathrm{W}} \\ -\sin\theta_{\mathrm{W}} & \cos\theta_{\mathrm{W}} \end{pmatrix} \begin{pmatrix} \mathrm{B} \\ \mathrm{W}_3 \end{pmatrix}, \tag{1.3}$$

with the Weinberg-angle θ_{W} given as

$$\cos\theta_{\mathrm{W}} = \frac{M_W}{M_Z}. \tag{1.4}$$

In general, these interactions are of a vector minus axial-vector (V-A) structure expressed by the current J^μ which is proportional to

$$J^\mu \quad \propto \quad \overline{\psi}_f G\gamma^\mu(c_\mathrm{V} - c_\mathrm{A}\gamma^5)\psi_i, \tag{1.5}$$

with the Dirac-matrices γ^μ and the initial and final fermion states ψ. The coupling constant G is characteristic for each interaction while the charge parameters $c_{\mathrm{V/A}}$ also depend on the particle charges. An overview of these parameters is given in Table 1.2 with the weak coupling strength $g = e/\sin\theta_\mathrm{W}$.

Table 1.2.: Coupling parameters for the electromagnetic and weak interactions.

Interaction	G	c_V	c_A
electromagnetism	e	Q	0
neutral current	$g/\cos\theta_\mathrm{W}$	$T_3 - Q\sin^2\theta_\mathrm{W}$	T_3
charged current	g	T_3	T_3

This generates a purely vector-like electromagnetic interaction ($c_A = 0$) that only couples to the electric charge Q. The weak interaction has an axial-vector contribution where the CC acts on the weak isospin only, while the NC couples to the electric charge, too.

1.2. The Higgs Sector

In the Standard Model explicit mass terms for the fundamental particles are forbidden by the underlying gauge principles. Since massive particles are observed in nature the Higgs-mechanism is used to generate massive particles by introducing a new weak isospin doublet ϕ with a potential $V(\phi)$, as shown in Figure 1.2, of the form

$$V(\phi) \quad = \quad \mu^2\phi^\dagger\phi - \frac{\lambda^2}{2}(\phi^\dagger\phi)^2, \tag{1.6}$$

with parameters $\lambda^2 > 0$ and $\mu^2 > 0$. This field has a non-vanishing vacuum expectation value $v = |\mu/\lambda|$. This means that the field does not vanish in the ground state. In other words, the lowest energy state for the vacuum is a state where a Higgs-condensate is present.

The non-vanishing vacuum expectation value spontaneously breaks the electroweak symmetry, introducing mass-terms to the Lagrangian. Since the $U(1)_{\mathrm{QED}}$-symmetry is preserved it is possible to pick a gauge such that the $W^{\pm}$- and Z^0-bosons become massive while the photon stays massless.

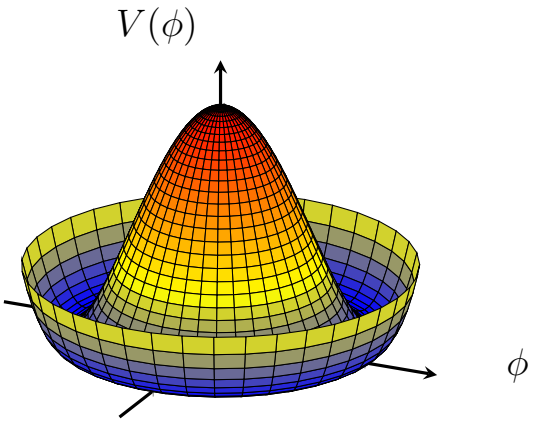

Figure 1.2.: Higgs-potential $V(\phi)$ drawn for different values of the complex field ϕ. The potential has its minimal values for non-vanishing values of ϕ. It is symmetric under rotation in the complex plane, but the ground state is not.

One inference from the Higgs-mechanism is the existence of at least one massive scalar particle. This was named the Higgs-boson and proving its existence was one of the major goals of the LHC physics program. On July 4^{th} 2012 the ATLAS and CMS experiments announced the observation of a Higgs-like particle with about 5σ significance, each [3, 4]. For the theoretical prediction [1, 2], Peter W. Higgs and François Englert were awarded with the Nobel price in physics 2013 [12]. Measuring the properties of this particle is one of the leading efforts of the two LHC experiments ATLAS and CMS.

1.3. Quarks

Quarks are spin-1/2-fermions (shown in yellow in Figure 1.1) carrying a red, green or blue color charge. They also carry an electric charge and a weak isospin. Hence, they couple to all gauge bosons. The strong interaction causes asymptotically free quarks to hadronize into color neutral particles like mesons, consisting of a quark and an anti-quark, or baryons, consisting of three quarks. Therefore, quarks carry the additive baryon number 1/3. Quarks come in three weak isospin doublets[4] known as generations or families. They are sorted with increasing mass up to the top-quark.

In high energy particle physics, the u, d and s quarks are considered massless and referred to as light quarks. Hadrons are strongly interacting particles composed of the valence quarks generating their quantum numbers and a sea of virtual quarks and gluons which are produced and annihilated in vacuum fluctuations and which generate most of the hadron mass. The valence quarks, sea quarks and gluons are referred to as partons.

1.3.1. The CKM-Matrix

The spontaneous breaking of the electroweak symmetry introduces quark mass terms with non-diagonal mass-matrices. Therefore, the strong eigenstates which also are eigenstates of mass are a linear combination of weak eigenstates. Hence the strong quark states ψ_q are transformed into a superposition of weak eigenstates $\psi_{q'}$ by a unitary matrix U_q. This is performed independently for up- and down-type quarks with the respective matrices $U_{u/d}$. Transforming initial and final state in the current J^μ (see Equation (1.5)) results in two possible outcomes depending on the type (up or down) of the initial and final quark state

$$U_u^\dagger U_u = U_d^\dagger U_d = 1 \qquad \text{or} \qquad U_u^\dagger U_d = V. \tag{1.7}$$

While for the NC the transformations in initial and final state cancel each other out, a non-diagonal contribution remains for the CC, introducing the **C**abibbo-**K**obayashi-**M**askawa (CKM)-matrix V. Thereby the CC not only converts a quark into its isospin partner but can also cause a transition between generations. The CKM-matrix is typically referred to as a single transformation:

[4] Only the left-handed quarks form doublets which is then generalized as a quark generation.

$$\begin{pmatrix} d' \\ s' \\ b' \end{pmatrix} = \begin{pmatrix} V_{ud} & V_{us} & V_{ub} \\ V_{cd} & V_{cs} & V_{cb} \\ V_{td} & V_{ts} & V_{tb} \end{pmatrix} \begin{pmatrix} d \\ s \\ b \end{pmatrix}. \tag{1.8}$$

For example, a t-quark which decays via the weak interaction is a linear combination of the weak states t', c' and u' and can decay into each of their respective weak isospin partners. The occurring decay vertex is proportional to the respective CKM matrix element V_{ij}. Currently, these parameters are measured to the absolute values [11]

$$|V_{\mathrm{CKM}}| = \begin{pmatrix} 0.97425 \pm 0.00022 & 0.2253 \pm 0.0008 & (4.13 \pm 0.49) \cdot 10^{-3} \\ 0.225 \pm 0.008 & 0.986 \pm 0.016 & (41.1 \pm 1.3) \cdot 10^{-3} \\ (8.4 \pm 0.6) \cdot 10^{-3} & (40.0 \pm 2.7) \cdot 10^{-3} & 1.021 \pm 0.032 \end{pmatrix}. \tag{1.9}$$

Since the off-diagonal elements are much smaller than unity, all transitions between families are suppressed by the respective matrix element squared $|V_{ij}|^2$. Consequently a top quark almost exclusively decays into b-quarks. Rendering b-hadrons an important signature for all processes involving top quark final states.

1.3.2. Parton Distribution Functions and Hadronization

In hadron collisions at high energies, the partons collide in the hard interaction. The parton density depends on the momentum transfer and is described by the **P**arton **D**istribution **F**unction (PDF) $f_i(x, Q)$. The PDF gives the probability of finding a certain parton i with a specific fraction x of the total hadron momentum at an energy scale Q. In Figure 1.3 the HERAPDF1.5 is shown for a typical **L**arge **H**adron **C**ollider (LHC) energy scale of $Q = 100\,\mathrm{GeV}$ [13].

In the hard scattering process, new particles can be created. In case of strongly interacting particles, hadrons are formed which can be categorized by the flavor of their most massive valence quark. Due to the high momentum transfer a cascade of collimated hadrons are generated, forming particle jets. These jets can also be labeled by the flavor of the most massive quark in the jet.

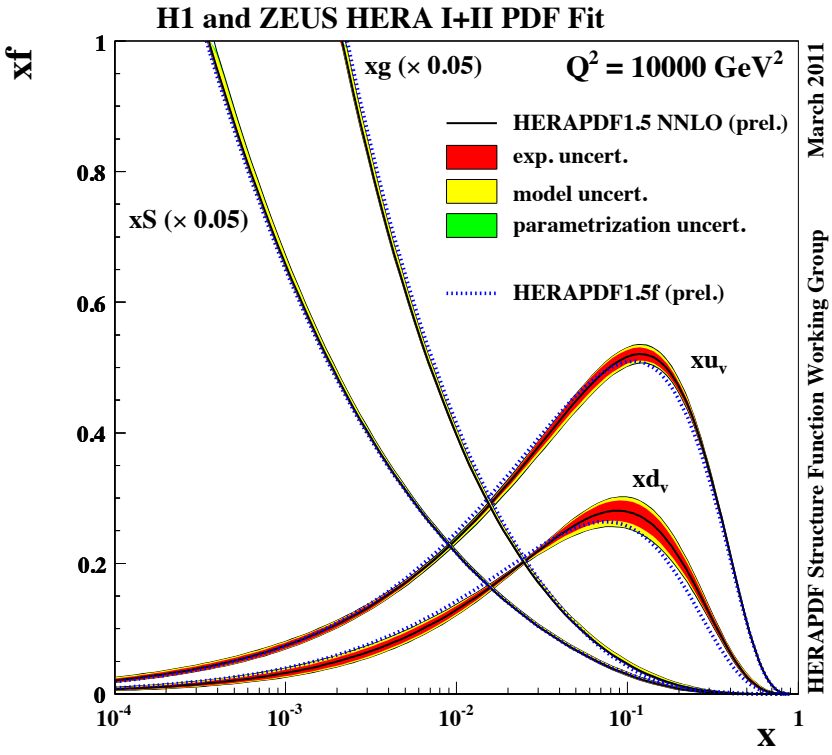

Figure 1.3.: The parton distribution functions from HERAPDF1.5 is shown at an momentum transfer of $Q = 100\,\text{GeV}$ [13]. The contribution of the valence quarks is shown as xd and xu. The gluon and sea contributions are scaled down by a factor of 20 and labeled xg and xS respectively.

1.4. Leptons

Spin 1/2-fermions that do not interact strongly are called leptons (shown in red in Figure 1.1). They come in three families or flavors e, μ and τ. Each family consists of a left-handed isospin doublet of one electrical charged lepton and the corresponding neutrino, and a right-handed singlet charged lepton. Neutrinos only interact via the weak force while charged leptons also interact electromagnetically. Weak flavor eigenstates are a linear combination of mass eigenstates. This means that for the time evolution of neutrinos, the flavor states have to be transformed into mass states[5]. This results in mass states that are a mixture of flavor eigenstates whose composition

[5] Alternatively, the time evolution operator, and therefore the Hamilton-operator, can be transformed into flavor space.

changes during propagation. This is called neutrino flavor oscillation. It is similar to the CKM mixing in the quark sector but the mixing matrix, known as the **P**ontecorvo-**M**aki-**N**akagawa-**S**akata-(PMNS)-matrix, is different. For neutrinos to mix in such a way it is inevitable that the neutrinos have different masses. As a consequence at least two neutrinos must have a non-vanishing mass. For their contribution to neutrino oscillation research and thus for the proof that neutrinos have mass Takaaki Kajita and Arthur B. McDonald were awarded with the Nobel price of physics in 2015 [14].

1.5. Beauty-Hadrons

For this analysis the b-quark and its hadrons are of particular interest. The b-quark is referred to as bottom- or beauty-quark[6] with the respective quantum number bottomness or beauty $B = -1$. B is conserved in the electromagnetic and strong interactions. General examples for physics processes with b-hadrons as an important signatures are the decay of the t-quark, which almost exclusively decays into bW. For the Higgs-boson the b-quark is the heaviest fermion the Higgs can decay into, as shown in Figure 1.4. Since the mass of a particle is a measure for its coupling strength to the Higgs field, the process $H \to b\bar{b}$ has the largest **b**ranching **r**atio (BR) of all Higgs-decay modes[7] [5].

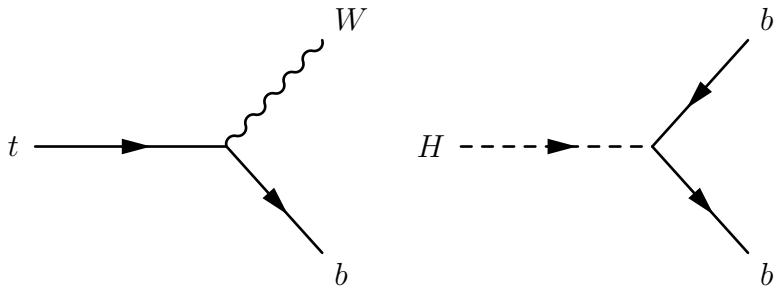

Figure 1.4.: Feynman diagrams for b-quarks produced in decays of t-quarks (left) or Higgs-bosons (right).

[6] In the latter case the top-quark is often also referred to as the truth-quark.
[7] The decay into vector bosons is suppressed by one boson being off-shell in the final state.

1.5.1. b-Hadron Production at Hadron Colliders

In high energetic proton-proton collisions, the b-quark can be produced by a variety of physics processes. In the hard scattering process, two partons of the respective protons collide according to the PDF of the proton. Due to the low probability of a b-quark existing in the sea, it is most probably produced by gluon fusion or quark anti-quark annihilation in the hard scattering process as shown in Figure 1.5.

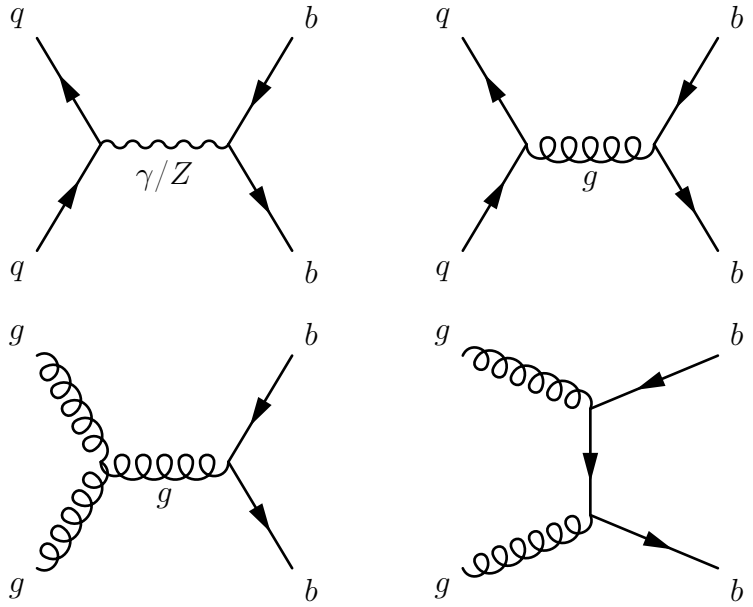

Figure 1.5.: Examples of Feynman-diagrams for b-quark pair-production in parton parton collisions. Shown are quark anti-quark annihilation on the top and gluon fusion below. These are just example diagrams on tree-level.

The overall b-hadron production fractions expected at a collider like the LHC have been measured at Tevatron. In addition Z^0-decays are expected to give a good estimate to the production fractions expected in high energy proton-proton collisions. Table 1.3 shows an overview of the b-hadron production fractions as obtained from Z^0-decays compared to inclusive measurements done at Tevatron and the combination performed by the **H**eavy **F**lavor **A**veraging **G**roup (HFAG) using results from LEP, Tevatron and LHCb [15].

Table 1.3.: Fractions of b-hadrons as produced in Z^0-decays, inclusive measurements performed at Tevatron, and compared to the average provided by the HFAG [15].

Hadron Fraction	Z^0-decays	Tevatron	HFAG-combination
B^+ fraction	0.410 ± 0.007	0.350 ± 0.020	0.406 ± 0.005
B^0 fraction	0.410 ± 0.007	0.350 ± 0.020	0.406 ± 0.005
B_s^0 fraction	0.100 ± 0.008	0.100 ± 0.010	0.105 ± 0.005
b-baryon fraction	0.080 ± 0.010	0.199 ± 0.044	0.083 ± 0.010

1.5.2. b-Hadron Decay Properties

Due to the b-mass being significantly larger than that of all the lighter quarks, the decay of b-hadrons can be considered as the decay of the b-quark within the presence of a spectator quark. The b-quark decays almost exclusively into a c-quark and a W-boson as shown in Figure 1.6, while the decay into an u-quark is suppressed by the CKM-matrix. Therefore, the lifetimes of the various b-hadrons are very similar and all in the order of $\mathcal{O}(1\,\mathrm{ps})$. For the most prevalent B-mesons, the lifetime is $\tau(B^0) \approx (1.520 \pm 0.004)\,\mathrm{ps}$ or $\tau(B^\pm) \approx (1.638 \pm 0.004)\,\mathrm{ps}$ [15]. With the relativistic flight length l being dependent on the particle momentum p one finds

$$\begin{aligned} l_B(p) &= \beta(p) \cdot \gamma(p) \cdot c \cdot \tau_B \\ &= p \cdot \frac{c \cdot \tau_B}{m_B}. \end{aligned} \tag{1.10}$$

For a B^0 with $m_{B^0} = (5279.58 \pm 0.17)\,\mathrm{MeV}$ [11] and a momentum of $p = 50\,\mathrm{GeV}$ the expected flight length is

$$l_{B^0}(50\,\mathrm{GeV}) \cong 4.3\,\mathrm{mm}. \tag{1.11}$$

Therefore, b-hadrons fly a measurable distance before decaying. This leads to distinguishable features like a spatially separated decay vertex and high impact parameters. These signatures can be exploited in multiple flavor-tagging techniques as discussed in Chapter 5.

The off-shell W, produced in the b-decay, can itself decay into multiple particles. In this thesis, decays with a muon in the final state are of particular interest as shown in Figure 1.6. The BRs for charged and neutral B-mesons into $\mu\nu_\mu X$ final states are $(10.99 \pm 0.28)\,\%$ and $(10.33 \pm 0.28)\,\%$ respectively [11]. This means that roughly one tenth of b-hadrons decay by producing a muon. Only such events are used for the $p_{\mathrm{T}}^{\mathrm{rel}}$-method as described in Chapter 7.

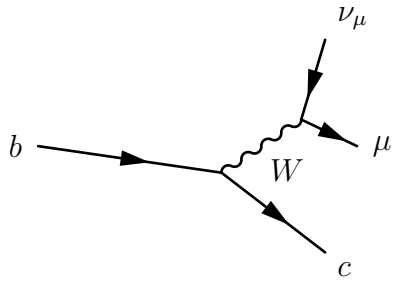

Figure 1.6.: Semileptonic b-decay with a muon in the final state.

2. CERN, LHC and the ATLAS Experiment

Und mit geheimnißvollem Trieb,
Die Kräfte der Natur rings um mich her enthüllen.

FAUST

2.1. The Large Hadron Collider at CERN

Founded in 1954 the "Conseil Européen pour la Recherche Nucléaire" CERN was one of the first international scientific organizations in Europe after World War 2. Nations who fought against each other only a few years before joined forces in an attempt to better understand the most fundamental building blocks of our universe. In July 2016 CERN welcomed Romania as its 22nd member state [16, 17]. Over the decades CERN experiments have unveiled major parts of what we now know as the Standard Model of particle physics.

The **L**arge **H**adron **C**ollider (LHC) took heritage on decades of ground breaking scientific discoveries and leading edge science done at CERN. It is currently the main project at CERN and the most powerful particle accelerator ever build by mankind. Starting from 1989 the **L**arge **E**lectron **P**ositron Collider (LEP) reached center of mass energies of 209 GeV in its eleven years of operation. This was achieved by constructing a 26.7 km long tunnel passing between 45 m and 170 m below the surface at the border of France and Switzerland. This tunnel was then refurbished and reused for the LHC machine [18].

Starting from a single bottle of hydrogen gas there are several steps in the proton accelerator chain as shown in Figure 2.1. Protons are extracted from the hydrogen gas by stripping of the electrons using a charged foil. The linear accelerator LINAC2 then injects the protons at a sub-GeV energy into the **P**roton **S**ynchrotron **B**ooster (PSB) which consists of four synchrotron rings accelerating four bunches of protons to 1.4 GeV in parallel. The four bunches are combined to one bunch with higher

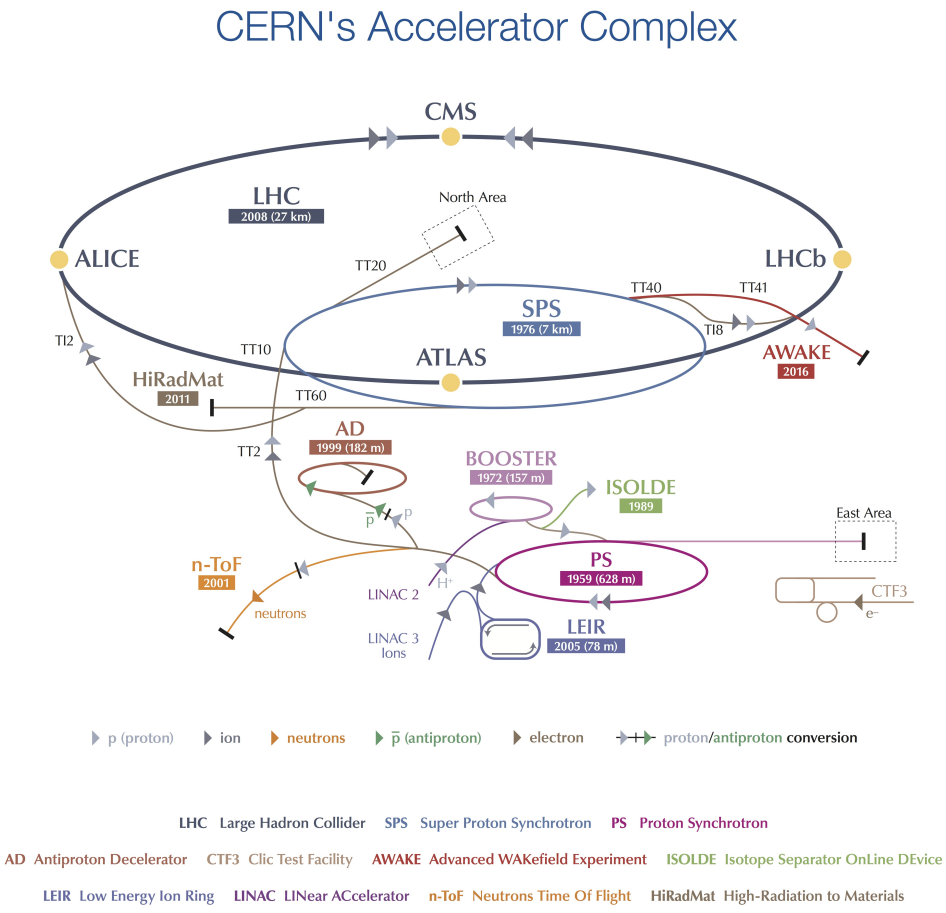

Figure 2.1.: Schematic view of the CERN accelerator complex [19]. The LHC is drawn in blue with the four major experiments shown as yellow dots. The positions are not accurate representation.

intensity and fed into the **P**roton **S**ynchrotron (PS) which then accelerates them to 25 GeV before feeding the proton packet in the **S**uper **P**roton **S**ynchrotron (SPS) where they are accelerated to 450 GeV. The last accelerator stage is the LHC storage ring itself. Built in the former LEP tunnel the LHC had physical constraints on its size. The tunnel has a diameter of 3.7 m and therefore a twin-bore magnet system was chosen rather than two separated proton rings. Using the lighter electrons LEP had more straights and tighter arcs as would be ideal for a proton synchrotron. This Challenge was met by the usage of super-conducting magnets. This way the LHC is capable of accelerating protons reaching a beam energy of currently 6.5 TeV per

proton[8]. These beams are circulated clockwise and counter clockwise in the ring and brought to collision at the four experiments ATLAS, CMS, ALICE and LHCb. [18]

The beam energies reached by the LHC increased during its operation. Starting with a center of mass energy $\sqrt{s}$ of 7 TeV in 2011 the LHC was then operated with $\sqrt{s} = 8$ TeV in 2012 and afterwards upgraded to the current conditions of $\sqrt{s} = 13$ TeV. This is planed to be increased to its design value of $\sqrt{s} = 14$ TeV in the future.

2.2. The ATLAS Experiment

The ATLAS experiment is a multipurpose particle detector located at one of the interaction points of the LHC proton synchrotron. The name ATLAS originally came from the acronym **A** **T**oroidal **L**HC **A**pparatu**S**. Consisting of different layers of specially designed detector components as shown in Figure 2.2 it has almost full angular coverage around the interaction point. The detector can broadly be described as consisting of four parts measuring specific properties of the collision remnants. The innermost part or **I**nner **D**etector (ID) is focused on high resolution reconstruction of particle tracks which is important for resolving the interaction vertices. Around that the electromagnetic calorimeter is measuring electrons and photons while the hadronic calorimeter is detecting hadronic particles and jets stopping the remaining particles except for muons. Despite neutrinos which leave the experiment undetected only muons pass the calorimeters and are then measured in the **M**uon **S**pectrometer (MS), the most outer layer of the detector.

2.2.1. Inner Detector and Insertable B-Layer

In order to reconstruct particle tracks and interaction vertices the Inner Detector is placed as close to the interaction region as possible. Figure 2.3 shows a cut away picture of the Inner Detector system of ATLAS. It has a total length of 6.2 m and is 2.1 m in diameter consisting of multiple subsystems which each have a cylindric barrel region and two end-cap regions with detectors perpendicular to the beam axis.

The detector part closest to the interaction region is the pixel detector. The pixel detector as shown in Figure 2.4 consists of three barrel layers of silicon pixel sensors

[8]It is also capable of accelerating lead ions but in this thesis emphasis is put on proton proton collisions.

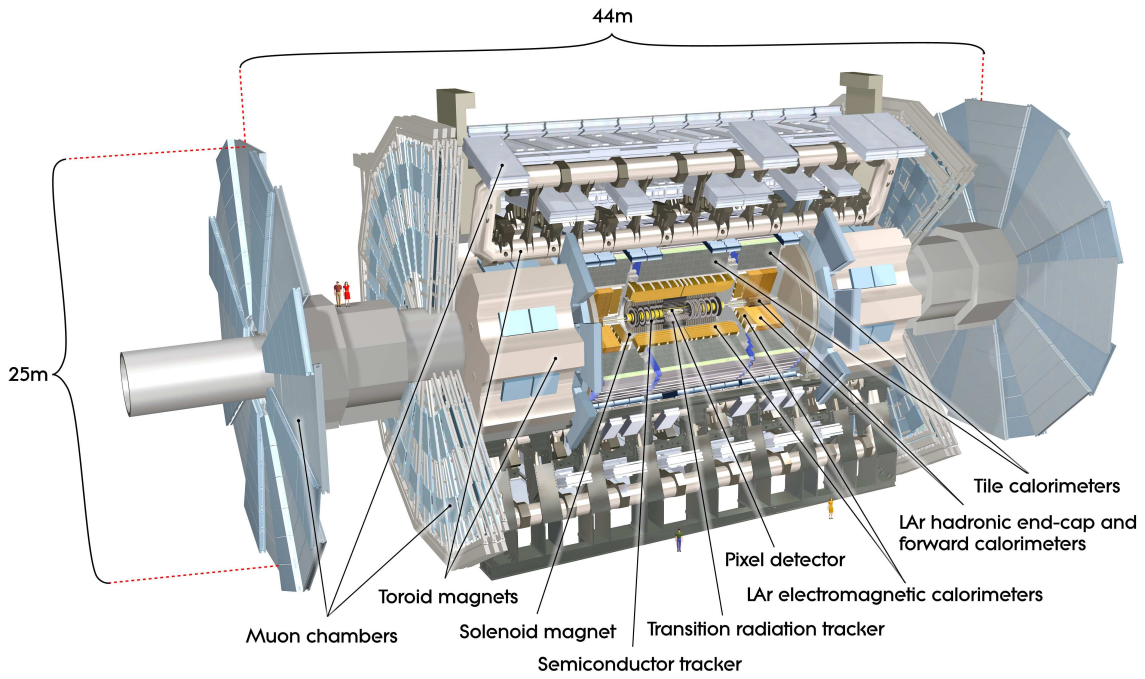

Figure 2.2.: Cut-away schematic of the ATLAS detector [20]. Pixel detector, semiconductor tracker and the transition radiation tracker make up the inner detector which is surrounded by the solenoid magnet. The LAr electromagnetic calorimeter, LAr hadronic end-cap and forward calorimeters and the tile calorimeters enclose the inner detector. The outermost part is the toroid magnet system and the muon chambers.

on concentric cylinders surrounding the beam line at mean radii of 122.5 mm, 88.5 mm and 50.5 mm. It also has two times three end-cap disk layers perpendicular to the beam axis covering scattering angles up to $|\eta| < 2.5$. It provides a resolution of about 15 µm for the transverse impact parameter and of about 1 mm in the longitudinal z-coordinate vertex reconstruction. This is achieved by 1456 silicon sensor modules in the barrel and 288 modules in the end-cap discs adding up to a combined active detector area of 1.73 m^2 with about 80 million readout channels. [21]

The capabilities of identifying b-flavored jets highly depend on these vertex resolutions. The innermost barrel layer has the biggest influence on these resolution capabilities and is hence called B-Layer.

In the **L**ong **S**hutdown period 1 (LS1) in the years 2013 and 2014 the IBL was added as the innermost detector layer as shown in Figure 2.5. This was possible due

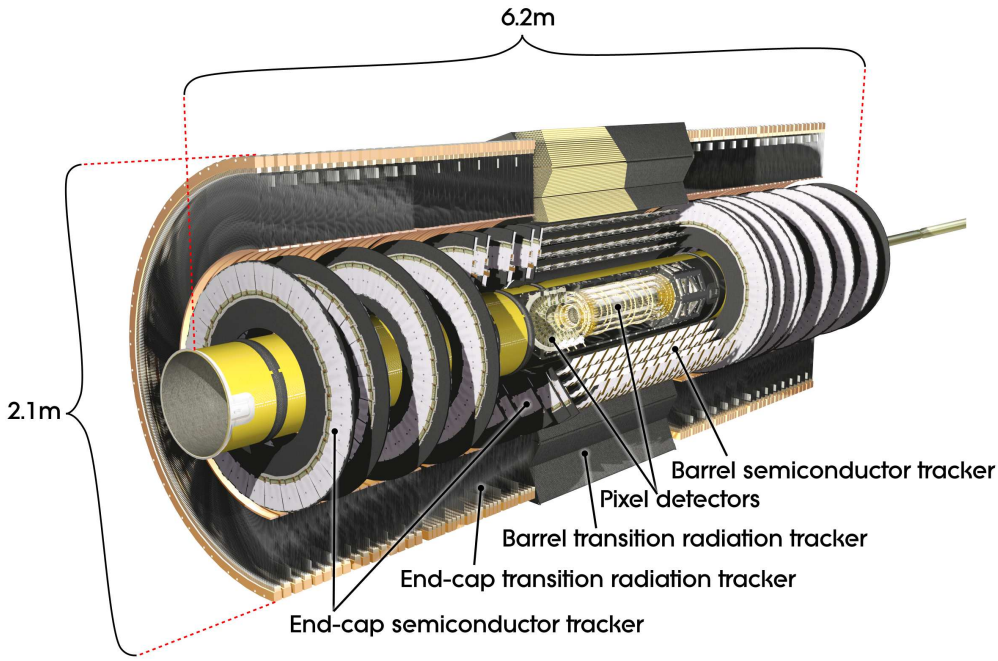

Figure 2.3.: Cut-away schematic of the ATLAS inner detector [20]. The ID consists - from the inside to the outside - of a pixel detector, a semiconductor tracker and a transition radiation tracker.

to an extensive maintenance period of the pixel detector and the replacement of the beam-pipe (29 mm $< R <$ 36 mm) with a new smaller beryllium beam-pipe (25 mm $< R <$ 29 mm). The IBL was then added with an inner radius of 31 mm and an outer radius of 40 mm between the innermost layer of the pixel detector and the beam-pipe. It consists of 14 slightly tilted staves of silicon sensors covering pseudo-rapidities up to $|\eta| < 3$. [22]

Surrounding the pixel detector the silicon **s**emi**c**onductor **t**racker (SCT) is a micro strip tracker composed of 4088 modules in 4 cylindrical barrel layers and 18 planar end-cap discs. This way an almost hermetic angular coverage is achieved granting at least four space-point measurements up to $|\eta| < 2.5$ as shown in Figure 2.4 and Figure 2.5. The pixel detector and the SCT are both silicon based semiconductor detectors. Impurities are added to the Silicon to generate p- and n-doped regions in the material with a depletion zone in between. This generates a diode structure and applying a reverse bias increases the depletion zone. Electron hole pairs generated by penetrating particles can then drift to the respective electrodes where they are measured. [20]

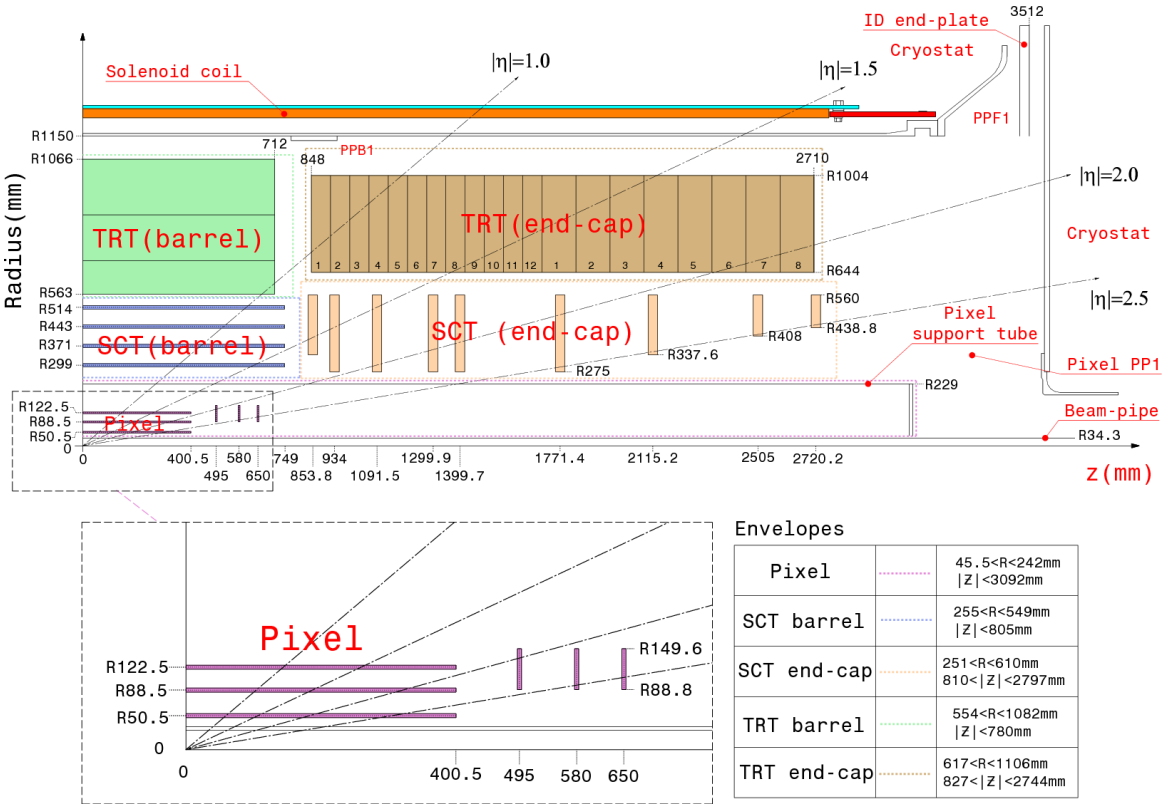

Figure 2.4.: Schematic view of one ATLAS quarter-section up to the solenoid coil [20]. Below an enlarged view of the pixel detector before addition of the **I**nsertable **B**-**L**ayer (IBL) is shown. The y-axis shows the radius in mm while the x-axis shows the z position in mm. Vertical lines also indicate multiple $|\eta|$ regions.

Covering a radial range of 563 mm till 1066 mm the **T**ransition **R**adiation **T**racker (TRT) is the outermost part of the ID as shown in Figure 2.4 and Figure 2.5. In the barrel region it consists of up to 73 layers of straw tubes with a diameter of 4 mm embedded in a radiator of 19 µm polypropylene fibers. In the end-cap region there are 160 straw planes with polypropylene foils covering pseudo-rapidities up to $|\eta| < 2$. The TRT can distinguish electrons from other long lived charged particles by the transition radiation produced by electrons passing the polypropylene radiators which is then measured in the gas filled detector tubes by ionization processes. [20]

In order to measure the charge and transverse momentum of the particles when they pass the different layers of the ID a strong magnetic field is required. Therefore, the ID is surrounded by a solenoid coil of Nb-Ti-cables in a copper matrix with an inner and

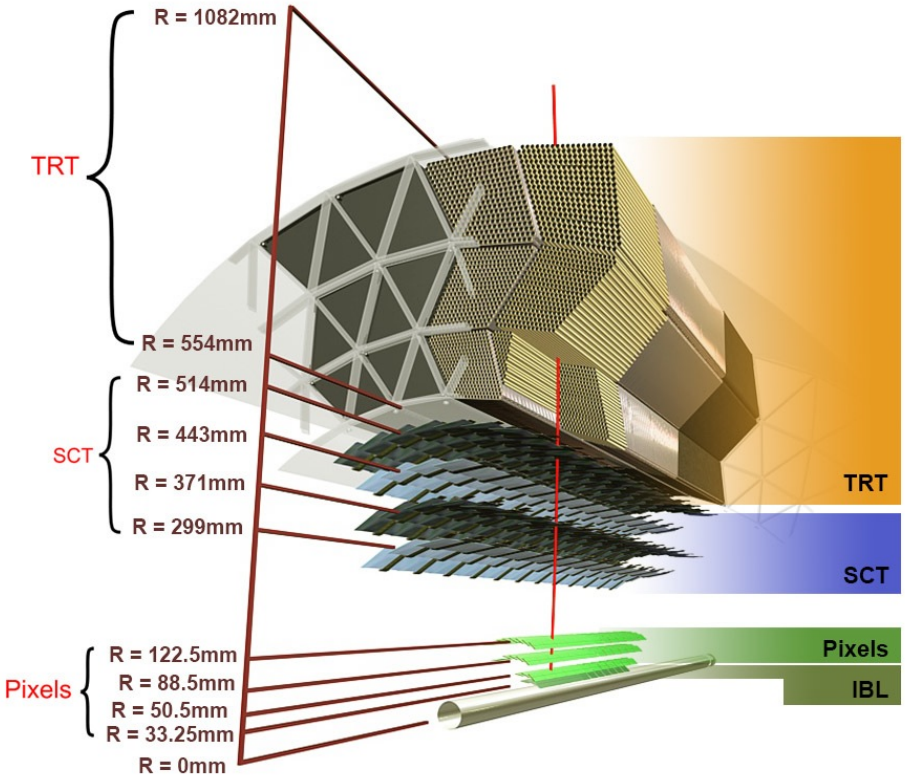

Figure 2.5.: Inner detector cross section [23]. Radius parameters are given for IBL, pixel, SCT and TRT for the barrel region.

outer radius of 1.23 m and 1.28 m, respectively. It uses an operational current of about 7.7 kA storing an energy of 40 MJ to generate a solenoidal magnetic field. This results in an axial magnetic flux in the ID with a field strength of 2 T ensuring an integrated bending power of 2 Tm up to $|\eta| < 1.2$. The bending power then gradually degrades till 0.4 Tm at the edge of the IBL at $|\eta| = 3$. The slim design corresponding to only ≈ 0.66 radiation lengths ensures a minimal energy loss for all traversing particles. [24, 25]

2.2.2. Electromagnetic and Hadronic Calorimeters

The ATLAS calorimeter system almost hermetically encloses the ID system covering pseudo-rapidities up to $|\eta| < 4.9$ in order to contain and measure the full event i.e. the energy of all produced particles. A high energetic particle generates a particle shower in the absorber material which is then detected by the active material. Muons

generated during collisions at LHC typically are minimal ionizing and therefore are the only charged particles permeating the calorimeter. Figure 2.6 shows a cut-out schematic of the calorimeter system.

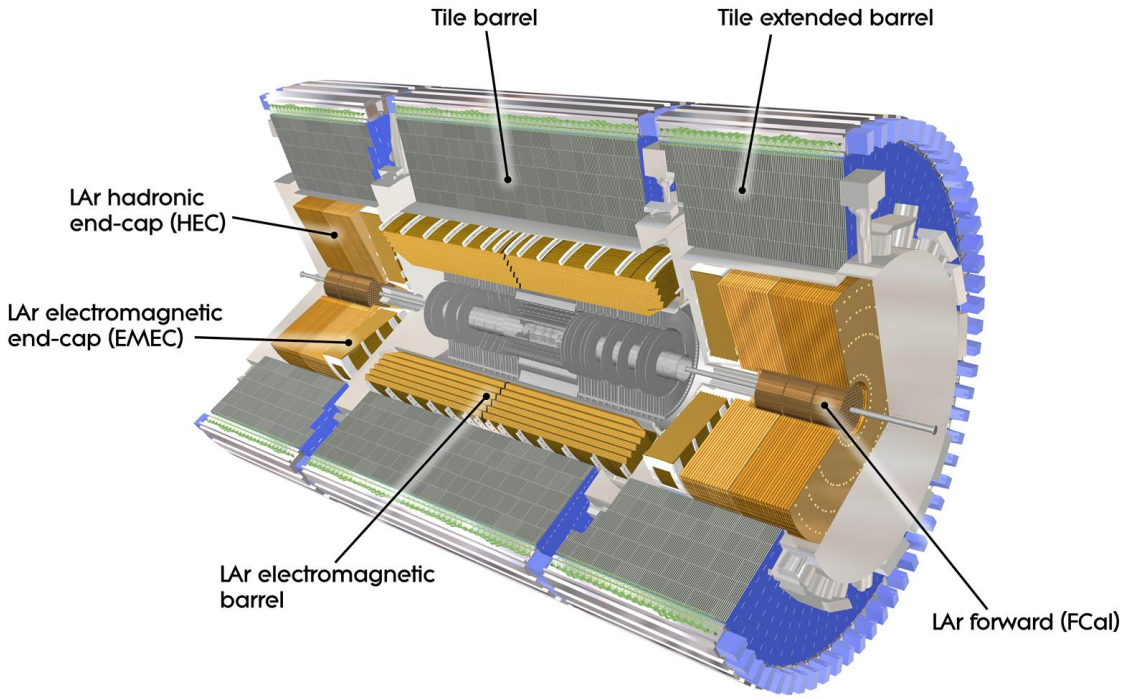

Figure 2.6.: Overview of the ATLAS calorimeter system [20]. The LAr-calorimeter is shown in yellow while the tile-calorimeter is shown in blue.

The electromagnetic calorimeter uses lead as "high-Z" absorbers. Stainless steel is used to separate the lead from the **l**iquid **ar**gon (LAr) which is ionized by traversing charged particles. The readout is done by multiple copper layers separated by insulating foils. These structures are folded in an accordion-like structure as shown in Figure 2.7. It is separated in a barrel region ($|\eta| < 1.475$) and an end-cap region ($1.375 < |\eta| < 3.2$) with a thickness of at least 20 radiation lengths X_0 up to almost 40 X_0 in the end-caps. [20]

The hadronic calorimeter uses a LAr system in the end-cap ($1.5 < |\eta| < 3.2$) and forward ($3.1 < |\eta| < 4.9$) regions as well. The high particle flux and radiative load in the very forward region is too high for standard tracking systems so only the calorimeter is providing a very forward coverage to ensure detection of jets in the vicinity of the beam-pipe.

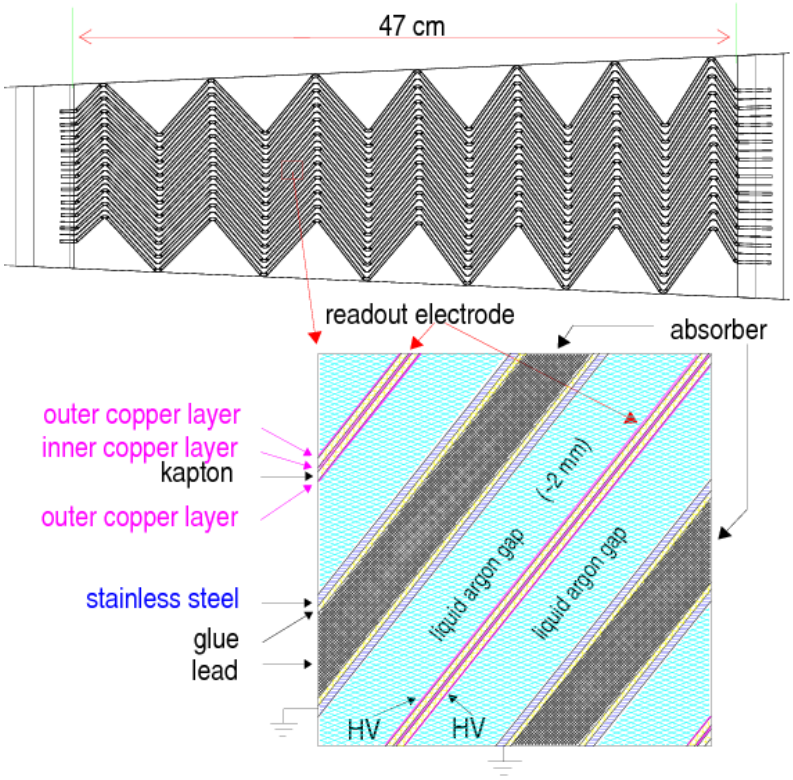

Figure 2.7.: Schematic of the LAr calorimeter structure. The lead absorber, the liquid argon layer and the copper read-out are folded into an accordion-like geometry. [26]

The LAr calorimeter is surrounded by tile calorimeter which consists of a barrel ($|\eta| < 1.0$) and an extended barrel ($0.8 < |\eta| < 1.7$) region. It consists of a steel absorber and scintillating tiles which have a granularity of $\Delta\eta \times \Delta\phi = 0.1 \times 0.1$ in the inner part and 0.2×0.1 in the outer part. The scintillators are read out using photomultiplier tubes. In total the calorimeter extends over 11 interaction lengths λ for $\eta = 0$ and still over 9 interaction lengths up to $\eta = 4.9$ ensuring that most of the energy is measured by one of the components [20].

2.2.3. Muon Detector System

The muon is the only charged particle that, due to its minimal ionizing properties at typical LHC energies, passes through the calorimeter systems. The MS as shown in Figure 2.8 is surrounding the calorimeter as the outermost detector system of ATLAS. It covers pseudorapidity ranges up to $|\eta| < 2.7$ allowing to reconstruct muons down to $\approx 3\,\text{GeV}$ [20].

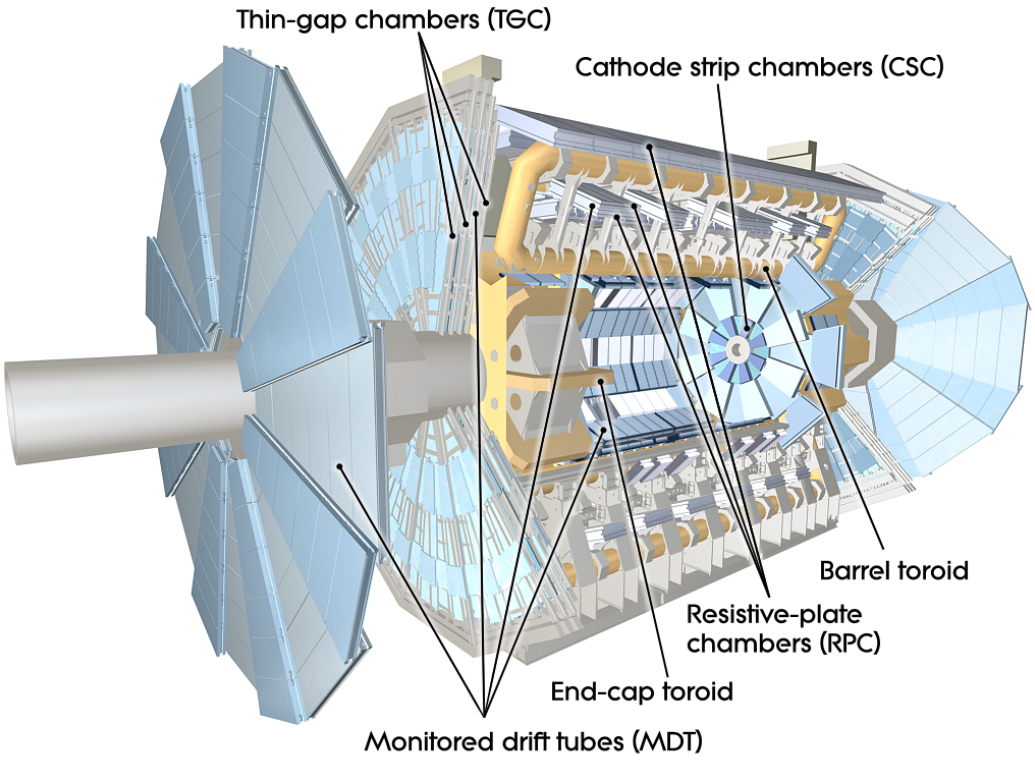

Figure 2.8.: ATLAS muon system cut-away schematic [20]. The toroid magnet system is shown in yellow while the muon chambers are in a light blue color.

In order to determine the muon's charge and measure its momentum up to energies of $\approx 3\,\text{TeV}$ a strong magnetic field is necessary. This is realized by a three piece toroidal magnet system that is giving ATLAS its name. It contains a barrel part and two end-caps with eight magnetic coils each. The Nb-Ti-cables conduct up to 20 kA and store an energy of about 1 GJ in order to generate a 0.5 T magnetic field in the barrel and about 1 T in the end-caps [20].[9] The integrated bending power highly depends on the $\eta\phi-$region a particle is passing through. For the most central region

[9] Cooling down the magnet to its operational state of 4.6 K takes five weeks.

the bending power is 2-4 Tm while in the forward region it goes up to a maximum of 9 Tm [27].

In the barrel region the MS consists of three concentric layers with radii of about 5 m, 7.5 m, and 10 m. In the end-cap regions the detectors are mounted perpendicular to the beam axis at ranges to the interaction point $\pm z$ of 7.4 m, 10.8 m, 14 m, and 21.5 m as can be seen in Figure 2.9. Overall the MS covers an angular region up to $|\eta| < 2.7$ with gabs for the detector support structure and service installations.

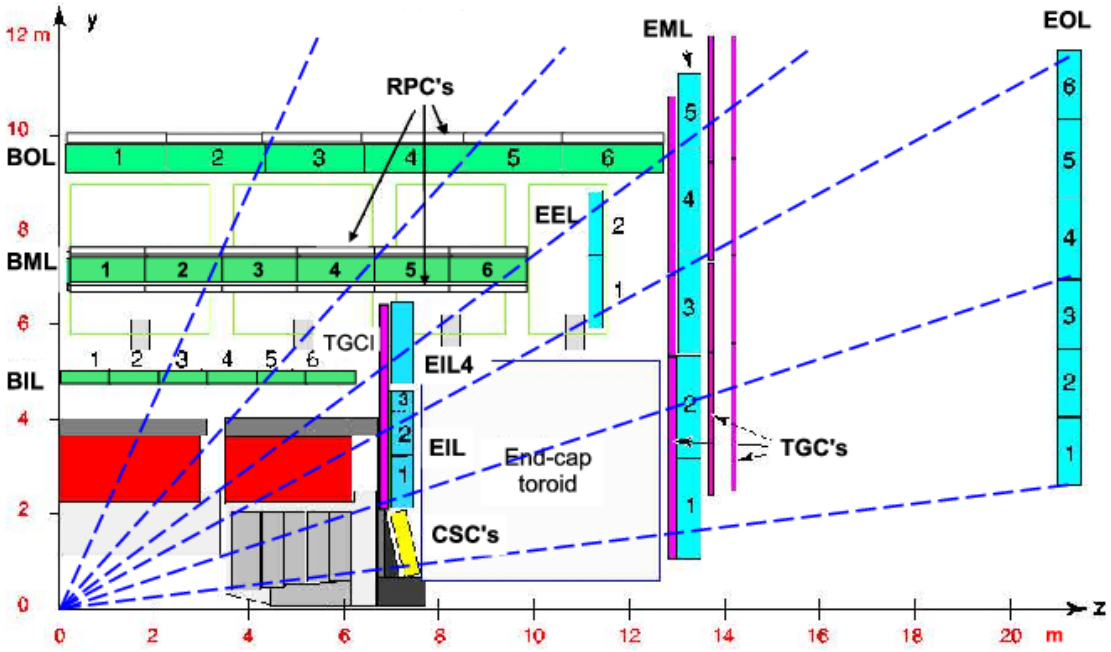

Figure 2.9.: Side-view of the ATLAS muon system quarter-section [20]. The radius is shown on the y-axis while the z-position is shown on the x-axis. MDTs are shown in green and turquoise while CSCs are yellow. For the trigger related systems the TGCs are drawn in purple while the RPCs are drawn without a fill color.

The MS consists of four different detector types which are split in two main categories.

For precision momentum measurements **M**onitored **D**rift **T**ube Chambers (MDTs) are used covering the entire pseudorapidity range of the MS. The drift tubes are about 30 mm in diameter and filled with an Ar/CO_2 gas mixture at 3 bar. In the center is a small W-Re-wire with a high voltage of about 3 kV applied. Traversing charged

particles ionize the gas and an increasing avalanche of electrons occurs which is then collected and read-out at the central wire. Each MDT is three to eight layers thick providing a single hit resolution of 80 µm in the bending plane [28]. During LS1 new detector components were added to the MS. Additional **s**mall-diameter **M**onitored **D**rift **T**ube Chambers (sMDT) where added in regions like the detector feet where the previous MDT did not fit. Due to the smaller radius of 15 mm they are also able to work in environments with higher particle rates [29].

Due to intense radiation in the forward region **C**athode-**S**trip **C**hambers (CSC) are used covering the innermost layer of the end-cap at $2.0 < |\eta| < 2.7$. These multi-wire proportional chambers use wires aligned in radial direction while the cathode strips are oriented orthogonally with respect to the wires. They are capable to deal with a particle flux of 1000 Hz/cm^2 which is six times higher than the MDT.

For these detectors to achieve a sagitta measurement of 500 µm with a precision of 50 µm which is necessary to measure muons up to 1 TeV with only 10% uncertainty the position of the wires has to be known to better than 30 µm. This is done not only by optical alignment but also by track-based data-driven alignment.

The second class of muon detectors are dedicated to triggering and therefore need a time resolution in the order of a few tens of nanoseconds. This is achieved by **R**esistive **P**late **C**hambers (RPCs) in the central region of $|\eta| < 1.05$. They are placed in front and behind the MDTs. RPCs are in principle plate capacitors with a 2 mm gap, at a operation voltage of 9.8 kV, filled with a gas mixture which gets ionized by traversing particles.

Thin **G**ap **C**hambers (TGC) are used in the more forward region $1.05 < |\eta| < 2.4$. These are multi-wire proportional chambers where the wire-to-cathode distance of 1.4 mm is smaller than the wire-to-wire distance of 1.8 mm. This results in short drift times and therefore a fast signal readout.

2.2.4. Forward Detectors and Luminosity Measurements

ATLAS has three sub-detectors for forward and luminosity measurements. These are placed in the most forward regions next to the beam-pipe. The **Lu**minosity measurement using **C**erenkov **I**ntegrating **D**etector (LUCID) is the first detector located at ±17 m along the beam-line corresponding to $|\eta| \approx 5.8$. As the name suggests it is a gas-based cerenkov detector used for online luminosity monitoring by measuring inelastic proton proton scattering.

The **Z**ero-**D**egree **C**alorimeter (ZDC) is placed $\pm 140\,\mathrm{m}$ away from the interaction point covering an pseudorapity region of $|\eta| > 8.3$ and is designed to detect forward neutrons from heavy-ion collisions. It can also be used as a minimum-bias trigger by triggering on the proton remnants from the hard scattering process. It consists of tungsten absorbers read out by quartz strips connected to photomultipliers.

The most forward detector is the **A**bsolute **L**uminosity **F**or **A**TLAS (ALFA) detector. It determines the luminosity by measuring forward elastic scattering and by exploiting the optical-theorem[10]. The detector consists of stacks of scintillating fibers housed in roman pots which can move the detector as close as 1 mm to the beam. [20]

In addition to these forward detectors **B**eam **C**onditions **M**onitor (BCM) detectors are included in the ID. These BCM systems are designed to protect ATLAS against dangerously high radiative loads e.g. in case of proton bunches hitting a collimator in front of the detector. These detectors not only prevent damage to other components but due to their sensitivity to the particle flux they contribute to the determination of the luminosity $\mathcal{L}$. Combining results from these detectors with dedicated **v**an **d**er **M**eer (vdM) measurements results in an uncertainty $\delta\mathcal{L}/\mathcal{L} = \pm 1.8\%$ [30].

2.2.5. The ATLAS Trigger and Data Acquisition System

The high rate of particle interactions and the high number of read-out channels in the ATLAS detector makes it necessary to reduce the incoming data significantly for the **D**ata **Aq**uisition (DAQ) to handle it. Therefore, a dedicated trigger system is put in place considerably reducing the data stream. The combined system is also referred to as **T**rigger and **D**ata **Aq**uisition (TDAQ).

The *Run 2* TDAQ scheme is shown in Figure 2.10. It is based on a **L**evel-**1** (L1) hardware trigger and a single **H**igh **L**evel **T**rigger (HLT). The L1 is fed by the calorimeter and muon detector (e.g. the RPC and TGC). It is triggering on simple signatures like high p_{T} objects (e.g. muons). Based on these trigger decision **R**egion **o**f **I**nterest (RoI) and so-called super-RoI[11] are formed. These are then used in the HLT which has access to the full event information and uses algorithms very close to the offline versions to calculate a trigger decision. As can be seen from the right part of Figure 2.10

[10] The optical theorem relates the total cross section to the imaginary part of the scattering amplitude for a vanishing momentum transfer, i.e. scattering in the forward direction.

[11] Building super-RoI means merging multiple overlapping RoI to just one, in order to significantly reduce computing efforts.

the TDAQ system reduces the event rate from initial 40 MHz to about 1 kHz. This corresponds to a reduction of almost five orders of magnitude, from about 100 TB/s to 2.4 GB/s [31, 32] .

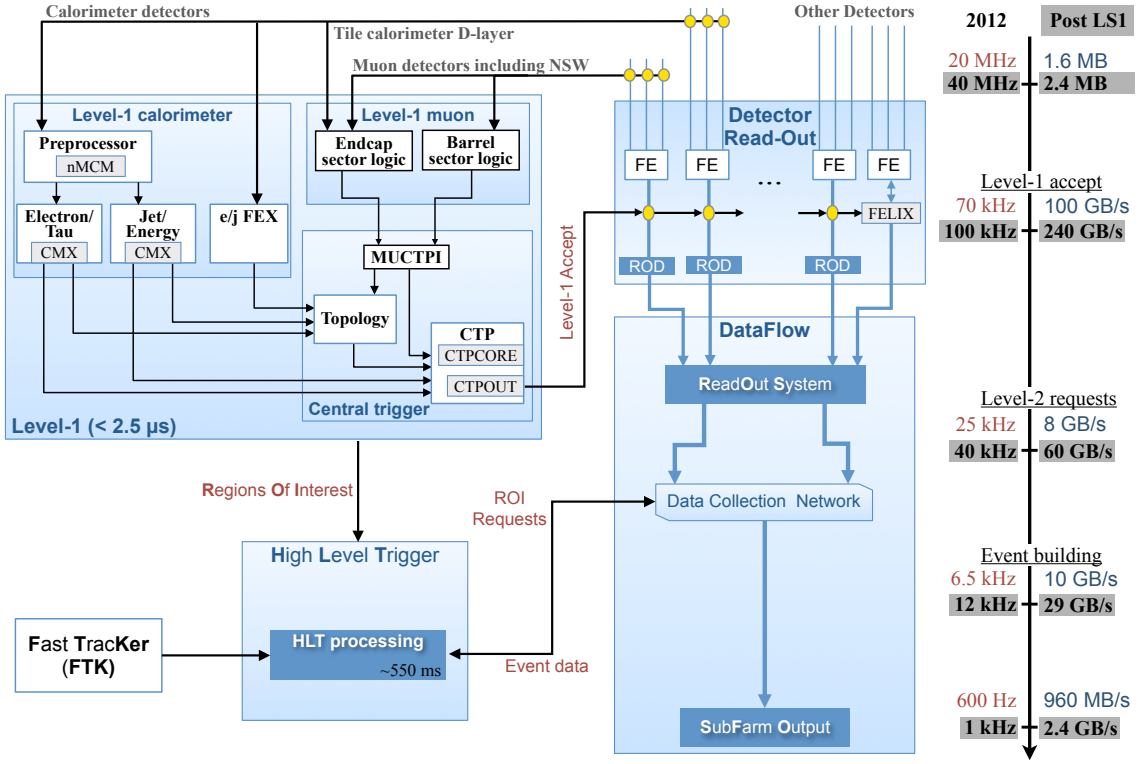

Figure 2.10.: ATLAS TDAQ system in *Run 2* [33]. The Level 1 trigger is shown in the top left edge processing information from calorimeter and muon detectors. The HLT is then using additional information for the final trigger decision. On the right a scale compares the reduction in trigger rate and data bandwidth for Run 1 and Run 2 TDAQ.

In *Run 1* the ATLAS trigger was based on a three stage system. The L1 trigger was still the first instance but the HLT was separated into two steps. First based on the L1 trigger decisions there was a **L**evel-**2** (L2) trigger running on RoI only. The super-RoI concept wasn't introduced before *Run 2*. It further reduced the amount of data that needs to be read out. The **E**vent **F**ilter (EF) then uses the full detector information to further reduce the amount of data rate. In *Run 1* the TDAQ was limited to 1 GB/s [34].

The total TDAQ bandwidth has to be allocated to multiple trigger streams, i.e. different trigger signatures. While rare processes are limited to their abundance in the collisions, prevalent processes with common signatures are occurring more frequently than can be recorded. Triggers searching for such signatures are pre-scaled and therefore set to limited bandwidth. A pre-scale of 100 means that only every hundredth event passing the trigger will be recorded by the DAQ system. In this analysis muon-in-jet triggers are used as described in Section 6.1.

In addition to simple signature triggers there have been multiple implementations of flavor tagging algorithms in *Run 1* and *Run 2*. Those are discussed in more detail in Section 5.2.

3. Definition and Reconstruction of Physics Objects in ATLAS

Wie schwer sind nicht die Mittel zu erwerben,
Durch die man zu den Quellen steigt!

WAGNER

In proton-proton collisions the physics processes are described by the **S**tandard **M**odel (SM) as discussed in Chapter 1. The particles produced in such interactions are then measured in the ATLAS detector as described in Chapter 2. The detector measures hits and energy depositions which are reconstructed as tracks and identified as particles. This task is done by multiple dedicated algorithms, that might slightly differ for online and offline objects, i.e. objects reconstructed during and after data-taking respectively. In this chapter the emphasize lies on offline reconstruction as used by the $p_{\mathrm{T}}^{\mathrm{rel}}$-analysis.

For the purpose of flavor tagging, i.e. determining the flavor of a jet, an optimal track and vertex resolution is crucial. In addition, the muon is of particular interest for this thesis. Furthermore, there are physics objects like electrons, photons or **m**issing $\boldsymbol{E_{\mathrm{T}}}$ (MET) which will not be discussed here. MET is the vectorial sum of all physics objects leaving only the unbalanced transversal component.

3.1. Tracking

The main tracking algorithm used within ATLAS is the **New T**racking (NEWT) algorithm which is rather a toolbox of algorithms and methodologies [35]. NEWT can run in an inside-out as well as an outside-in sequence with multiple algorithms and configurations.

A short overview on inside-out track algorithm is given in the following. First, the expected interaction region is retrieved from a conditions data-base. Then space points are calculated by a simple local-to-global transformation getting the global detector positions from the local **I**nner **D**etector (ID) hits. These space points are

used for seeding the search for track candidates starting from pixel only and, in a second step, also from the **s**emi**c**onductor **t**racker (SCT). Additional constraints on the vertex z-position are also included. Then multiple Kalman-filter techniques can be used to filter hits that belong to tracks [36]. Therefore, the contribution of each hit to the fits χ^2 is evaluated. In order to assess the goodness of a fitted track and resolve ambiguities, a likelihood is computed which also takes topological signatures into consideration. For example, a missing hit in the innermost pixel layer results in a strong penalty in the likelihood value. Tracks found this way are extended into the **T**ransition **R**adiation **T**racker (TRT) by fitting an extension onto the existing track. Finally a list of particle-track candidates is retrieved [35, 37].

3.2. Vertex Finding

For vertex fitting, different procedures were used in *Run 1* and *Run 2*. In *Run 1* the following iterative vertex reconstruction algorithm was used [38]. First step is to find tracks that can be associated to a vertex. For this vertex finding minimal requirements have to be fulfilled by the tracks:

- Transverse track momentum $p_{\mathrm{T}} > 150\,\mathrm{MeV}$,
- Transverse track impact parameter $|d_0| < 4\,\mathrm{mm}$,
- Uncertainty of the transverse track impact parameter $\sigma(d_0) < 5\,\mathrm{mm}$,
- Uncertainty of the longitudinal track impact parameter $\sigma(z_0) < 10\,\mathrm{mm}$,
- Number of SCT hits $N_{\mathrm{Hits}}^{\mathrm{SCT}} \geq 4$,
- Number of hits in SCT and pixel $N_{\mathrm{Hits}}^{\mathrm{Pixel+SCT}} \geq 6$.

For the remaining track candidates, z distributions are searched for maxima, i.e. points where multiple tracks cross each other, which is used as a vertex seed. After that the vertex is fitted using the same adaptive vertex fitting algorithm as described in [39]. A χ^2-criterion is used to associate tracks recursively to calculate the vertex position and error matrix for multiple vertices. Figure 3.1 shows the spatial distribution of reconstructed primary vertices. It can be seen that the spread of the interaction region in z-direction is much wider than in the xy-plane.

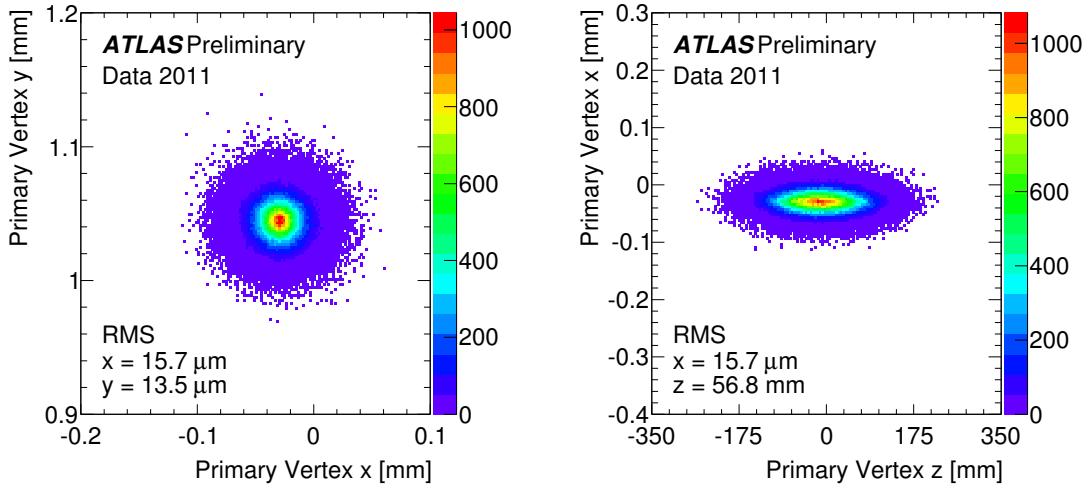

(a) PV position in xy-plain.

(b) PV position in xz-plain.

Figure 3.1.: Reconstructed primary vertex position in 2011 data with $\sqrt{s} = 7\,\text{TeV}$ [40]. Here a 400 MeV track cut is used. These plots are updates to [38].

For *Run 2* additional algorithms were developed making use of image reconstruction techniques. Therefore, the reconstructed tracks form a three dimensional source density in the interaction region. After transformation into Fourier-space using a three dimensional discrete Fourier transformation, image filtering algorithms can be used to reduce blurring and artifacts. After back transformation the source density is explored for maxima. Around these maxima, vertices are clustered with the vertex position being the center of gravity of the resulting cluster [41, 42].

During the operation of the **L**arge **H**adron **C**ollider (LHC) the run conditions change, which includes the center of mass energy and also to the instantaneous luminosity. The instantaneous luminosity can be increased by raising the amount of protons in each bunch. This increases also the amount of additional zero-bias interactions also denoted as pile-up. The mean number of interactions per bunch crossing μ is a measure for pile-up since not more than one hard scattering process is expected per bunch crossing. The **p**rimary **v**ertex (PV) is defined as the vertex with the highest p_{T}^2-sum of associated tracks. For b-tagging purposes, the reconstruction of secondary vertices is of particular interest. The secondary vertex reconstruction algorithm used for b-tagging is discussed in Chapter 5.1.

3.3. Jets

Starting from calorimeter cells effective noise functions are used to remove electronic and pile-up noise. The electronic signal of the cleaned cells is calibrated at the electromagnetic (EM) scale to compute the cell energy E_{cell} [43]. This scale reproduces the energy response generated by photons or electrons appropriately but does not account for additional hadronic losses. A three-dimensional topological clustering algorithm follows patterns in the cell signal significance

$$\zeta_{\text{cell}} = \frac{E_{\text{cell}}}{\sigma_{\text{cell}}^{\text{noise}}}, \tag{3.1}$$

with the average cell noise $\sigma_{\text{cell}}^{\text{noise}}$, to combine cells in a sequence of seed and collect steps [44–46]. The resulting topological cluster, or topo cluster, is assumed to be a massless pseudo-particle with the energy E_{tc} being a weighted sum of the cell energies. Combining also the cell directions, the four momentum vector P_{tc} of the cluster can be found as

$$P_{\text{tc}} = E_{\text{tc}} \cdot \begin{pmatrix} 1 \\ \sin\theta_{\text{tc}} \cos\phi_{\text{tc}} \\ \sin\theta_{\text{tc}} \sin\phi_{\text{tc}} \\ \cos\theta_{\text{tc}} \end{pmatrix}. \tag{3.2}$$

Exploiting differences in shape variables, the resulting clusters can be characterized as being electromagnetic, meaning that it most likely originates from γ or e, or hadronic. An additional calibration step can be performed using **l**ocal hadronic **c**ell **w**eighting (LCW). These **l**ocally **c**alibrated (LC) clusters are corrected for signal losses due to inactive material or due to noise suppression during the clustering procedure. Hadronic jets are also corrected for the non-compensating calorimeter response, which means that hadronic showers are measured with lower energy when compared to electromagnetic showers. [47]. After this step the sum of cluster energies is expected to represent the energy deposition of the particle shower.

A variety of algorithms exists for jet clustering that can be used for calorimeter cells or tracks. In this thesis the "algorithm of choice" is the infrared and collinear safe anti-k_t algorithm [48]. Based on topological clusters, jets are build with a radius parameter of $R = 0.4$ in the $\eta\phi$-plane. The algorithm uses the distance measure d_{ij} between two entities i and j defined as

$$d_{ij} = \min(p_{\text{T}i}^{-2}, p_{\text{T}j}^{-2}) \frac{\Delta R_{ij}^2}{R^2}, \tag{3.3}$$

with the distance in the rapidity-azimuthal-plane $\Delta R_{ij}^2 = (y_i - y_j)^2 + (\phi_i - \phi_j)^2$ and $p_{\mathrm{T}i}$, y_i and ϕ_i being the respective transverse momentum, rapidity[12] and azimuth of entity i. The algorithm combines clusters j to the proto-jet i until $d_{ij} > p_{\mathrm{T}i}^2$.

This procedure is done using EM or LC clusters as well as clusters based on trigger level properties. The $p_{\mathrm{T}}^{\mathrm{rel}}$-calibration was performed for all of those possibilities.

3.3.1. Pile-up Mitigation

Pile-up is dominated by soft QCD events. These cause additional activity in the calorimeter system which can be reconstructed as low energy jets not emerging from the primary vertex. Pile-up mitigation techniques utilized in this analysis are discussed in [49, 50]. During *Run 1* the **J**et **V**ertex **F**raction (JVF) was introduced. It is defined as the sum of the transverse momenta of all tracks of the jet that are coming from the primary vertex divided by the sum of transverse momenta of all tracks of the jet. A cut is then applied for all jets with $|\eta| < 2.4$ and $p_{\mathrm{T}} < 50\,\mathrm{GeV}$. For *Run 2* in addition to JVF[13] the $R_{p_{\mathrm{T}}}$ variable is used, which relates the sum of the track momenta from the primary vertex to the full jet p_{T}, which has been determined from calorimeter clusters. The **J**et **V**ertex **T**agger (JVT) utilizes a two dimensional likelihood of those variables to discriminate pile-up jets in a slightly bigger kinematic region $|\eta| < 2.4$ and $p_{\mathrm{T}} < 60\,\mathrm{GeV}$ [49, 50].

3.4. Muons

Muon candidates penetrate the full detector and are therefore measured in the ID and **M**uon **S**pectrometer (MS) independently. The ID provides a precise measurement of the muon track close to the interaction point, which is crucial to associate the muon to a vertex. The measurement in the MS provides an additional precise measurement of the track momentum with a large integrated bending power. Energy losses in the calorimeter system can be used as additional information to the global muon reconstruction. Several types of muons are defined depending on the information used for the reconstruction [51, 52]:

[12] The anti-k_t algorithm is used on topo clusters which are assumed to be massless pseudo-particles and hence the rapidity and pseudorapidity are identical.

[13] In *Run 2* an additional correction is applied to the JVF accounting for the pile-up-dependence of the variable.

- Muons that are reconstructed using the MS only are called **s**tand-**a**lone (SA) muons. The muon track is then extrapolated back to the interaction region and a vertex is reconstructed from the stand-alone track [53].

- Candidates with tracks reconstructed in the ID are referred to as **s**egment-**t**agged (ST) muons. The fitted track has to be associated to at least one local track segment in the **M**onitored **D**rift **T**ube Chamber (MDT) or **C**athode-**S**trip **C**hambers (CSC). This increases the overall acceptance by adding muons that do not have enough hits in the MS.

- In order to reconstruct muons outside the acceptance of the MS, calorimeter information can be used. Therefore, a ID track is extrapolated into the calorimeter system and associated to an energy deposit compatible with the expectation for a minimal ionizing particle.

- The commonly used type of muons is the **c**om**b**ined (CB) muon. Therefore, a track has to be successfully fitted in the ID and MS independently. The two tracks are then combined either using a statistical combination based on the corresponding covariance matrices or by a global re-fit using hit information from both detector systems.

The CB muons have the highest purity and are therefore used for the $p_{\mathrm{T}}^{\mathrm{rel}}$-method. The reconstruction efficiency can be measured using Z and J/Ψ decays in a tag-and-probe approach. The overall muon reconstruction efficiency is close to 99 %, but degrades in the soft $p_{\mathrm{T}} < 5\,\mathrm{GeV}$ region [28].

4. Monte-Carlo-Simulations

Welch Schauspiel! aber ach! ein Schauspiel nur!
Wo faß' ich dich, unendliche Natur?

FAUST

In particle physics statistical methods are generally used. Due to the high complexity of its experiments, it is very complicated to evaluate a probability density function for the full phase-space. Thereby, huge efforts are made to generate those probability densities with **M**onte **C**arlo (MC) methods. The full problem of simulating statistical distributions for all available variables is solved by an event based simulation where the different steps factorize very well. This means that the full simulation can be done in multiple independent steps. First, the hard scatter process is modeled in different orders of perturbative **q**uantum **f**ield **t**heory (QFT). Second, the hadronization is added with dedicated shower generators and finally, a detector simulation is done, modeling all the interactions with the detector material. On top of the hard scatter process, the underlying event, i.e. the interaction between the proton remnants as well as additional pile-up interactions, are simulated.

4.1. Pythia di-jet MC

This thesis deals with **q**uantum **c**hromo**d**ynamics (QCD) dominated phase-space and, therefore uses di-jet MC samples. These are simulated using the PYTHIA 8 package [54], which is capable of generating the hard scattering interaction, including also initial- and final-state interactions, and also the hadronization process using string fragmentation. The simulation therefore depends on a variety of free parameters.

Before the actual simulation, the **P**arton **D**istribution **F**unction (PDF) used with PYTHIA has to be specified. This defines the high dimensional probability density for the initial state which has to be adjusted to particle physics measurements. From this initial state the hard scatter process is calculated using sets of parameters motivated by particle physics measurements.

These so called tunes define parameters like the strength of the strong interaction $\alpha_s(Q)$ at the different interaction scales Q like the hard scatter process and **I**nitial **S**tate **R**adiation (ISR) and **f**inal **s**tate **r**adiation (FSR). After the hadronization the resulting hadrons are interfaced into the EvtGen package [55]. With the special emphasis on b-physics in this thesis, it is important to have an accurate description of flavor physics in the simulation. The EvtGen package includes full B-decay tables with the latest and most precise measurements as well as semileptonic form-factor models. After refining hadron properties the particle flight through the ATLAS detector is simulated using the GEANT4 package with a full implementation of the detector geometry and magnetic field maps [56]. In this step, the detector response to the traversing particle is generated. These MC events are reconstructed in the same way as the collision data described in Chapter 3.

In *Run 1* the CT10 PDF is used [57]. This is then used in the AU2CT10 PYTHIA tune [58] and interfaced wit the EvtGen package to improve the modeling of b-hadron decays. For GEANT4 simulation and reconstruction the ATLAS-GEO-20-00-01 geometry version is used.

In *Run 2* PDFs are used, that are next-to-next-to-leading-order in QCD and tuned to LHC measurements defining the NNPDF23 [59]. From this the NNPDF23LO set with leading-order QED corrections is constructed [60]. It is then combined with the ATLAS 2014 tune to the overall A14NNPDF23LO configuration [61] in which PYTHIA generates the events. Again the EvtGen simulation package is used. For the detector simulation GEANT4 is used with the updated ATLAS-R2-2015-03-01-00 geometry which includes upgrades like the **I**nsertable **B**-**L**ayer (IBL).

The cross-section of multi-jet events induced by the strong interaction as studied in this thesis falls very steeply with the jet momentum. In order to simulate events over a large range of jet momenta generating a rather flat statistical precision over the whole spectrum, special techniques are used. First, the overall $p_{\mathrm{T}}^{\mathrm{jet}}$ spectrum is divided into slices which are then generated separately[14]. These samples are called JX samples where X denotes the number of the slice increasing with $p_{\mathrm{T}}^{\mathrm{jet}}$. Second, within each slice the leading $p_{\mathrm{T}}^{\mathrm{jet}}$-spectrum is generated rather flat when compared to the physical spectrum. This is done to generate a similar statistical precision over the full momentum range. The individual events have to be weighted with an event weight computed by the generator to produce a physical distribution. These

[14]For the determination of slice boundaries, anti-k_t 6 jets, built on truth level information are used.

techniques were applied for *Run 1* and *Run 2* and are internally documented in [62] and [63], respectively. For *Run 2* improved slice boundaries were used, which can be seen in Table 4.1 and Table 4.2, showing an overview on the samples used in *Run 1* and *Run 2*.

Table 4.1.: JX sample definition as used in *Run 1* [62].

Name	dataset ID	$p_{\mathrm{T}}^{\mathrm{jet,\ truth}}$ [GeV]	Cross-section σ [nb]	N^{events}
J0	129270	0 - 20	$7.285 \cdot 10^7$	2M
J1	129271	20 - 60	$7.285 \cdot 10^7$	1M
J2	129272	60 - 200	$2.636 \cdot 10^4$	3M
J3	129273	200 - 500	$5.442 \cdot 10^2$	2M

Table 4.2.: JX sample definition as used in *Run 2* [63].

Name	dataset ID	$p_{\mathrm{T}}^{\mathrm{jet,\ truth}}$ [GeV]	Cross-section σ [nb]	N^{events}
J0	361020	0 - 20	$7.842 \cdot 10^7$	2M
J1	361021	20 - 60	$7.842 \cdot 10^7$	2M
J2	361022	60 - 160	$2.433 \cdot 10^6$	2M
J3	361023	160 - 400	$2.645 \cdot 10^4$	2M

4.2. Muon Filtered Samples

In addition to the jet slicing a second filtering option is used. Since the $p_{\mathrm{T}}^{\mathrm{rel}}$-method relies on muon kinematics, it is mandatory to have at least one muon in each event. Generating minimum bias samples based on strong interaction processes not necessarily generate muons. In order to increase this fraction, a truth level filter, rejecting events without a muon, is used. An overview on the used muon-filtered samples is shown in Table 4.3.

Table 4.3.: JX muon filtered sample definition as used in *Run 1*.

Name	Datset ID	$p_{\mathrm{T}}^{\mathrm{jet,\ truth}}$ [GeV]	Cross-section σ [nb]	N^{events}
J0	129280	0 - 20	$7.285 \cdot 10^7$	4M
J1	129281	20 - 60	$4.144 \cdot 10^6$	8M
J2	129282	60 - 200	$5.015 \cdot 10^3$	10M
J3	129283	200 - 500	$5.442 \cdot 10^2$	4M

In *Run 2* this simple filtering technique is only applied in the soft QCD region where the energy scale of the scattering process is close to additional radiative corrections. Therefore, the J1 sample is split into two samples J1A and J1B. For J0 and J1A the same filtering techniques as in *Run 1* is used. Starting with J1B, internal features of Pythia are used to generate a biased sample enriched with muon final states. A special treatment has to be applied to these samples, since they are generated from a biased phase-space. They cannot be normalized to the number of generated events, but rather have to be normalized to the sum of the respective event weights computed by Pythia. The muon-filtered samples used in *Run 2* are listed in Table 4.4.

Table 4.4.: JX muon filtered sample definitions as used in *Run 2*.

Name	Datset ID	$p_{\mathrm{T}}^{\mathrm{jet,\ truth}}$ [GeV]	Cross-section σ [nb]	N^{events}
J0	427000	0 - 20	$7.842 \cdot 10^7$	2M
J1A	427030	20 - 40	$7.842 \cdot 10^7$	1M
J1B	427031	40 - 60	$3.153 \cdot 10^7$	1M
J2	427032	60 - 160	$2.433 \cdot 10^6$	2M
J3	427033	160 - 400	$2.645 \cdot 10^4$	2M

An example for the sliced jet spectrum is shown in Figure 4.1. When scaled correctly the jet slices sum up to the steeply dropping distribution observed in a QCD dominated event selection. Basic cuts are applied to reduce pile-up dependence, which would otherwise increase the slope in the low p_{T} region.

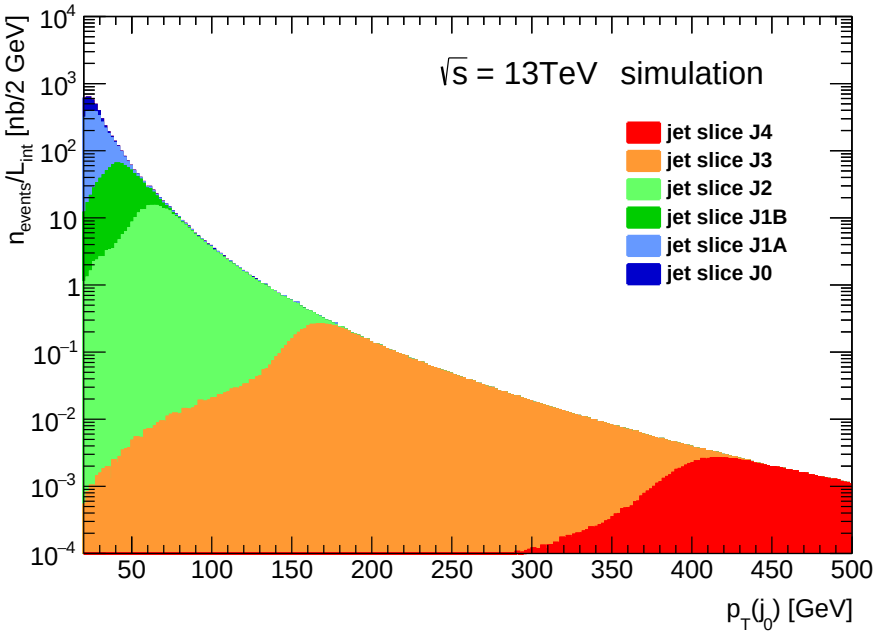

Figure 4.1.: Leading jet p_{T}-distribution for the muon-filtered PYTHIA samples listed in Table 4.4. Cuts on jet and muon multiplicity are applied, as well as pile-up rejecting cuts on the JVT. The datasets are scaled to an integrated luminosity of 1 nb^{-1}.

4.3. Flavor Matching on Truth Level

MC simulations have the advantage of information being available on particle truth level. This includes the flavor of a particle. Therefore, the flavor of a particle and the flavor of a jet can be determined using a standard cone based algorithm, that successively tries to find heavy particles inside the jet cone. First, a b-quark is searched for in a distance $\Delta R = \sqrt{\Delta\eta^2 + \Delta\phi^2} < 0.3$. If it is successful, the jet is labeled as b-jet. If not, the same procedure is done for c- and τ-hypotheses. If all heavy flavor candidates are rejected, the jet is labeled as a light-jet.

5. Flavor Tagging at ATLAS

Ja was man so erkennen heißt!
Wer darf das Kind beym rechten Namen nennen?

FAUST

Tagging algorithms in general are techniques classifying between multiple decisions by exploiting distinguishable properties in the input variables. Flavor tagging is an application where algorithms are used to determine the most probable flavor of a jet, based on reconstructed jet properties. It is very important for the ATLAS physics program, since many analyses rely on tagging algorithms to very efficiently identify objects while rejecting underground processes, as much as possible. In this thesis the emphasis lies on the tagging of b-jets. A detailed overview of the ATLAS flavor tagging efforts is given in [64].

In principal, the performance of tagging algorithms can be assessed by the signal efficiency and the background rejection. For b-tagging a crucial measure to evaluate the performance of an algorithm is the tagging efficiency

$$\varepsilon_b = \frac{N_b^{\text{tagged}}}{N_b^{\text{total}}}, \tag{5.1}$$

with the number of jets tagged by the algorithm N_b^{tagged} divided by the total number of b-jets N_b^{total}. In general, tagging algorithms have a continuous output where cuts can be applied. Each of these cuts corresponds to a b-tagging efficiency and a specific cut is defined as an **o**perating **p**oint (OP). Each OP also corresponds to a specific c-tagging efficiency ε_c and light-rejection rate $R_\ell = \varepsilon_\ell^{-1}$. These are equally important figures, specifying the algorithms ability to reject other jet flavors. In general, the signal and background efficiencies are highly correlated so a trade-off between a high signal efficiency and a high background rejection has to be made when defining OPs for a tagging algorithm. The efficiency (and rejection rates) used for the definition of an OP is evaluated on a specific $t\bar{t}$-simulation to ensure comparability.

5.1. b-Tagging Algorithms

As discussed in Chapter 1 one common property of b-hadrons is their life time in the order of 1-2 ps. Therefore, the particles travel several millimeters in the laboratory frame before decaying, leading to distinguishable decay signatures. These signatures are exploited by dedicated algorithms, most of which are also summarized in [64].

5.1.1. Impact Parameter Based Algorithms

Tracks of the b-hadron's decay products are displaced compared to the **p**rimary **v**ertex (PV) as shown in Figure 5.1. The tracks can be extrapolated backwards and the **i**mpact **p**arameter (IP) can be determined as the point of closest approach with respect to the PV. In ATLAS two projections of the IP are used due to the different resolution in the transversal plane compared to the longitudinal direction. The z_0 is the projection longitudinal to the beam axis and the d_0 is defined in the transversal plane. The IP is signed to further increase its discrimination power. The sign is defined as positive if the track crosses the jet axis in front of the PV, and negative if the track intersects the jet axis behind the PV. For light jets this is a symmetrical distribution due to resolution effects while heavy flavor hadrons generate a higher, positive value of the signed impact parameter significance.

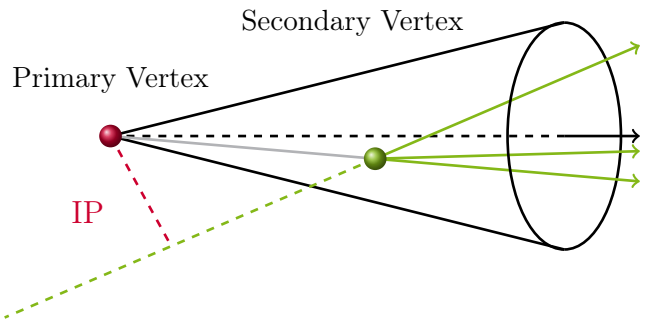

Figure 5.1.: Displaced decay of a b-hadron at a secondary vertex inside a jet. Tracks from the decay products are shown in green. Extending the track beyond the secondary vertex, the IP is the distance at the closest approach to the PV shown in red.

The **JetProb** algorithm uses the track impact parameter significance $S_{d_0} = d_0/\sigma_{d_0}$, with the uncertainty σ_{d_0} of the reconstructed d_0, and compares it to a pre-defined

resolution function $R(S_{d_0})$ [65]. This results in a probability P_i^{trk} of the track to originate from the PV. The probability for all tracks is then combined in one tagging discriminant for the jet P_{jet}. This algorithm has only been used for early data before 2011 and also for online b-tagging during *Run 1*.

The **IPxD** algorithm-family uses pre-determined log-likelihood ratios to compute the tagging discriminant. The **IP1D** uses the longitudinal impact parameter significance, while the **IP2D** tagger utilizes the transverse impact parameter significance. Both are combined in the **IP3D** that uses a two-dimensional likelihood distribution based on both the longitudinal and transversal impact parameter significances. Therefore, the correlation between both variables is taken into account by the two dimensional probability density functions. This way a weight gets assigned to each track based on the (S_{d_0}, S_{z_0})-values of the track. The jet discriminant w_{IP3D} is defined as the sum over all the track weights.

5.1.2. Secondary Vertex Based Algorithms

Since the b-hadron travels multiple millimeters before decaying the different decay products can be traced back to a displaced **s**econdary **v**ertex (SV). The properties of this vertex can then be used to discriminate jet flavors. A dedicated vertex finding algorithm is used to cluster tracks with a high IP significance $S_{d_{3D}} = d_{3D}/\sigma_{d_{3D}}$ that can be associated to a jet. Pairs of these track candidates are fitted to a SV using a χ^2-criterion. Vertex candidates compatible with material interactions, converted photons or long-lived particles like K_{s} or Λ are rejected using geometrical information and invariant mass distributions. Finally all tracks from the remaining vertex candidates are used to refit a single inclusive SV.

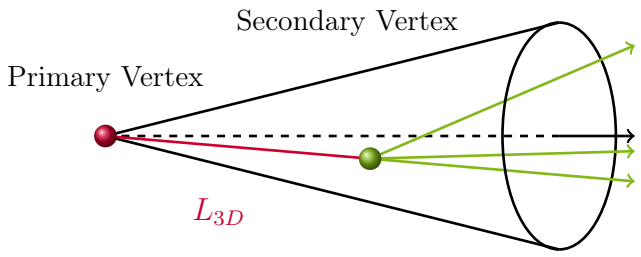

Figure 5.2.: The decay length L_{3D} of a b-hadron is defined as the three-dimensional distance of the fitted secondary vertex, shown in green, to the primary vertex shown in red.

The distance of the SV to the PV is defined as L_{3D} and corresponds to the flight length of a decaying particle as shown in Figure 5.2. The signed flight length significance $L_{3D}/\sigma_{L_{3D}}$ is used as the discriminant for the **SV0** tagging algorithm [66]. While the mistag rate is typically smaller for SV based algorithms its performance is limited by the vertex finding efficiency of about 70% [67].

Additional properties of the SV can be exploited to gain additional discrimination power. The **SV1** algorithm uses a likelihood ratio approach based on the following four variables:

- the invariant vertex mass, computed under the assumption that all associated tracks are pions by adding their four-momenta and calculating the resulting invariant mass,
- the sum of energies of all tracks, associated to the SV, divided by the energy-sum of all tracks in the jet,
- the number of two-track vertex candidates,
- the difference of the jet-direction to the direction of the line connecting the PV with the SV in the $\eta\phi$-plane.

SV1 uses the first two variables in a two-dimensional log-likelihood ratio while the latter two variables are used in independent likelihood definitions.

So far only a SV is considered, where the b-quark undergoes a weak decay most probably into a c-quark as discussed in Section 1.5.2. However, the c-hadron then decays into a light-flavored-hadron, generating an additional decay vertex. Intermediate excited states that undergo strong or electromagnetic transitions are not expected to generate additional vertices due to their short lifetimes. The SV finding algorithm tries to match all displaced tracks to a single inclusive vertex, which does not completely match this b-hadron decay topology. Therefore, the **JetFitter** algorithm utilizes a Kalman-filter [36] to reconstruct a weak b-to-c-to-light-decay chain in a jet [43, 68]. As a result a b-flight axis is iteratively computed and the vertex candidates representing the decay chain are reconstructed as shown in Figure 5.3. This ensures that single tracks can suffice to reconstruct an additional decay step, by fitting a vertex where the track passes the b-flight axis. The algorithm generates six flavor-sensitive variables:

- the number of vertices with at least two tracks,

- the total number of tracks matched to the respective vertex,
- the amount of single track vertices on the b-hadron flight axis,
- the b-decay vertex mass, including all tracks from the complete decay chain,
- the sum of track energies associated to the decay chain divided by the sum over all track energies in the jet,
- the weighted sum of the flight length significances.

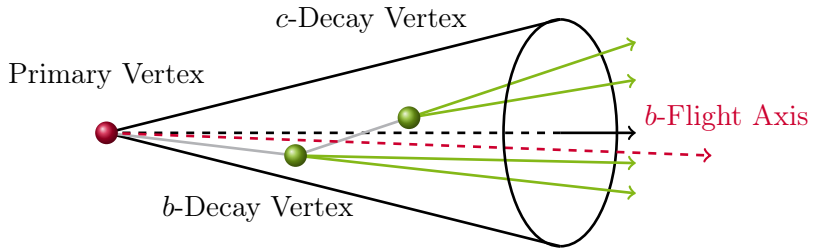

Figure 5.3.: The JetFitter algorithm reconstructs the b-to-c-to-light decay chain by iteratively fitting the b-flight axis, shown in red, and the vertex candidates, shown in green.

Those variables are then combined with the jet p_{T} and η in a **n**eural **n**etwork (NN). To prevent the network from learning the p_{T} and η dependences of the first six variables a two-dimensional re-weighting is applied during the training of the network. The NN has three output nodes for the different flavor hypotheses $P_{b,c,\ell}$. OPs are defined based on the **JetFitter** discriminant $w_{\mathrm{JF}} = \ln(P_b/P_\ell)$.

5.1.3. Muon-based Algorithm

As discussed in Section 1.5.2, the b-hadron decays with a muon in the final state in about 10% of the cases. The kinematic properties of these muons are exploited by the **s**oft **m**uon **t**agger (SMT). When also considering cascade decays where the final state muon is coming from a c-decay the tagging efficiency is limited to about 20% [67]. This is a strong limitation on the overall efficiency. As a result, it is not commonly used in physics analyses. Due to its focus on muon properties it is also highly correlated to the $p_{\mathrm{T}}^{\mathrm{rel}}$-variable itself which therefore cannot reliably be used for calibration. The SMT is only discussed here for completeness.

For the SMT, only combined muons are used that have been measured in the **I**nner **D**etector (ID) and the **M**uon **S**pectrometer (MS) as described in Section 3.4. The muon has to be loosely associated to the PV to reduce the contribution from pile-up. Furthermore, cuts are applied to reduce the contribution of decay-in-flight muons coming from light flavored decays. The classification discriminant is the matching quality for the ID to MS track divided by the number of degrees of freedom $\chi^2_{\text{match}}/N_{\text{DoF}}$ as shown in Figure 5.4. This distribution is broader for light-jets compared to heavy-flavor muons.

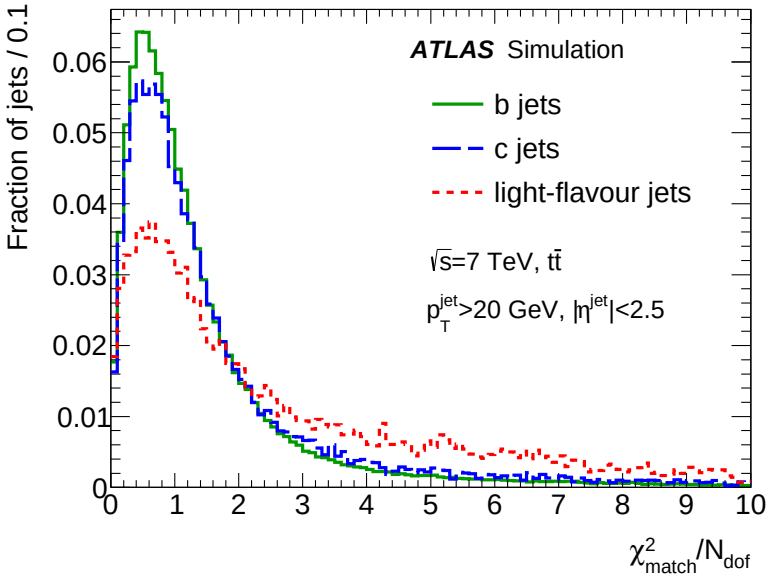

Figure 5.4.: Soft muon tagger matching-χ^2 distribution [64]. The b-, c- and light contributions are shown in green, blue and red, respectively.

5.1.4. Combined Algorithms

The IP-based and SV-based algorithms have different caveats and advantages. While the SV-based algorithms have a lower mistag rate, the IP-based algorithms are not limited by the vertex finding efficiency. Combining both classes of algorithms generates a versatile and more robust type of algorithms with an enhanced classification power.

The **IP3D+SV1** algorithm exploits the fact, that the IP3D and SV1 algorithms both rely on the same log-likelihood ratio technique. The respective output values are summed up to the combined discriminant $w_{\text{IP3D+SV1}} = w_{\text{IP3D}} + w_{\text{SV1}}$ [69].

Another approach for the combination of those classes of algorithms is adding the IP3D discriminant as an input to the **JetFitter** neural network [69]. The resulting network undergoes two different trainings and two different discriminants are defined, based on the three output nodes of the network. The **JetFitterCombNN** uses the same definition as before with $w_{\mathrm{JFCNN}} = \ln(P_b/P_\ell)$ while the **JetFitterCombNNc** is constructed to strongly reduce c-jets at the expense of a degraded light rejection. The discriminant is defined as $w_{\mathrm{JFCNNc}} = \ln(P_b/P_c)$.

The algorithm most commonly utilized in *Run 1* and also in the start of *Run 2* is the **MV1** classifier [64]. It is a NN, based on the perceptron implementation from the **T**oolkit for **M**ulti**v**ariate **A**nalysis (TMVA) [70], to combine the SV1, IP3D and JetFitterCombNN discriminants. An additional input variable is used, categorizing each jet in a two-dimensional grid in (p_{T}, η). The network training relies on back-propagation and is performed on $t\bar{t}$ and high-p_{T} dijet events from **M**onte **C**arlo (MC) simulation. Therefore, the MC samples are re-weighted, as was done for the **JetFitter** algorithm, to avoid any bias from the p_{T} and η distributions. This procedure ensures that the network can learn the input variables independent of the jet's kinematic region while still maintaining the (p_{T}, η)-information for classification. This network has a single output node providing a variable w_{MV1} with a high discrimination power, as shown in Figure 5.5a. This algorithm is again retrained after replacing the JetFitterCombNN with the JetFitterCombNNc as an input variable to construct an algorithm with enhanced c-jet rejection. This is referred to as the **MV1c** algorithm which is commonly used in analyses that have to reduce c-jets as a major background contribution.

For *Run 2*, the new **MV2** algorithm-family was developed. The MV2 classifier is a **b**oosted **d**ecision **t**ree (BDT), implemented in the TMVA framework [70], combining the inputs of previously used algorithms IP2D, IP3D, SV1 and JetFitter rather than combining the outputs as has been done for MV1. Including the jet p_{T} and η, MV2 uses a total of 24 input variables[15]. Also the signal jets are re-weighted to match the background distribution instead of flattening the (p_{T}, η)-spectrum as has been done before. Three different taggers are defined. Therefore, three different trainings are done with different flavor-fractions, which also change from 2015 to 2016 data taking. Therefore, the background sample is defined as a set of light jets with a specific c-contribution, as listed in Table 5.1.

[15]Since the MV2 tagger is under current development the input variables might change.

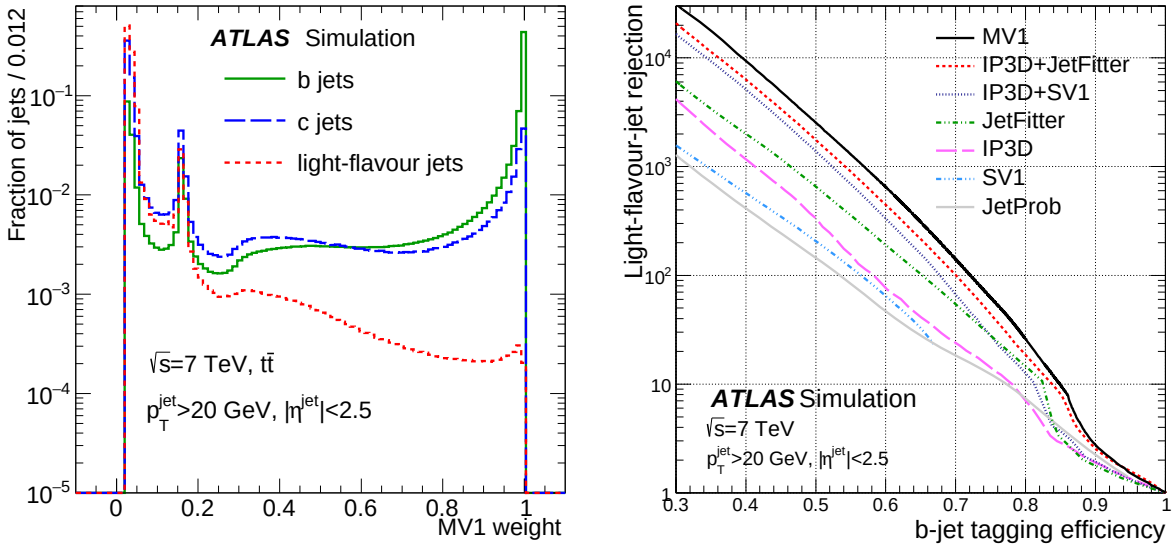

(a) Comparison of the normalized MV1 discriminant for different jet flavor.

(b) ROC curve comparing the performance of multiple tagging algorithms.

Figure 5.5.: The discrimination power of a tagging algorithm can be seen in the difference of its output distribution for different jet flavor as shown for MV1 in (a). A comparison to the performance of other algorithms is shown in (b) [64].

Table 5.1.: MV2c definitions for BDT-trainings with different c-fractions.

c-fraction	MV2c00	MV2c10	MV2c20
2015 training	0%	10%	20%
2016 training	0%	7%	15%

The **MV2c20** tagger was found to have the best trade-off between light- and c-rejection and is commonly used for *Run 2* analyses. It is described including its 2015 and 2016 performance in [71] and [72], respectively.

In general, tagging algorithms are compared using **r**eceiver **o**perating **c**haracteristic (ROC) curves. Therefore, the background rejection, which is usually the light-jet rejection, is plotted against the b-tagging efficiency for varied discriminant thresholds. Each possible cut value in the discriminant corresponds to values (ε_b, R_ℓ) for the respective classifier.

A set of ROC curves is shown in Figure 5.5b, comparing the performance of multiple tagging algorithms, discussed before. The MV1 classifier clearly shows a higher light rejection rate than the other algorithms for every b-tagging efficiency value[16].

5.2. b-Tagging Triggers

Typically, the tagging algorithms discussed before are defined based on offline objects. This has the advantage that algorithms and OPs can be optimized extensively. However, this only changes the number of selected b-jets while the total amount of measured b-jets is already determined during data taking. Therefore, the **T**rigger and **D**ata **Aq**uisition (TDAQ) system has to be optimized to select as many physically relevant events as achievable while simultaneously rejecting as many minimum bias events as possible.

The b-trigger selection is based on online objects starting from **L**evel-**1** (L1) calorimeter jets [73]. Two different trigger modes have been utilized using either the **R**egion **o**f **I**nterest (RoI) defined by the L1 decision, or a **f**ull **s**can (FS) of the complete detector for events triggered by the L1-trigger. The first version is faster than the rather costly FS method. However, both methods have been used during data taking. For the respective b-jet candidates the **L**evel-**2** (L2) and **E**vent **F**ilter (EF) objects are computed and analyzed with online versions of the tagging algorithms discussed before.

During 2011 data taking, the b-trigger selection was based on the JetProb algorithm as shown in Figure 5.6. Three OPs were defined with *loose*, *medium* and *tight* efficiencies corresponding to roughly 70%, 55% and 40% selection efficiency, respectively [64]. It can clearly be seen that the performance of the algorithm strongly increases with each trigger level, up to the offline reconstruction step. In 2012 data taking the SV1+IP3D algorithm was used for trigger selection with a *loose* and a *medium* OP. In 2016 the MV2c algorithm is deployed for trigger selection.

[16] For efficiencies very close to one the JetFitterCombNN tagger has a higher rejection. However, these high efficiencies are not used, due to their limited background rejection capabilities.

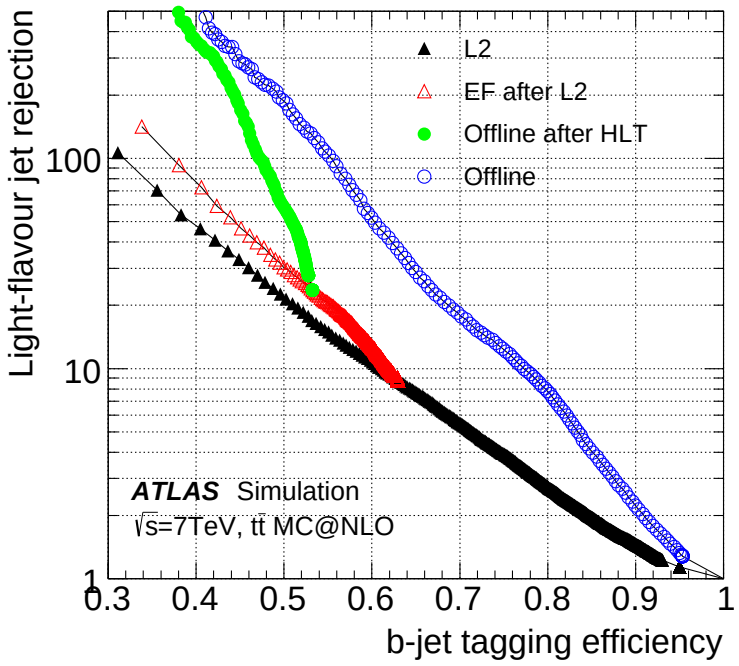

Figure 5.6.: ROC curves for the JetProb algorithm calculated on different trigger steps. The selected events are based on the medium, i.e. 55% efficiency, working point of the **H**igh **L**evel **T**rigger (HLT) [64].

5.3. Flavor Tagging Performance

The previously discussed flavor tagging algorithms are typically characterized on MC samples. Therefore, the different flavor selection efficiencies and their p_{T}, η and pile-up dependencies are evaluated in MC. For sophisticated algorithms using multivariate analysis techniques it is crucial that all input variables and their correlations are described by simulation in high precision since it is a priori unknown which variables or correlations the algorithm is using for discrimination. Therefore, the modeling of observables is extensively studied in [67]. Despite detailed MC studies, the performance is also measured using data-driven methods. The resulting differences in the tagging efficiency ε_{f} for flavor f are computed in form of data to MC **s**cale **f**actors (SFs)

$$\kappa_{\mathrm{f}} = \kappa_{\varepsilon_{\mathrm{f}}}^{\mathrm{data/sim}} = \frac{\varepsilon_{\mathrm{f}}^{\mathrm{data}}}{\varepsilon_{\mathrm{f}}^{\mathrm{sim}}}. \tag{5.2}$$

In general, more than one technique is used to evaluate each of the tagging efficiencies as summarized in [64]. This is done for redundancy and the ability to cross-check various methods and to ultimately combine different measurements.

5.3.1. b-Tagging Efficiency

Apart from the $p_{\mathrm{T}}^{\mathrm{rel}}$-method, multiple other techniques have been used to measure the b-tagging efficiency in ATLAS. Those can be separated into two groups: the $t\bar{t}$-based methods and the μ-based methods. In *Run 1*, the $p_{\mathrm{T}}^{\mathrm{rel}}$-calibration was accompanied by the sytem8-method as a second μ-based technique. In *Run 2*, the system8-calibration is no longer carried out, leaving the $p_{\mathrm{T}}^{\mathrm{rel}}$-method as the only μ-based technique used in ATLAS.

The **system8**-method[17] also relies on the $p_{\mathrm{T}}^{\mathrm{rel}}$-variable as defined in Chapter 7 [75, 76]. Therefore, the event selection is similar to the one described in Chapter 6, requiring non-isolated soft muons, geometrically matched to a jet under study. It uses the following three independent and uncorrelated variables to select a set of eight independent samples as shown in Figure 5.7:

- A soft muon criterion (denoted MT), implemented by a cut on the $p_{\mathrm{T}}^{\mathrm{rel}}$-variable.
- A SV criterion, obtained by a cut on the signed decay length significance $S_{L_{3D}}$. This criterion is applied to a second jet in the event. In the following, n denotes the number of events without applying the cut and p denotes the number of events passing the cut.
- The b-tagging criterion under study (denoted LT), i.e. a combination of a tagging algorithm and the respective OP.

[17] The system8 method was previously known as SystemD method while used by the D0-collaboration [74].

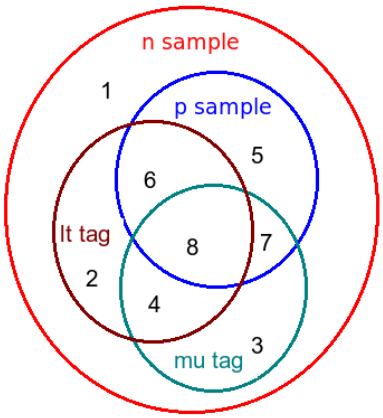

Figure 5.7.: Venn diagram of system 8 selection categories [75]. The MT and LT criteria are denoted as "mu tag" and "lt tag", respectively.

A set of eight equations can be derived:

$$
\begin{aligned}
n &= n_b + n_{c\ell} \\
p &= p_b + p_{c\ell} \\
n^{\mathrm{LT}} &= \varepsilon_b^{\mathrm{LT}} n_b + \varepsilon_{c\ell}^{\mathrm{LT}} n_{c\ell} \\
p^{\mathrm{LT}} &= \alpha_6 \varepsilon_b^{\mathrm{LT}} p_b + \alpha_4 \varepsilon_{c\ell}^{\mathrm{LT}} p_{c\ell} \\
n^{\mathrm{MT}} &= \varepsilon_b^{\mathrm{MT}} n_b + \varepsilon_{c\ell}^{\mathrm{MT}} n_{c\ell} \\
p^{\mathrm{MT}} &= \alpha_5 \varepsilon_b^{\mathrm{MT}} p_b + \alpha_3 \varepsilon_{c\ell}^{\mathrm{MT}} p_{c\ell} \\
n^{\mathrm{LT,MT}} &= \alpha_1 \varepsilon_b^{\mathrm{LT}} \varepsilon_b^{\mathrm{MT}} n_b + \alpha_2 \varepsilon_{c\ell}^{\mathrm{LT}} \varepsilon_{c\ell}^{\mathrm{MT}} n_{c\ell} \\
p^{\mathrm{LT,MT}} &= \alpha_7 \alpha_6 \alpha_5 \varepsilon_b^{\mathrm{LT}} \varepsilon_b^{\mathrm{MT}} p_b + \alpha_8 \alpha_4 \alpha_3 \varepsilon_{c\ell}^{\mathrm{LT}} \varepsilon_{c\ell}^{\mathrm{MT}} p_{c\ell}
\end{aligned}
$$

The eight correction factors α_i account for correlations between the different criteria. The correlations are evaluated on MC and the equations can then be solved numerically. Therefore, a χ^2-criterion is minimized and $\varepsilon_b^{\mathrm{LT}}$ is extracted as described in [75, 76].

Due to the high production cross section under **L**arge **H**adron **C**ollider (LHC) conditions and the high integrated luminosity taken by ATLAS, t-quark pair production can be utilized to measure b-tagging efficiencies. Exploiting the fact that t-quarks mostly decay into b-quarks, different techniques were developed, also documented in [77, 78].

The **tag counting method** assumes that every t-quark decays into a b-quark, hence each $t\bar{t}$-event has two b-jets. The expected signal yields for two tagged jets and

one tagged jet in $N_{t\bar{t}}$ are $\varepsilon_b^2 \cdot N_{t\bar{t}}$ and $2 \cdot \varepsilon_b(1-\varepsilon_b) \cdot N_{t\bar{t}}$, respectively. Multiple effects influence these relations. Acceptance corrections degrade the efficiency of tagging jets while additional $g \to b\bar{b}$ radiation and light and c mistagging generates additional b-jets. This is accounted for by fitting the expected flavor multiplicities F_{ijk} for events with i b-jets, j c-jets and k light jets. The expectation for F_{ijk} is evaluated using MC events.

The **kinematic selection method** relies on the accurate modeling of the flavor composition in MC. The fraction of tagged jets is given by

$$f_{\text{tag}} = \varepsilon_b f_b + \varepsilon_c f_c + \varepsilon_\ell f_\ell + \varepsilon_{\text{fake}} f_{\text{fake}}, \tag{5.3}$$

with the flavor fractions f and the respective tagging efficiencies $\varepsilon_{\cdot}$. The additional fake contribution accounts for jets with non-prompt, fake leptons which is used for the selection of leptonically decaying t-quarks, being estimated in a data-driven approach. Relation (5.3) can be solved for the efficiency

$$\varepsilon_b = \frac{1}{f_b}(f_{\text{tag}} - \varepsilon_c f_c - \varepsilon_\ell f_\ell - \varepsilon_{\text{fake}} f_{\text{fake}}). \tag{5.4}$$

This efficiency is then measured in bins of p_{T} and η using flavor fractions from simulation as well as efficiencies, which are in addition corrected using data to MC scale factors.

The **kinematic fit method** exploits the kinematic decay properties and fits the reconstructed objects to the decay topology using t- and W-masses as additional constraints. As a result, b-jet candidates are obtained by kinematic properties only, without the usage of dedicated tagging algorithms. The $t\bar{t}$ semileptonic decay channel is used for this method. After fitting the most probable object permutation, the b-tagging efficiency is measured using the b-jet candidate on the leptonic side of the event. This method has a combinatorial background in addition to backgrounds from other physics processes. Therefore, the hadronical side of the decay is separated into a signal enriched sample and a background enriched sample using multiple combinations of b-tagging criteria and b-tagging vetoes. A side-band in the matching χ^2 distribution is used to normalize the background expectations which can then be subtracted from the signal distribution. After background subtraction the tagging efficiency is calculated by integrating the signal yields in the tagging discriminant distribution $T(w)$

$$\varepsilon_b(w_{\text{cut}}) = \int_{w_{\text{cut}}}^{\infty} T(w)\,\mathrm{d}w. \tag{5.5}$$

The **combinatorial likelihood method** reaches the highest precision of the discussed efficiency calibrations. The event selection is based on the $t\bar{t}$ dileptonic decay channel. The calibration is carried out in ee, $\mu\mu$ and $e\mu$ final states. Furthermore, the effect of additional radiation is taken into account by performing the measurement independently in topologies with two and three jets. This technique relies on per-event likelihood functions that have to be defined separately for the different jet multiplicities due to different amount of possible permutations. The two jet likelihood is defined as

$$\begin{aligned}\mathcal{L}(p_{\mathrm{T},1}, p_{\mathrm{T},2}, w_1, w_2) &= \frac{1}{2}\sum_{(j,k)}[f_{\mathrm{bb}}\mathcal{P}_{\mathrm{bb}}(p_{\mathrm{T},i}, p_{\mathrm{T},k})\mathcal{P}_{\mathrm{b}}(w_i|p_{\mathrm{T},i})\mathcal{P}_{\mathrm{b}}(w_k|p_{\mathrm{T},k}) \\ &+ f_{\mathrm{bj}}\mathcal{P}_{\mathrm{bj}}(p_{\mathrm{T},i}, p_{\mathrm{T},k})\mathcal{P}_{\mathrm{b}}(w_i|p_{\mathrm{T},i})\mathcal{P}_{\mathrm{j}}(w_k|p_{\mathrm{T},k}) \\ &+ f_{\mathrm{jj}}\mathcal{P}_{\mathrm{jj}}(p_{\mathrm{T},i}, p_{\mathrm{T},k})\mathcal{P}_{\mathrm{j}}(w_i|p_{\mathrm{T},i})\mathcal{P}_{\mathrm{j}}(w_k|p_{\mathrm{T},k})] \end{aligned} \tag{5.6}$$

with the following ingredients:

- The sum is executed over the permutations (1,2) and (2,1). In the three jet case, additional permutations have to be taken into account.
- The jet flavor fractions f for the possibilities b-jet or non-b-jet. The non-b-jet is simply denoted as jet j.
- The probability density functions $\mathcal{P}_{\mathrm{f}}$ for the b-tagging discriminant for a jet of flavor f in dependence of the jet transverse momentum.
- The two-dimensional probability density functions $\mathcal{P}_{\mathrm{f_1 f_2}}$, depending on the two jet flavors and their respective p_{T} values.

The probability density functions used for this approach are extracted from MC distributions. Only the measured probability density function for the b-jet discriminant is estimated in data and the tagging efficiency can be computed by the integral

$$\varepsilon_b = \int_{w_{\mathrm{cut}}}^{\infty} \mathcal{P}_b(w, p_{\mathrm{T}})\,\mathrm{d}w. \tag{5.7}$$

5.3.2. c-Tagging Efficiency

The c-jet tagging efficiency ε_c is measured by two different methods. The first method uses a selection enriched with final states where a c-quark is produced in association with an on-shell W-boson [79]. The dominant production channels are $gs \to W^- c$ and $g\bar{s} \to W^+ \bar{c}$. The c-hadron is required to decay with a muon in the final state, which can be matched with a geometric cone algorithm to the produced c-jet. The $W^\pm$ is required to decay leptonically with exactly one isolated electron to avoid ambiguities with the muon in the event. Additional **m**issing $\boldsymbol{E_T}$ (MET) is required to account for the neutrinos. While the muon has an electrical charge with the same sign as the produced c-quark, the electron has the opposite electrical charge. As a result, the muon and electron in the final state are of **o**pposite **s**ign (OS) with respect to their electrical charge. In contrast, the background is distributed symmetrically between OS and **s**ame **s**ign (SS) final states. This asymmetry in the event yields of the signal process can be exploited to remove the background yield $N_{\mathrm{OS}}^{\mathrm{bkg}} = N_{\mathrm{SS}}^{\mathrm{bkg}} = N_{\mathrm{SS}}^{\mathrm{total}}$. As a result the signal yield can be found as

$$N_{\mathrm{OS}}^{Wc} \;=\; N_{\mathrm{OS}}^{\mathrm{total}} - N_{\mathrm{SS}}^{\mathrm{total}}. \tag{5.8}$$

This way the amount of c-jets in a selected sample can be evaluated. This technique is used to compute the c-yield before and after a tagging algorithm is applied to calculate the efficiency

$$\varepsilon_c \;=\; \frac{N_{Wc}^{\mathrm{tag}}}{N_{Wc}^{\mathrm{total}}}. \tag{5.9}$$

A second method to determine the c-tagging efficiency is to measure the D^{*+}-yield before and after tagging [80, 81]. Therefore, the $D^{*+} \to D^0(\to K^-\pi^+)\pi^+$ process is selected by fitting the measured tracks to the expected decay chain. For the resulting candidates the invariant mass difference $m(K\pi\pi) - m(K\pi)$ is used to evaluate the background by fitting it in a side-band, 3σ away from the invariant mass signal peak, as seen in Figure 5.8a. For the background-subtraction a distribution of events from the side-band region is normalized to the fitted background fraction in the signal region and is then subtracted from the data distribution in the D^0 pseudo-proper time

$$t(D^0) \;=\; \mathrm{sign}\left(\vec{L}_{xy}(D^0) \cdot \vec{p}_{\mathrm{T}}(D^0)\right) \cdot m_{D^0} \frac{L_{xy}(D^0)}{p_{\mathrm{T}}(D^0)}, \tag{5.10}$$

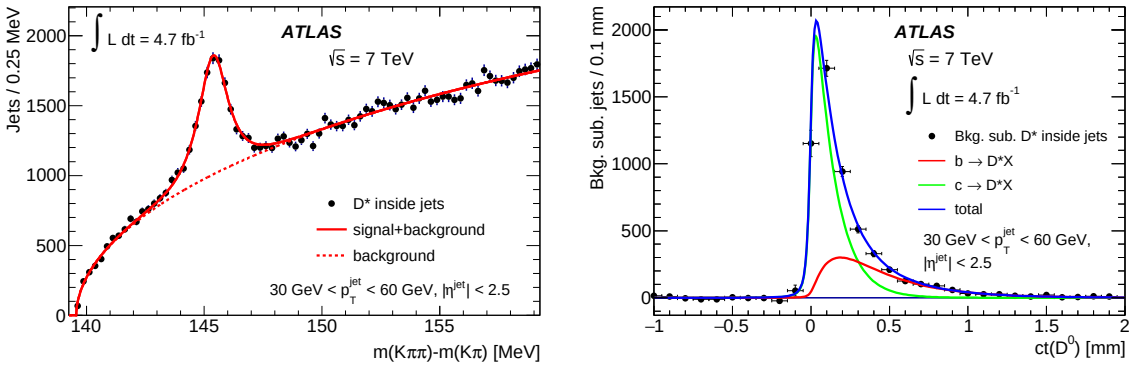

(a) Difference in the invariant mass Δm for D^{*+} candidates.

(b) D^0 pseudo proper time distribution with fitted flavor fractions.

Figure 5.8.: For the D^{*+} analysis the background is subtracted using a fit in the missing mass difference (left) while the flavor fractions are fitted in the pseudo proper time (right) [64].

with the meson mass m_{D^0} and L_{xy} being the distance between the D^0 decay vertex and the PV in the transverse plane. Since the pseudo-proper time loosely corresponds to the decay time in the particle rest frame, exponential functions convoluted with dedicated resolution functions can be utilized to fit the different flavor fractions, as shown in Figure 5.8b. As a result, the efficiency to tag D^{*+}-mesons $\varepsilon_{D^{*+}}$ is determined. Since those mesons can also be produced in b-hadron decays, the c-tagging efficiency can be found using

$$\varepsilon_{D^{*+}} \quad = \quad f_b \varepsilon_b + (1 - f_b)\varepsilon_c, \tag{5.11}$$

with the fitted b-fraction f_b while ε_b is evaluated on simulation. This equation is then solved for ε_c.

5.3.3. Mistag Rate

The mistag rate describes the number of light jets that are falsely tagged as a b-jet. This is equal to the light-tagging efficiency ε_ℓ, which is calibrated using the **negative tag method** [81, 82]. This technique exploits the fact that the IP and SV reconstruction for light jets is limited by resolution effects. Therefore, the signed impact parameter significance $S_{d_{3D}} = d_{3D}/\sigma_{d_{3D}}$ and signed decay length significance $S_{L_{3D}} = L_{3D}/\sigma_{L_{3D}}$ are randomly distributed within the resolution range around zero.

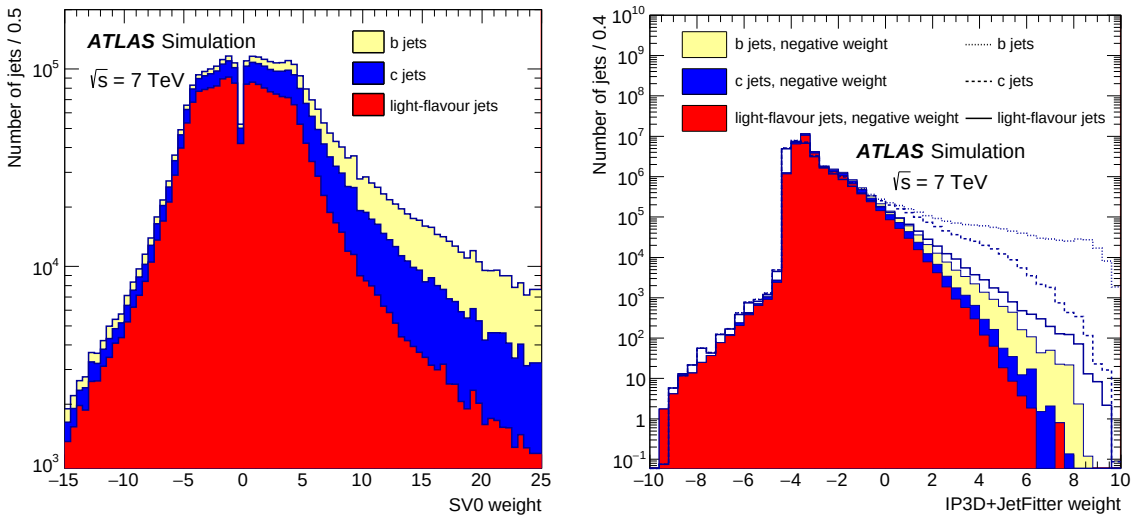

(a) Distribution of the SV0 discriminant.

(b) Negative tag and standard version of the JetFitterCombNN discriminant.

Figure 5.9.: The JetFitterCombNN discriminant on the right changes due to the negative tag weighting in the input variables [64].

In contrast, b- and c-contributions are shifted to higher values due to the decay properties of heavy flavor hadrons, as shown in Figure 5.9a. For the negative tag method the signed impact and decay length significances are redefined to $\overline{S_{d_{3D}}} = -S_{d_{3D}}$ and $\overline{S_{L_{3D}}} = -S_{L_{3D}}$, inverting their sign. This slightly affects the random, resolution limited distribution for light jets but has a bigger impact on the heavy flavor distributions, as seen in Figure 5.9b. As a result, the impact on the probability of falsely tagging light jets is very small, while the probability of tagging heavy flavor jets is vastly decreased. The mistag rate can be approximated by the tagging efficiency under these negative tag conditions $\varepsilon_\ell \cong \varepsilon_\ell^{\text{neg}}$. To increase the precision of this measurement two additional correction factors are applied, which have to be estimated in simulation. The factor k_{hf} corrects for heavy flavor contributions in the negative tagged distribution and k_{ll} accounts for long-lived light particles like K_{s}^0.

An alternative approach uses the discriminating power of the **SV0 mass** to estimate flavor fractions [82]. The light and heavy flavor distributions are different and templates are generated from simulation. A template fit to the data distributions before and after tagging provides an effective measure of the light tagging efficiency $\varepsilon_\ell = N_\ell^{\text{tag}}/N_\ell^{\text{total}}$.

6. Event and Object Selection

Ein guter Mensch, in seinem dunkeln Drange,
Ist sich des rechten Weges wohl bewußt.

DER HERR

During data taking multiple kinds of events are recorded, covering a variety of physics processes and phase-space regions. For this thesis, a set of events containing b-hadrons produced in QCD-dominated phase-space is selected. Since the $p_{\mathrm{T}}^{\mathrm{rel}}$-method relies on a muon in the final state, it is a necessity to have a muon in the jet under study. Since the b-hadron decay is independent from its production, this only introduces a minor kinematic bias as discussed in Chapter 9. Events are selected from recorded ATLAS data using a **g**ood **r**uns **l**ist (GRL) which rejects events taken during non-physics operation or unscheduled downtime of detector components.

6.1. Trigger Selection

For the event selection muon-in-jet triggers are used[18]. These triggers are seeded by a low threshold **L**evel-**1** (L1) muon trigger. Due to the high hadronic activity in proton-proton collisions, multiple jet candidates are usually measured in each event. Those are picked up and a cone based matching to the muon is carried out. An additional cut on the z_0 **i**mpact **p**arameter (IP) is applied to reduce random combinatorial background from pile-up events. This occurs when a jet from a pile-up vertex flies into the same $\eta\phi$-direction as the muon from the **p**rimary **v**ertex (PV).

These triggers are referred to as HLT_mu$x$_jy_dr05_dz02 where x stands for the muon momentum threshold and y for the jet momentum threshold. There are multiple instances of these triggers with different thresholds x and y and hence different prescale factors. The "dr05" means that a matching in the $\eta\phi$-plane with a cone radius of 0.5 is required, i.e. the jet and the muon are flying in the same direction. In addition, a cut on the z-position has been applied with a 2 mm threshold to ensure both are

[18] As discussed in Section 2.2.5 the trigger set-up changes in time. However, the basic principal and usage of the muon-in-jet triggers for this analysis remain the same.

originating from the same vertex. Since only the p_{T}-thresholds change in between the triggers they are in short referred to as mu$x$ jy. The leading jet spectrum for multiple muon-in-jet **H**igh **L**evel **T**riggers (HLTs) is shown in Figure 6.1. It can be observed that the triggers have broad turn-on regions where the trigger becomes increasingly efficient. The trigger turn-on is broadened in leading jet-p_{T} since the trigger selects events based on matched objects while there might be jets in the event with higher momentum.

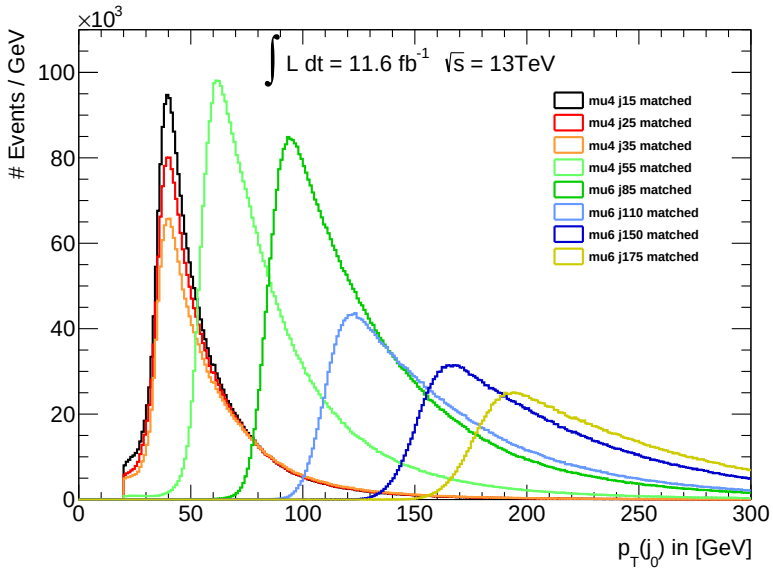

Figure 6.1.: Leading jet spectrum for data taken in early 2016 with $\sqrt{s} = 13\,\mathrm{TeV}$. Events taken by different muon-in-jet triggers are shown in different colors. The trigger yield is given by the area under the respective curve.

Due to the pre-scale factors the yield of recorded events is only a fraction of the observed events in a given time period. Since the $p_{\mathrm{T}}^{\mathrm{rel}}$-method relies on ratios of event yields those pre-scales cancel out and are not corrected for. Therefore, the integrated luminosities quoted in the following discussions correspond to the integrated luminosity of the utilized dataset as recorded by ATLAS, rather than the integrated luminosity of the shown physics processes. For the event selections one specific trigger is used in each jet p_{T} region. It is chosen by maximizing the yield while ensuring that the trigger is fully efficient.

6.2. Jet Selection

For the $p_{\mathrm{T}}^{\mathrm{rel}}$-measurement anti-$k_t$ jets are used with a cone radius of 0.4, as described in Chapter 3.3. For this thesis, only topological clusters based on calorimeter cells are used. In *Run 1* the emphasis was on **l**ocally **c**alibrated (LC) jets while in *Run 2* jets calibrated at the **e**lectro**m**agnetic (EM) scale was utilized more broadly. In addition, trigger level jets have been used for $p_{\mathrm{T}}^{\mathrm{rel}}$-measurements.

Jets are always required to have at least $p_{\mathrm{T}}^{\mathrm{jet}} > 20\,\mathrm{GeV}$ and $|\eta^{\mathrm{jet}}| < 2.5$. In order to suppress pile-up events the **J**et **V**ertex **F**raction (JVF) and **J**et **V**ertex **T**agger (JVT) criterion has been applied in *Run 1* and *Run 2*, respectively.

6.3. Muon Selection and Identification

Muons are the key items for the $p_{\mathrm{T}}^{\mathrm{rel}}$-method. In contrast to prompt muon production in hard scattering processes, generating a hard and isolated muon, here muons from b-hadron decays inside a jet are selected. The high amount of hadronic activity hampers the identification of the muon of interest. Due to their high abundance in jets and their high **b**ranching **r**atio (BR) into muon final states the charged $\pi^{\pm}$ and $K^{\pm}$ can produce muons inside a jet. Considering their huge life times the decay mostly happens after the first layers of the **I**nner **D**etector (ID). Therefore, **c**om**b**ined (CB) muons are selected, ensuring that the muon track can already be resolved in the ID, rejecting muons from long-lived light hadrons, as described in Chapter 3.4.

Another criterion to suppress background from pion and kaon decays is the muon identification. Typically a track is reconstructed for a charged light flavor meson traversing the ID. This meson decays during its flight through the detector and a track from the emerging muon is measured in the **M**uon **S**pectrometer (MS). In cases where these two track segments match each other, the following criteria are used to reject this decay-in-flight events:

- The q/p-significance is defined as difference in the charge over momentum ratio as measured by the different detector parts $|(q/p)_{\mathrm{ID}} - (q/p)_{\mathrm{MS}}|$, divided by quadratic sum of their uncertainties.

- The ρ', defined as the momentum difference divided by the momentum of the CB track $(p_{\mathrm{T}}^{\mathrm{ID}} - p_{\mathrm{T}}^{\mathrm{MS}})/p_{\mathrm{T}}^{\mathrm{CB}}$.

- The normalized χ^2 as calculated in the combined fit.
- Additional requirements to the number of hits in the layers of the ID.

These criteria are used to define the inclusive identification selections *loose*, *medium* and *tight* as described in [51, 52]. For the $p_{\mathrm{T}}^{\mathrm{rel}}$-analysis the *tight* criterion is chosen, with a muon selection efficiency of about 90%, to reduce the amount of decay-in-flight events as much as possible. In addition, a dynamical muon p_{T}-cut is applied. For low p_{T} jets the muon threshold has to be low as well. Therefore, a cut at $p_{\mathrm{T}}(\mu) > 5\,\mathrm{GeV}$ ($> 4\,\mathrm{GeV}$ in *Run 1*) is used. For an increasing jet momentum the muon threshold is increased in two steps as listed in Table 6.1. The pseudorapidity is also limited to $|\eta(\mu)| < 2.5$. The muon is then geometrically matched to a jet using a cone based algorithm. In addition, cuts on the differences of the IPs are defined $|\Delta d_0| < 2\,\mathrm{mm}$ and $|\Delta(z_0 \sin(\theta))| < 2\,\mathrm{mm}$. These cuts are very loose to reduce pile-up while not biasing the flavor tagging algorithms.

Table 6.1.: Cut values for $p_{\mathrm{T}}(\mu)$ depending on the jet momentum bins used in *Run 1* and *Run 2*.

Jet p_{T} in *Run 1*	Jet p_{T} in *Run 2*	Muon p_{T} cut value
20 - 60 GeV	20 - 40 GeV	4/5 GeV
60 - 90 GeV	40 - 90 GeV	6 GeV
90 - 200 GeV	90 - 200 GeV	8 GeV

6.4. Backtag Criterion

An additional selection criterion is applied to increase the b-fraction in the dataset. In a "standard" analysis this would be done by selecting b-tagged jets. This direct approach could introduce a bias to the efficiency measurement and is not suited for the $p_{\mathrm{T}}^{\mathrm{rel}}$-method. The b-quark is dominantly produced in pairs via the strong interaction, as discussed in Chapter 1.5.1. Hence, an event containing a b-quark most likely contains a second b-quark. This is exploited in a tag-and-probe approach. To avoid confusion with the b-tagging criterion under study the tag jet is denoted as a **b**ack**t**ag (BT) jet. The BT jet is determined as a jet passing a high efficiency b-tagging algorithm IP3D+SV1, as described in Section 5.1.

In case of multiple jets passing the tagger, jets without a matched muon are preferred. If there are still multiple candidates remaining, the BT jet is chosen randomly. Since the BT criterion is highly correlated to the tested algorithm, the BT jet is not used for the measurement. The probe jets are the remaining jets with a matched muon passing all the previous cuts. These muon and jet combinations are referred to as $p_{\mathrm{T}}^{\mathrm{rel}}$-candidates. Figure 6.2 shows the b-fraction of jets from the muon-filtered **M**onte **C**arlo (MC) in blue. Adding the BT criterion with a loose, medium or tight cut on the IP3D+SV1 discriminant increases the fraction of b-jets, as shown in green, red and black, respectively.

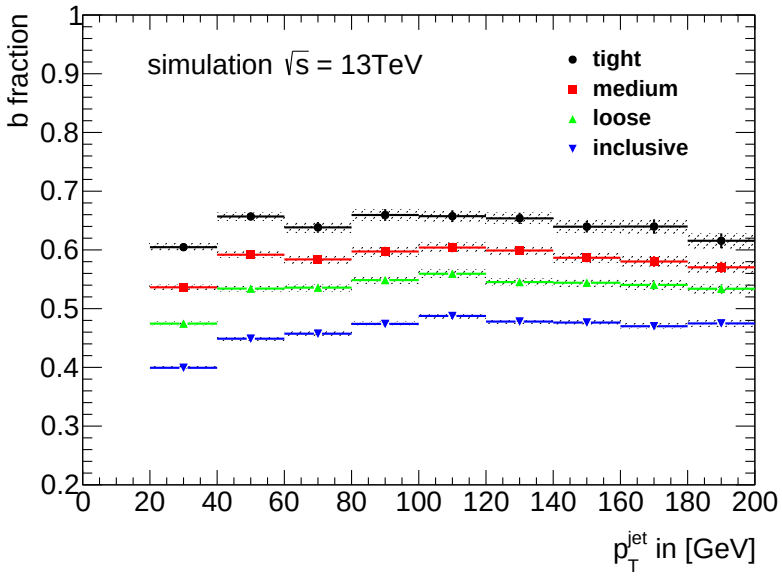

Figure 6.2.: Fraction of b-jets determined for different BT cut values. Based on the muon-filtered MC a loose, medium or tight cut on the IP3D+SV1 discriminant is used to increase the b-fraction.

The BT is also exploited for a data-driven generation of the light template, as described in Chapter 7.1.2. Therefore, the selection criterion is inverted and only events not having a BT jet are probed, minimizing the amount of heavy flavor jets in the sample while generating a dataset disjoint to the signal region.

6.5. Semileptonic Correction

Due to the semileptonic decay of the b-hadron its four-momentum can not completely be measured. The muon is measured and reconstructed separately to the hadronic activity of the jet and the neutrino is not measured at all. However, the available information from the different detector components can be combined to improve the calibration measurement. This is exploited for two different aspects of the analysis, the calculation of the $p_{\mathrm{T}}^{\mathrm{rel}}$-variable and the definition as the $p_{\mathrm{T}}^{\mathrm{jet}}$ as a proxy for the b-hadron momentum.

As discussed before, the $p_{\mathrm{T}}^{\mathrm{rel}}$-candidate contains a muon within the jet cone. Therefore, the muon also passes the calorimeter in the region where the jet energy is measured. Since the muon is minimal ionizing it deposits a small amount of energy in the calorimeter. However, for an accurate measurement of the $p_{\mathrm{T}}^{\mathrm{rel}}$ this has to be taken into account. This is achieved by subtracting the energy loss expected for a **m**inimal **i**onizing **p**article (MIP) depending on the amount of material in the respective flight direction [83]. The momentum of the muon itself as measured by the MS is then added to the corrected jet four-momentum. These corrections are carried out to get a better estimate for the b-hadron direction, necessary for an exact calculation of $p_{\mathrm{T}}^{\mathrm{rel}}$.

In *Run 1*, the jet+muon four momentum is also scaled by an all-particle response function to account for the missing neutrino. This function is evaluated on simulation as the ratio of the $p_{\mathrm{T}}^{\mathrm{jet+muon}}$ divided by the combined momentum of all truth particles including the neutrino. Therefore, this correction only scales the momentum and has no effect on the calculation of $p_{\mathrm{T}}^{\mathrm{rel}}$ itself. Instead, it was only used to scale the $p_{\mathrm{T}}^{\mathrm{jet}}$ to get a better estimate for the b-hadron momentum. These response functions have to be computed in dedicated studies which have not been fully adapted to *Run 2* conditions at this point[19]. Therefore, it was decided to keep the uncorrected $p_{\mathrm{T}}^{\mathrm{jet}}$ as measured by the calorimeter as the proxy for the b-hadron momentum for the current stage of the analysis in *Run 2*.

[19] Early efforts for the semileptonic correction of b-jets are ongoing and internally documented in [84].

7. The $p_{\mathrm{T}}^{\mathrm{rel}}$-Method

Wie alles sich zum Ganzen webt,
Eins in dem andern wirkt und lebt!
Wie Himmelskräfte auf und nieder steigen
Und sich die goldnen Eimer reichen!

FAUST

The $p_{\mathrm{T}}^{\mathrm{rel}}$-variable is defined for muons that are associated to a jet by geometrically matching in the $\eta\phi$-plane, using a cone algorithm. For a muon inside a jet, the $p_{\mathrm{T}}^{\mathrm{rel}}$-variable is computed as the muon momentum component transversal to the combined muon plus jet momentum as shown in red in Figure 7.1.

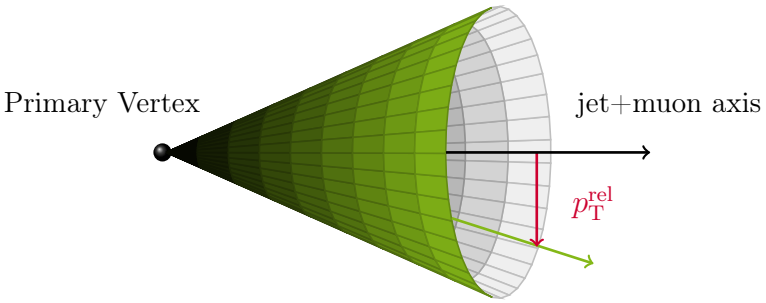

Figure 7.1.: The $p_{\mathrm{T}}^{\mathrm{rel}}$-variable is defined as the projection of the muon momentum transversal to the combined jet+muon axis shown in black. This relies on the momentum measurement and no spacial information on the decay vertex is needed. The muon track is shown in green while the transversal component is highlighted red.

From the three momentum components $\vec{p} = (p_x, p_y, p_z)$ of the four-vectors of the corrected jet vector $\vec{p_{\mathrm{j}}}$ (including the semileptonic correction as discussed in Section 6.5) and the muon vector $\vec{p_\mu}$ the transversal projection can be found as

$$p_{\mathrm{T}}^{\mathrm{rel}} = \sqrt{\vec{p}_{\mu}^{\,2} - \left(\frac{\vec{p}_{\mathrm{j}} \cdot \vec{p}_{\mu}}{|\vec{p}_{\mathrm{j}}|}\right)^2}. \tag{7.1}$$

This variable depends on the production mechanism of the respective muon. Direct muon production has a smaller cross section compared to multi-jet production. In addition, the event selection rejects combinatorial background where a random jet direction coincides with a prompt muon. Therefore, $p_{\mathrm{T}}^{\mathrm{rel}}$-candidates are dominantly produced in decays of hadrons inside the jet. The $p_{\mathrm{T}}^{\mathrm{rel}}$-value after the decay is correlated to the mass of the decaying hadron. Hence, the $p_{\mathrm{T}}^{\mathrm{rel}}$-distribution for muons coming from b-hadron decays is harder than for muons from light or c-flavored jets. This difference is then exploited in a binned log-likelihood template fit. The templates for the different flavor hypotheses are created using simulation and data-driven techniques discussed below. The fit is sensitive to the flavor fractions in a sample of $p_{\mathrm{T}}^{\mathrm{rel}}$-candidates. By measuring the b-fraction before and after applying a b-tagging criterion, the tagging efficiency ε_b can be derived. Jets passing the combination of tagging algorithm and **o**perating **p**oint (OP) under study are denoted as "tagged" while jets not matching the criterion are denoted "untagged".

In *Run 2*, the most commonly utilized tagging discriminant is the MV2 algorithm. Which is mostly used with the training with roughly one fifth charm background as discussed in Section 5.1. The output of the **b**oosted **d**ecision **t**ree (BDT) is used as the discriminant for the different flavor hypotheses as shown in Figure 7.2a. While it is clear that there is a correlation to the $p_{\mathrm{T}}^{\mathrm{rel}}$-variable since both are sensitive to the jet-flavor, it is necessary that the correlation is small. In Figure 7.2b, the correlation for jets passing the $p_{\mathrm{T}}^{\mathrm{rel}}$-selection is shown to be about 26%. It has been validated in simulations that there is a negligible correlation for the independent flavor hypotheses but the overall correlation is purely generated by the different jet flavors populating different regions in the $p_{\mathrm{T}}^{\mathrm{rel}}$-MV2-plane as would be expected for two flavor-sensitive variables.

The $p_{\mathrm{T}}^{\mathrm{rel}}$-method has been used by the CDF and D0 experiments and has been proven as a reliable measurement of the b-tagging efficiency (see e.g. [85]). Therefore, it has been recommended for usage at the **L**arge **H**adron **C**ollider (LHC) [86]. Calibration measurements have been conducted using ATLAS data by scientists at the University of Dortmund in *Run 1* conditions. These are documented to varying extent in [87–89]. Measurements using ATLAS data are also discussed in [64, 76].

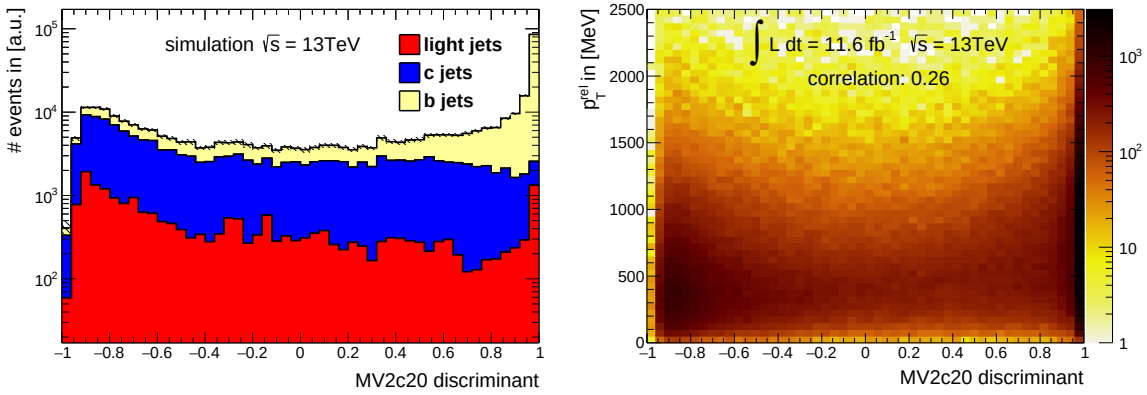

(a) Output of the MV2c20 algorithm.

(b) Correlation between MV2 and $p_{\mathrm{T}}^{\mathrm{rel}}$.

Figure 7.2.: The output of the MV2c20 algorithm for b-, c-, and light-jets shown in yellow, blue, and red, respectively (left). The distribution is scaled to arbitrary units. On the right, the correlation between MV2c20 and the $p_{\mathrm{T}}^{\mathrm{rel}}$-variable is shown. Data is recorded with the mu4 j15 trigger using $p_{\mathrm{T}}^{\mathrm{rel}}$ event selection without applying a **b**ack**t**ag (BT).

7.1. Template Generation

Templates are probability density functions of the $p_{\mathrm{T}}^{\mathrm{rel}}$-variable for the different flavor-hypotheses. The light- and c-templates are very similar in their shape and therefore, the $p_{\mathrm{T}}^{\mathrm{rel}}$-method is not sensitive to their relative flavor-fractions. For this reason, the fit is performed using b- and non-b-templates which have to be derived in multiple steps. All templates are generated in a range of the transverse jet momentum of the respective candidate jet. This way, the measurement can be conducted in various $p_{\mathrm{T}}^{\mathrm{jet}}$-regions.

7.1.1. Heavy Flavor Templates

The templates for the b- and c-flavor distributions are generated using simulations. Here, the di-jet **M**onte **C**arlo (MC) with the muon filter applied on generator level, as introduced in Section 4.2, is used. The generator filter increases the amount of $p_{\mathrm{T}}^{\mathrm{rel}}$-candidates which allows extracting the shape of the two templates with higher statistical precision. The jet flavor is determined by cone based truth-matching as discussed in Section 4.3.

7.1.2. Data-Driven Light-Template

The template for the light-flavor hypothesis is extracted in a data-driven approach. To achieve this, a phase-space region disjoint to the signal region is defined by inverting the BT criterion discussed in Section 6.4. Selecting $p_{\mathrm{T}}^{\mathrm{rel}}$-candidates in this region generates a template dominated with light-flavor jets with only a small heavy-flavor contribution. The expected contamination of b-jets in the light template is evaluated in simulations. For that, the same phase-space region is selected in the unfiltered di-jet MC as is used to extract the light template from data. Figure 7.3 shows the expected contamination of b-jets in the light template as a function of $p_{\mathrm{T}}^{\mathrm{jet}}$. As can be seen, the b-contamination in the light-template is expected to be in the order of few percent (as shown by the red dots) and the choice of the BT cut value is found to be negligible. There is also no strong dependence on the jet momentum as can be seen by the linear extrapolation (shown in green with a 1σ error band). The fit indicates a b-fraction of about 4-6% which is compatible with the results found in *Run 1* at a lower center of mass energy [64, 76]. The light-template is corrected for these heavy flavor contaminations by subtracting the b- and c-templates in the respective amounts before doing the fit.

7.1.3. Light-to-Charm Ratio and the Non-b-Template

Since the shapes of the light- and c-template are very similar, the fit is not sensitive to the relative fractions. That is why the ratio of light- to c-jets has to be determined separately. The light-template is generated in a data-driven approach leading to the fact that the relative normalization in the signal region is not known. The c-template is extracted from simulation with a muon filter applied on generator level, which introduces a bias to the relative flavor abundances. Hence, the unfiltered di-jet MC samples introduced in Section 4.1 are used to compute the light-to-charm ratio, also denoted ℓc-ratio for short. With the p_{T}-dependent ℓc-ratio extracted from the signal region in simulation, the light- and c-templates are combined with the respective flavor fractions generating a combined non-b-template.

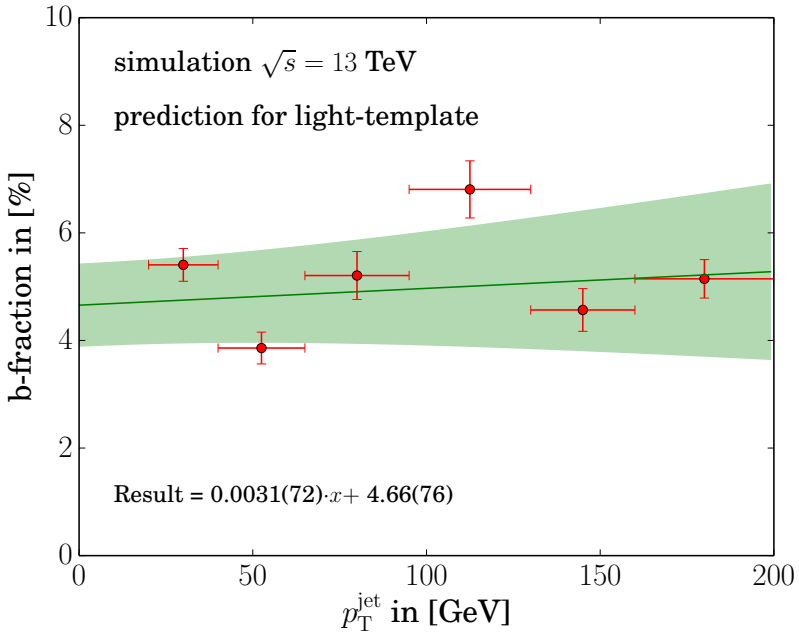

Figure 7.3.: Contamination of b-jets expected in the light-template shown in red. The b-fraction is determined based on unfiltered di-jet MC by inverting the BT cut criterion. No strong dependence on the jet momentum is found by a linear fit (green line) and the b-contamination is compatible with 4-6% as indicated by the linear fit function and the 1σ error band shown in green.

7.2. Likelihood Definition and Fit

All proton-proton-collisions are statistically independent which results in the amount of observed events following a Poisson distribution. Therefore, the probability of observing k events for a given expectation value λ is given as

$$P(k, \lambda) = \frac{\lambda^k}{k!} \exp(-\lambda). \tag{7.2}$$

While in the measurement only the observed number of events is known, a likelihood $\mathcal{L}$ for the expectation value given k is found to be

$$\mathcal{L}(\lambda|k) = \frac{\lambda^k}{k!} \exp(-\lambda). \tag{7.3}$$

The logarithm is a continuously differentiable real function with strictly increasing behavior. Hence, maximizing the log-likelihood gives the same result as maximizing

the likelihood itself. However, while the likelihood of multiple outcomes is multiplicative, the log-likelihood is summed for multiple independent observations. Using the logarithm to the base e, one can find

$$\log \mathcal{L}(\lambda|k) = -\log k! + k \log \lambda - \lambda, \tag{7.4}$$

which is maximized by the expectation value being the observed value as can be found by the derivative

$$\frac{\partial \mathcal{L}(\lambda|k)}{\partial \lambda} = \frac{k}{\lambda} - 1. \tag{7.5}$$

For the template fit, the templates are normalized to the $p_{\mathrm{T}}^{\mathrm{rel}}$-distribution measured in data. The expectation value in the ith $p_{\mathrm{T}}^{\mathrm{rel}}$-bin $\lambda_i(f_b)$ is defined as the sum of the b- and non-b-templates with a varied fraction f_b. The first term in Equation (7.4) is a constant value which can be dropped giving the log-likelihood

$$\log \mathcal{L}_i(\lambda_i(f_b)|N_i^{\mathrm{data}}) = N_i^{\mathrm{data}} \log \lambda_i(f_b) - \lambda_i(f_b), \tag{7.6}$$

$$\text{with} \quad \lambda_i(f_b) = f_b \cdot N_i^b + (1 - f_b) \cdot N_i^{\text{non-b}}. \tag{7.7}$$

The log-likelihood is summed over all $p_{\mathrm{T}}^{\mathrm{rel}}$-bins using one value of f_b. N_i denotes the number of events in the ith $p_{\mathrm{T}}^{\mathrm{rel}}$-bin for the data or the respective template. The resulting likelihood $\mathcal{L}(f_b)$ is then maximized to extract the most probable value of the b-fraction f_b.

7.3. Template Fit

The resulting templates differ in shape for the different flavor-hypotheses as shown in Figure 7.4. As can be seen, the light- and c-template (shown in red and blue, respectively) are similar to each other and are therefore combined using a predetermined ℓc-ratio. In contrast, the b-template (yellow) differs in shape, which generates the discrimination power of the method.

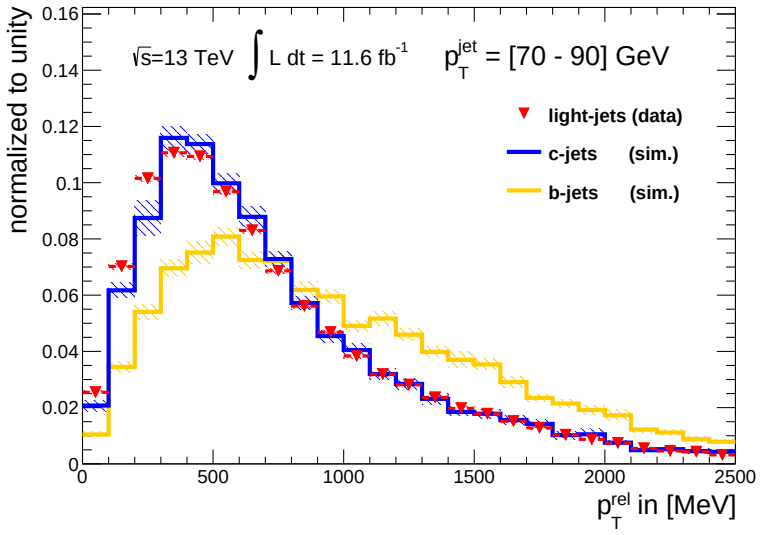

Figure 7.4.: Comparison of $p_{\mathrm{T}}^{\mathrm{rel}}$-templates for the different flavor hypotheses. The templates for light- and c-jets are shown in red and blue, respectively. They clearly differ from the b-template shown in yellow.

There are possible $p_{\mathrm{T}}^{\mathrm{jet}}$-dependences for the template shapes, the flavor fractions as well as the tagging efficiencies, themselves. That is why the measurement is done in regions of $p_{\mathrm{T}}^{\mathrm{jet}}$. Figure 7.5a shows the $p_{\mathrm{T}}^{\mathrm{jet}}$-dependence of the b-template. The η-dependence of the **s**cale **f**actors (SFs) has been found to be negligible in *Run 1* measurements which also has been confirmed for *Run 2* (see Appendix A.1). Also, due to the low correlation of $p_{\mathrm{T}}^{\mathrm{rel}}$ with the tagging algorithms discussed before, there is no dependence of the template shape on the applied tagger and OP as shown in Figure 7.5b. Hence, the templates can be generated before applying any tagging decision to maximize the statistical precision and can then be applied to the tagged data distributions.

Figure 7.6 visualizes how the $p_{\mathrm{T}}^{\mathrm{rel}}$-method works. The four plots show the different inputs to the SF determination. The black dots represent the $p_{\mathrm{T}}^{\mathrm{rel}}$-distribution measured in data. On the left, only jets tagged by the algorithm and OP are shown, while on the right, only untagged jets are used. All plots also show the stacked templates for b, c, and light in yellow, blue, and red, respectively. The top plots combine the templates using the flavor fractions determined on the unfiltered MC which is used to calculate the simulation efficiency. Below, the same templates are used, combined with the b-fraction obtained by the likelihood fit.

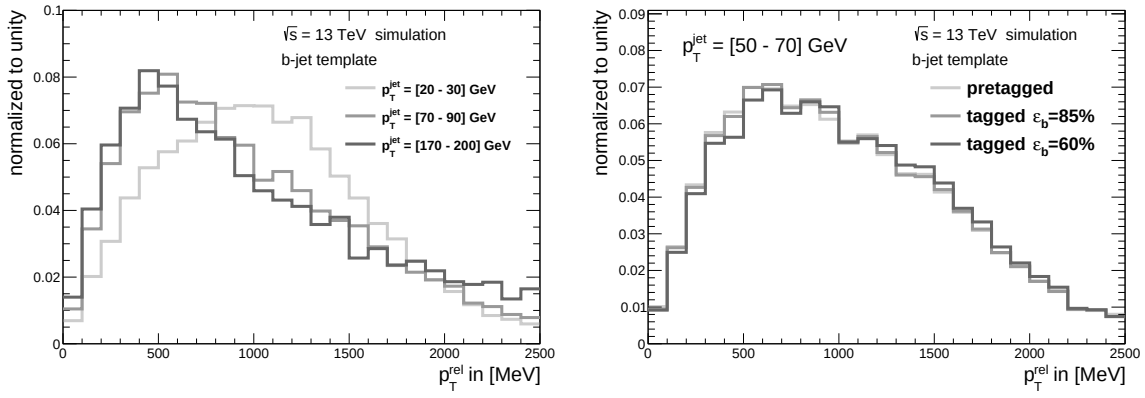

(a) Shape dependence on jet momentum.

(b) Shape dependence on tagging decision.

Figure 7.5.: Templates for b-jets in different $p_{\mathrm{T}}^{\mathrm{jet}}$-regions shown in different shades of gray (left) show a clear momentum dependence. The b-templates show no dependence on the tagging decision (right).

As expected, the flavor fractions differ by some amount. The goodness of fit can be assessed using a χ^2-criterion. While it is possible that the χ^2/ndf is better for the MC prediction, because the fit is optimizing the discussed likelihood function and not the χ^2, the agreement needs to be better after the fit in most of the cases. This is true for the discussed results and is shown exemplary for one OP in Appendix A.2.

It is noticeable that the log-likelihood fit can converge to an all b-jet composition as shown in Figure 7.6c. This can be caused by the minimization algorithm hitting the parameter boundaries or simply by the data being described best by a pure b-template result. Both cases can occur in datasets with a very high b-purity ($\gtrsim 99\%$). While it is not expected to have no light- or c-jets in the set of candidates the template fit is not sensitive to a low amount of jets. The resulting impact on the measured b-tagging efficiency is small and covered by the template statistics uncertainty discussed in Chapter 9.

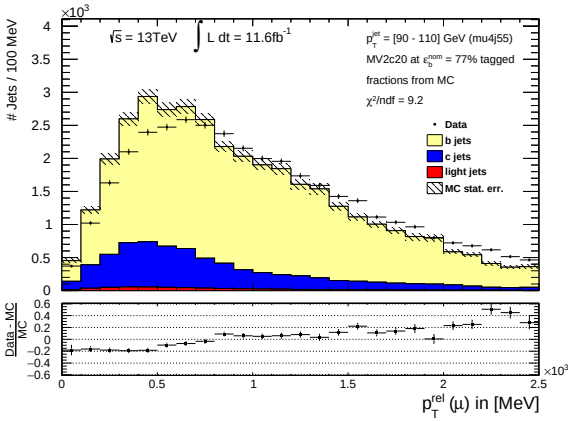

(a) MC prediction for the tagged distribution.

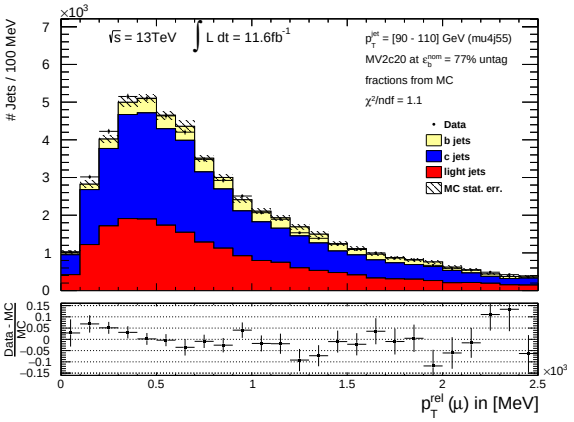

(b) MC prediction for the untagged distribution.

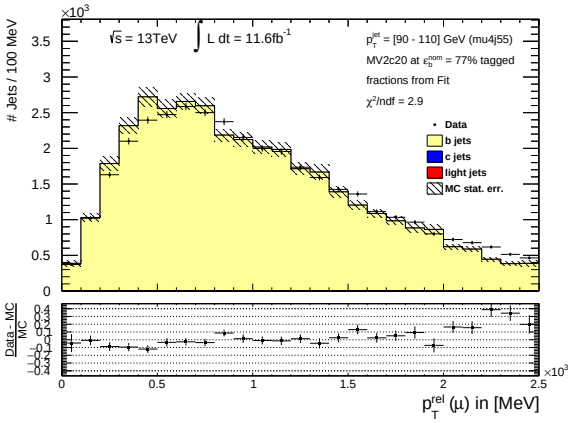

(c) Fractions obtained from fit to the tagged distribution.

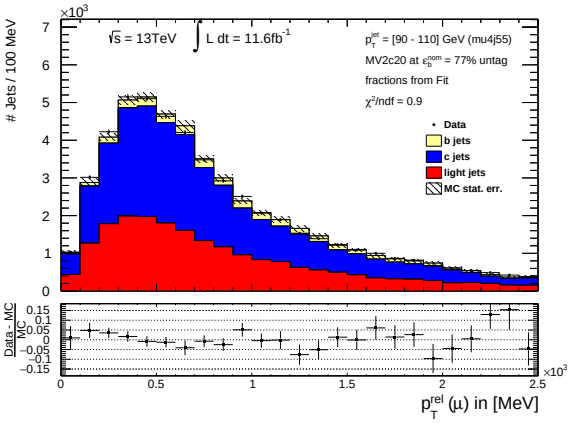

(d) Fractions obtained from fit to the untagged distribution.

Figure 7.6.: Distributions of $p_{\mathrm{T}}^{\mathrm{rel}}$ using b-tagged jets (left) and untagged jets (right). The black dots show the data while the templates are shown as a colored stack. The distributions on top use the flavor-fractions as predicted by the unfiltered MC while the plots below show the results of the fit.

8. Scale Factor Determination

Nicht darf ich dir zu gleichen mich vermessen.

FAUST

Performing the log-likelihood fit to the $p_{\mathrm{T}}^{\mathrm{rel}}$-distribution for the sets of tagged and untagged $p_{\mathrm{T}}^{\mathrm{rel}}$-candidates results in the respective flavor-fractions f_b as described in Chapter 7. These are then used to calculate the b-tagging efficiency and derive **s**cale **f**actors (SFs) in the following way.

8.1. Efficiencies and Scale Factors

As discussed in Chapter 5, the b-tagging efficiency ε_b is defined as the fraction of tagged b-jets divided by the total number of b-jets (see equation (5.1)). Using the flavor-fraction f_b in the tagged and untagged set, the efficiency can be found as

$$\varepsilon_b^{\mathrm{data}} = \frac{f_b^{\mathrm{tagged}} \cdot N_{\mathrm{data}}^{\mathrm{tagged}}}{f_b^{\mathrm{tagged}} \cdot N_{\mathrm{data}}^{\mathrm{tagged}} + f_b^{\mathrm{untagged}} \cdot N_{\mathrm{data}}^{\mathrm{untagged}}}, \tag{8.1}$$

with the total number of jets observed in the tagged and untagged data distributions N_{data}. Here, the statistical correlation in the nominator and denominator becomes obvious. Using the truth-flavor in **M**onte **C**arlo (MC) makes it possible to also calculate the efficiency in simulation $\varepsilon_b^{\mathrm{sim}}$ for the respective phase-space region. Comparing the efficiencies from simulation and measurement, SFs $\kappa^{data/sim}$ are defined as

$$\kappa_b^{data/sim} = \varepsilon_b^{\mathrm{data}} / \varepsilon_b^{\mathrm{sim}}. \tag{8.2}$$

The SFs are then used to correct the b-tagging efficiency when using the algorithm in an analysis. An example of the measurement of the b-tagging efficiency and the resulting SFs are shown in Figure 8.1.

Figure 8.1a displays the measured efficiency in dependence of $p_{\mathrm{T}}^{\mathrm{jet}}$ as black dots. While the statistical uncertainty is very small and barely visible in those figures, the systematic uncertainty is clearly visible in the green uncertainty bands. An overview of the different sources of uncertainty is given in Chapter 9. The measured efficiency

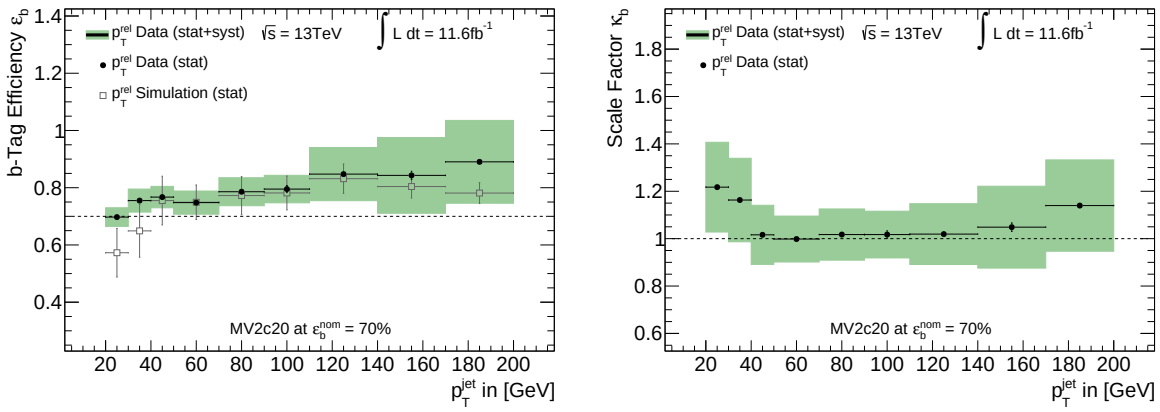

(a) Efficiencies.

(b) Scale factors.

Figure 8.1.: Showing the measured efficiency (left) in the black dots with systematic uncertainties in green bands while the simulation efficiency is shown in gray. The calculated SFs (right) are shown as black dots with statistical and systematic errors in green. The studied algorithm is the MV2c20 with a nominal efficiency of 70% depicted by the dashed line.

is then compared to the MC prediction shown in the gray circles with the respective statistical uncertainty as obtained from the simulation.

For both data and simulation, a clear difference to the nominal efficiency value shown as a dotted line is visible. This is due to the fact that the nominal efficiency is determined on a specific $t\bar{t}$-simulation as a benchmark. Therefore, similar but not identical efficiencies are expected. Also a dependence on the $p_{\mathrm{T}}^{\mathrm{jet}}$ is visible, showing that low energy b-jets are harder to identify due to their kinematic properties. This can be understood by a boosted b-hadron traveling a larger distance in the detector before decaying, resulting in higher **i**mpact **p**arameters (IPs) and clearly separable **s**econdary **v**ertices (SVs) making them easier to identify. It is also clear that the efficiencies obtained by the measurement and the MC prediction do not agree perfectly which leads to the resulting SFs.

The SFs shown in Figure 8.1b are an example of the results obtained for one tagging algorithm and **o**perating **p**oint (OP). Here, the results are again shown as black dots. The green uncertainty bands include the systematic uncertainty as well as the MC and data statistical uncertainties. While being close to unity, a $p_{\mathrm{T}}^{\mathrm{jet}}$ dependent deviation can be observed. This is caused by a $p_{\mathrm{T}}^{\mathrm{jet}}$ dependent difference in the modeling of

flavor dependent kinematic variables in the simulation. The rise in the low $p_{\mathrm{T}}^{\mathrm{jet}}$ region was additionally checked against a kinematic bias. In the $20\,\mathrm{GeV} < p_{\mathrm{T}}^{\mathrm{jet}} < 30\,\mathrm{GeV}$ and $30\,\mathrm{GeV} < p_{\mathrm{T}}^{\mathrm{jet}} < 40\,\mathrm{GeV}$ regions the trigger with the lowest threshold available (i.e. $p_{\mathrm{T}}^{\mathrm{jet}} > 15\,\mathrm{GeV}$ and $p_{\mathrm{T}}^{\mu} > 4\,\mathrm{GeV}$) is chosen which might not be fully efficient in those kinematic regions. Therefore, multiple approaches have been used to assess a possible bias but no systematic effect was observed leading to the conclusion that the observed behavior is inherent to the tagging algorithm on the respective simulation and kinematic phase space and not a trigger induced effect[20].

8.2. Systematic Uncertainties

The systematic limitations of the $p_{\mathrm{T}}^{\mathrm{rel}}$-measurement are discussed in detail in Chapter 9. Table 8.1 shows the full list of evaluated uncertainties for the result of the presented measurement for the $\varepsilon_b^{\mathrm{nom}} = 70\%$ OP of the MV2c20 algorithm. The uncertainties are given in the respective bins of $p_{\mathrm{T}}^{\mathrm{jet}}$. In general the uncertainties are evaluated by applying systematic variations to the templates, performing the template fit and comparing the results obtained by the variation to the nominal result or between an "up" and a "down" variation. Here, the impact and possible mitigation of the dominating sources of uncertainty are discussed.

For high jet momentum bins the uncertainty of the light-to-charm ratio is the dominating systematic uncertainty. Especially in the highest $p_{\mathrm{T}}^{\mathrm{jet}}$-bin, the templates for all flavors become increasingly alike. Therefore, the discrimination power of the $p_{\mathrm{T}}^{\mathrm{rel}}$-method decreases and a variation of flavor fractions can have an increasing effect. This has also been observed in *Run 1* calibrations as discussed in [64] and [76] where the ℓc-ratio is the dominating uncertainty in the highest momentum region. This uncertainty represents the inherent limitation of the method itself and can not easily be reduced.

[20] The studies discussed here lead to the addition of a full trigger simulation in the early steps of the simulation planned to be produced for analysis efforts in 2017. This will allow for an even more in depth analysis not possible on reconstruction level information.

In the low $p_{\mathrm{T}}^{\mathrm{jet}}$-region, the presented SF results are limited by the available simulation statistics. Based on that, it becomes clear that an increase in the size of the available simulation sample and improvement in the quality of the modeling is an important factor in order to improve the precision of the *Run 2* calibration with the $p_{\mathrm{T}}^{\mathrm{rel}}$-method.

Another contributing uncertainty is the extrapolation to inclusive b-jets. This uncertainty accounts for a possible difference in the b-tagging efficiency of jets containing a muon compared to the inclusive b-jets (discussed in Section 9.3). The efficiency calculated for jets with an associated muon was not found to differ significantly compared to the efficiency determined on the inclusive set of jets [77]. The efficiencies where determined with a precision of 4%, generating this uncertainty. With a higher amount of data and simulation available in *Run 2*, this uncertainty can be determined with higher precision and therefore reduce the systematic uncertainty which is currently expected to be overestimating the effect.

Based on the presented results, it is expected that the $p_{\mathrm{T}}^{\mathrm{rel}}$-measurement can increase in precision for most of the kinematic range within the continuing *Run 2* data acquisition with the ATLAS detector and will continue to deliver reliable calibration measurements. The full list of uncertainty tables for all calibrated algorithms and OPs can be found in appendix A.4.

Table 8.1.: Systematic uncertainties for a set of $p_{\mathrm{T}}^{\mathrm{rel}}$-candidates passing the MV2c20 tagging algorithm at $\varepsilon_b^{\mathrm{nom}} = 70\%$ b-tagging efficiency.

MV2c20 at $\varepsilon_b^{\mathrm{nom}} = 70\%$	p_{T} in GeV								
Systematics [%]	20-30	30-40	40-50	50-70	70-90	90-110	110-140	140-170	170-200
Axis Smearing	0.3	0.6	0.7	0.5	2.0	2.0	6.5	7.0	0.3
B Fragmentation Fractions	0.1	-0.2	-0.4	-0.3	-0.1	-0.2	-0.2	0.2	<0.1
B Fragmentation Function	0.2	0.1	-0.1	-0.1	-0.2	-0.2	-0.2	-0.4	<0.1
B JES Response	<0.1	<0.1	0.1	0.3	0.1	-0.1	0.1	<0.1	<0.1
B-Decay p* Spectrum	-1.9	-1.5	-1.7	-1.9	-1.3	-0.6	-0.1	-0.2	<0.1
BDecayFractions	<0.1	<0.1	0.2	0.6	0.6	0.6	0.5	0.4	<0.1
Effective NP 1	0.7	0.5	1.0	0.7	-0.4	-0.4	0.6	-0.2	0.1
Effective NP 2	-0.1	<0.1	<0.1	<0.1	<0.1	-0.1	0.7	-0.8	<0.1
Effective NP 3	<0.1	<0.1	-0.1	<0.1	0.2	0.2	-0.4	<0.1	<0.1
Effective NP 4	<0.1	<0.1	0.1	<0.1	-0.1	0.2	0.1	0.3	<0.1
Effective NP 5	-0.1	<0.1	<0.1	0.1	<0.1	0.1	<0.1	0.1	<0.1
Effective NP Rest Term	<0.1	<0.1	0.1	0.1	-0.1	0.1	<0.1	0.2	<0.1
Eta Intercalibration Modeling	0.1	0.2	0.5	0.3	-0.4	-0.7	0.6	-0.6	<0.1
Eta Intercalibration Total Stat	0.1	<0.1	0.3	0.1	-0.2	-0.1	<0.1	0.1	<0.1
Fake Muons	-0.1	0.2	<0.1	0.5	-0.4	1.9	0.2	-0.5	-0.2
Flavor Composition	0.7	0.4	0.8	0.6	-1.3	-1.1	0.7	-0.7	0.1
Flavor Response	-0.2	-0.1	-0.4	-0.1	0.6	0.4	-0.1	-0.3	<0.1
Gluon Splitting B	<0.1	<0.1	0.2	0.7	1.2	0.9	1.0	1.4	0.2
Gluon Splitting C	<0.1	0.1	0.1	0.3	0.9	0.7	1.7	1.7	0.1
JER Single NP	0.1	0.6	0.1	1.2	0.5	-0.6	-2.7	2.2	-0.1
JVT Efficiency	<0.1	-0.1	-0.6	-0.8	-0.5	0.3	-0.8	-1.0	-0.1
LC-Ratio	-0.7	-2.5	0.9	0.9	-3.1	<0.1	-6.3	-12.6	-15.3
Light template contamination	-0.6	-0.7	-0.6	-0.5	-0.7	-0.5	-0.9	-1.0	-1.6
Muon ID	<0.1	<0.1	<0.1	-0.1	0.1	0.1	-0.3	-0.1	<0.1
Muon MS	<0.1	<0.1	<0.1	<0.1	<0.1	<0.1	0.3	-0.1	<0.1
Muon Scale	<0.1	-0.1	<0.1	<0.1	-0.1	-0.1	-0.5	-0.1	<0.1
Pileup Offset Mu	<0.1	0.1	0.4	0.3	-0.2	-0.1	0.1	0.1	<0.1
Pileup Offset NPV	0.1	0.2	-0.1	0.3	-0.2	-0.1	0.1	0.1	<0.1
Pileup Pt Term	<0.1	<0.1	<0.1	<0.1	<0.1	<0.1	0.3	<0.1	<0.1
Pileup Rho Topology	0.2	0.1	0.5	0.2	-0.4	0.1	-0.1	0.7	0.1
SF to Inclusive	4.0	4.0	4.0	4.0	4.0	4.0	4.0	4.0	4.0
Template Statistics	-0.1	1.6	0.1	-1.9	-0.8	-2.4	2.5	2.8	-3.6
Simulation Statistics	14.8	14.2	11.3	8.1	8.6	7.6	6.2	5.0	4.7
Data Statistics	0.6	0.5	0.7	0.8	0.8	1.6	1.1	1.7	0.5
Total Systematics	15.6	15.2	12.3	9.7	10.6	9.6	12.6	16.4	17.0

9. Systematic Uncertainties

Es irrt der Mensch so lang er strebt.

DER HERR

In order to estimate the precision of the $p_{\mathrm{T}}^{\mathrm{rel}}$-measurement the systematic limitations have to be evaluated. Therefore, multiple sources of systematic uncertainties are taken into account. For technical reasons the list of systematics and their calculation varies between *Run 1* and *Run 2*. In *Run 2* efforts have been made to further unify the treatment of common systematics between different analyses within ATLAS which leads to different treatment in some of the cases. When no special discrimination between run periods for the respective methods is mentioned the procedure has stayed the same.

If not otherwise mentioned, the systematics is applied before producing the templates including the respective variation. The template fits are then done in the same manner as discussed in Chapter 7 and each systematic is evaluated independently as a difference of the altered fit result with respect to the nominal measurement. There are two kinds of variations. A single variation is taken as the difference to the nominal value

$$\Delta\varepsilon_b = \varepsilon_b^{\mathrm{var}} - \varepsilon_b^{\mathrm{nom}}. \tag{9.1}$$

And a double sided variation is evaluated by doing an up- and downwards variation and using half the difference as a systematic uncertainty:

$$\frac{\Delta\varepsilon_b}{2} = \frac{1}{2}(\varepsilon_b^{\mathrm{up}} - \varepsilon_b^{\mathrm{down}}). \tag{9.2}$$

The uncertainties are then propagated to the **s**cale **f**actors (SFs) and added in quadrature, assuming there are no correlations in between the systematics. One might expect some systematics to be correlated but using this strategy gives a conservative estimate not depending on the knowledge or modeling of correlations.

9.1. Modeling and Resolution Uncertainties

Fake Muons in b-Jets

The $p_{\mathrm{T}}^{\mathrm{rel}}$-measurement relies strongly on the quality of the muon candidate. Fake muons from a variety of sources can have a negative impact on the separation power of the method. Therefore, the selection of **c**om**b**ined (CB) muons passing the *tight* muon quality criterion is used to reduce the amount of fake muons as much as possible, as discussed in Section 6.3. Remaining fake muons still may have an impact on the measurement. Two main sources are considered here. Firstly, other particles can be misidentified as muons. Secondly, muons from decay-in-flight of long lived particles, that decay after the **I**nner **D**etector (ID) can be misidentified as CB muons. In the b- and c-templates the amount of fake muons is under-estimated due to the muon-filter applied during the generator step. To account for this bias in the simulation, the fraction of fake muons in the templates has been increased by a factor of two to estimate the impact on the efficiency measurement.

Light Template Contamination

The light template is generated in a data-driven approach as described in Section 7.1.2. This allows for b-jets to pass the selection criteria and contaminate the template. The fraction of b-jets in the light-jet enriched sample is estimated on simulation to be in the order of few percent. This contamination is varied to account for the limited knowledge of this fraction in the data distribution. The effect on the measurement is calculated by directly altering the flavor fractions used in Equation (8.1).

Light-to-Charm Ratio

As discussed in Section 7.1 the ratio used to combine the light- and c-templates is set to a fixed value extracted from the unfiltered **M**onte **C**arlo (MC). Since those templates are rather similar in shape this improves the convergence behavior for the minimization process. A caveat of this procedure is that the ℓc-ratio depends on the modeling in the simulation. To account for possible mis-modeling effects the light-flavor contribution is varied by a factor of 2 up and down, a new non-b-template is generated and the $p_{\mathrm{T}}^{\mathrm{rel}}$-fit is repeated for both variations. The variations in the SFs are taken as the systematic uncertainties.

Jet Energy Scale and Resolution

The reconstruction of jets, as discussed in Section 3.3 is highly non-trivial and multiple steps of reconstruction and calibration have to be performed. Complex non-linear dependencies and correlations make it complicated to disentangle the different sources and magnitudes of uncertainties. In *Run 1* fewer variations are done to cover the combined impact of multiple effects. For *Run 2* in situ measurements with high amounts of **n**uisance **p**arameters (NPs) are put in place. The most important variations are identified and a set of reduced NPs is applied to the analysis.

In *Run 1* the **j**et **e**nergy **r**esolution (JER) systematic covers the limited resolution of the jet energy reconstruction. The jet energy in simulation is smeared with a Gaussian function with the width set to the resolution of the jet energy, which is measured in dedicated studies as explained in [90]. The altered jets are then used to determine the efficiency and the difference to the nominal result is taken as the uncertainty. Similarly the **j**et **e**nergy **s**cale (JES) is evaluated by scaling the jet p_{T} within $\pm 1\sigma$ of the measured uncertainty. The *Run 1* procedure to determine the JES uncertainty is explained in [91].

For *Run 2* the jet related systematics are evaluated in the form of multiple NPs as discussed above. A breakdown of the different components is given in [92]. The recommendations used for the $p_{\mathrm{T}}^{\mathrm{rel}}$-measurement in *Run 2* are briefly summarized as follows:

- JER single NP: The quadratic sum of ten uncorrelated NPs to cover uncertainties on the JER.
- BJES response: Variation of the response function $R_b = \langle E_{\mathrm{reco}}/E_{\mathrm{truth}} \rangle$ for b-jets. With E_{reco} being the reconstructed jet energy and E_{truth} being the energy on MC level.
- Effective NPs: A total of 64 NPs are evaluated in an in situ measurement to cover multiple sources of uncertainties. These parameters are reduced to five main contributions and one additional estimator for residual effects.
- Eta Inter-calibration: During the η-inter-calibration jets with a high pseudo-rapidity are calibrated using central jets as a reference. The systematic and statistical limitations of this method are propagated to the analysis to estimate corresponding uncertainties.

- Flavor Response and Composition: The properties of a jet depend on the contributions of quarks and gluons during the hadronization. These properties can have an impact on the calorimeter response. The "Flavor Response" uncertainty covers differences of the response function for gluon and quark induced jets. The "Flavor Composition" uncertainty accounts for the impact of the modeling of gluon to quark ratios in the hadronization process.

Muon p_{T} Spectrum

The measurement of the muon momentum is also prone to uncertainties. In *Run 1* the muon p_{T} spectrum is reweighted to match the distribution observed in data. This reweighted distribution is used for the nominal measurement while the difference to the unchanged distribution is taken as a systematic.

In *Run 2* a dedicated study is performed to treat the muon related uncertainties in a common approach within different analyses. Therefore, multiple systematic effects have been studied, of which only the following have an impact to the $p_{\mathrm{T}}^{\mathrm{rel}}$-calibration[21]. Systematic variations are evaluated by smearing the respective observable with a Gaussian function with the width set to the respective resolution:

- The muon scale systematic accounts for the resolution of the muon momentum by altering the p_{T}^{μ} within $\pm 1\sigma$ of its uncertainty.

- For the muon ID uncertainty the muon track as reconstructed by the ID is smeared by $\pm 1\sigma$ of the precision achieved by its measurement.

- The same $\pm 1\sigma$ variation is applied to the **M**uon **S**pectrometer (MS) track resulting in the muon MS systematic.

Semileptonic correction

As a part of the jet energy response measurement for heavy flavor jets, the semileptonic correction as discussed in Section 6.5 accounts for the energy fraction emitted in form of the muon and neutrino. While the impact of the uncertainty in the difference of the jet direction to the b-hadron is already covered by the respective direction modeling uncertainty the impact of the jet momentum scaling has to be evaluated separately.

[21] Other systematics only affect e.g. isolated or high p_{T} muons and are therefore negligible for this measurement.

In *Run 1* a dedicated all particle response function is utilized to scale the $p_{\mathrm{T}}^{\mathrm{jet}}$. This is then varied within the predetermined uncertainties [91].

Modeling of b- and c-Production

The strong interaction preserves the flavor quantum numbers. Therefore, gluons produce pairs of b- or c-quarks. Depending on the kinematic properties of the initial gluon these quark pairs can form independent hadrons while still flying into the same direction and hence being clustered into a single jet. For two hadrons of the same flavor the tagging probability is not expected to be the same as for a jet with only one heavy flavor hadron. Particularly, a jet with two b-hadrons has a higher probability of being tagged as a single hadron jet. Therefore, the overall tagging rate depends on the fraction of jets with two heavy flavor hadrons insight. The fraction of jets with multiple heavy flavor hadrons coming from gluon splitting might differ between data and simulation. To evaluate the impact of this effect the amount of these jets in the simulation is varied by a factor of 0 or 2 as a down- or upwards variation, respectively. Figure 9.1 shows the difference of the varied b-template compared to the nominal in black and red. For higher $p_{\mathrm{T}}^{\mathrm{jet}}$-regions the amount of gluon splitting is expected to increase due to the additional Lorentz-boost which can also be observed by comparing figures 9.1a and 9.1b.

b-Decay

The $p_{\mathrm{T}}^{\mathrm{rel}}$-method is sensitive to the decay chain of heavy-flavor particles. This is due to the multiple decay steps in which muons can be produced, meaning a muon in the final state not necessarily originates from the b-decay but can also originate from decays of intermediate particles in decay cascades. The ratio of direct decays to cascade decays is modeled in the MC simulation to agree with current measurements. This fraction is varied within the uncertainties of the respective measurements to evaluate a systematic uncertainty.

For the variation the following values have been used[22]: The **b**ranching **r**atio (BR) for direct decays is measured to $BR(b \to lX) = (10.69 \pm 0.22)\%$ and for cascade decays to $BR(b \to c \to lX) = (9.62 \pm 0.53)\%$ [64, 93].

[22]Current results do not differ significantly with respect to the values used in *Run 1* [11].

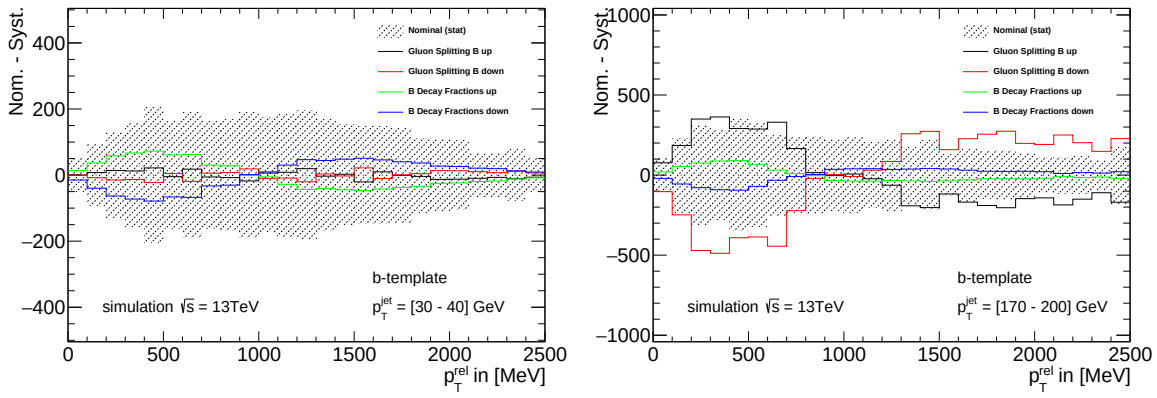

(a) Low $p_{\mathrm{T}}^{\mathrm{jet}}$ region.

(b) High $p_{\mathrm{T}}^{\mathrm{jet}}$ region.

Figure 9.1.: Differences between nominal and systematic b-templates for two bins of $p_{\mathrm{T}}^{\mathrm{jet}}$. The statistical uncertainty on the nominal template is depicted by the shaded band while the gluon splitting and b-decay uncertainties are shown in color coded lines. It can be observed that the systematic variations change the template shape which can have different dependences on the $p_{\mathrm{T}}^{\mathrm{jet}}$.

Therefore, the ratio is found to be

$$\frac{BR(b \to lX)}{BR(b \to c \to lX)} = 1.11 \pm 0.07. \tag{9.3}$$

To evaluate the impact of the uncertainty on the template shape, jets are weighted based on the origin of the associated muon as can be seen in Figure 9.1. For this systematic no strong $p_{\mathrm{T}}^{\mathrm{jet}}$-dependence is observed, due to the fact that the BRs are independent from the jet momentum.

In addition to the variation of the ratio of direct to cascade decays, the muon momentum in the b-hadron rest-frame p^* is varied. Therefore, a pre-determined weighting function is applied to muons from direct b-decays. To evaluate the agreement with current measurements events are generated using Pythia and EvtGen (w/o detector simulation) and the resulting p^* distribution is found to agree with the measurement performed by the DELPHI-collaboration [94] within uncertainties as shown in Figure 9.2a. An independent measurement performed by the BaBar-collaboration [95] is then used to calculate weights utilized to estimate the systematic uncertainty[23].

[23]The measurements include or exclusively use electrons. Due to their low mass the p^*-distribution

b-Quark Fragmentation

In addition to the b-decay systematics, accounting for uncertainties in the branching fractions and the muon momentum p^*, the fragmentation systematics are related to the production of the b-hadron itself. First, the b-fragmentation function X_b describes the amount of energy from the initial b-quark that is transferred to the hadron. This function is altered so that the average energy fraction passed to the b-hadron is varied by 5% as an up-down-systematic.

Second, the production fractions of b-hadrons are varied as shown in Figure 9.2b. For *Run 1* production fractions are used as measured at **L**arge **E**lectron **P**ositron Collider (LEP) [93]. The results agree at a $2\,\sigma$ level with measurements performed at Tevatron [97]. Therefore, the hadron spectrum is reweighted to match the results from the Tevatron measurement. The difference to the nominal measurement is taken as a systematic uncertainty. In *Run 2* the nominal value is replaced by the combination done by the **H**eavy **F**lavor **A**veraging **G**roup (HFAG) as discussed in Section 1.5.1 (see Table 1.3) [15] while the uncertainty is still computed using the results obtained by Tevatron [97].

Jet Vertex Fraction

As discussed in Section 3.3 the **J**et **V**ertex **F**raction (JVF) and **J**et **V**ertex **T**agger (JVT) are used to reduce pile-up dependencies in *Run 1* and *Run 2*, respectively. Since both techniques rely on information based on jets, tracks and vertices they might induce a bias on the favor-tagging efficiency. To evaluate the impact on the $p_{\mathrm{T}}^{\mathrm{rel}}$-measurement a systematic uncertainty is computed. In *Run 1* this uncertainty is determined by dropping the JVF requirement entirely from the analysis and redoing the calibration. The difference is then taken as an estimate for the uncertainty. In *Run 2* in situ measurements have been performed to study the quality of the JVT modeling [92]. While the respective effects have been found to be negligible the choice of the JVT-threshold might still affect the measurement. This has been estimated by switching from the default to a "loose" and "tight" cut value of the JVT-output. These are then propagated to the $p_{\mathrm{T}}^{\mathrm{rel}}$-calibration as an up- and downwards variation.

for electron and muon agree for the available region as can also be seen in [96]

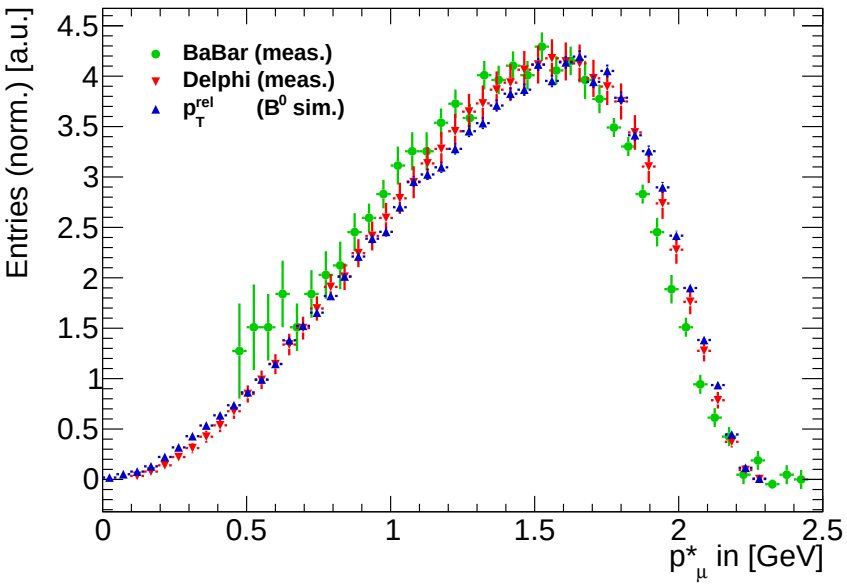

(a) B-decay p^* distributions.

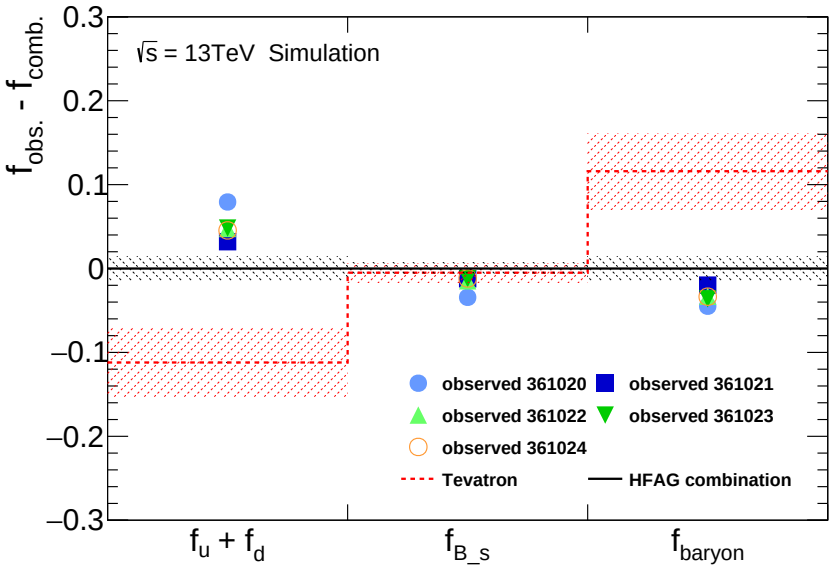

(b) Fragmentation Fractions.

Figure 9.2.: Comparison of the lepton p^*-spectrum for semileptonic B-decays (top). Measurements by DELPHI (red) [94] and BABAR (green) [95] are compared to simulation (blue). Difference in b-fragmentation fractions compared to the combination done by the HFAG [15] (bottom). The MC fractions are evaluated on the unfiltered jet slices separately as indicated by the run numbers in the legend. The difference to the Tevatron measurement [97] used for systematics is shown in red.

Pile-up

During generation of simulated samples additional interactions are simulated and superimposed to each event to account for pile-up in the data. The average number of interactions per bunch-crossing $\langle\mu\rangle$ is set to the expected pile-up profile for the respective data-taking period. Furthermore, the simulation of additional interactions is updated on a regular basis to adapt to the changing pile-up profile under different data-taking conditions. In addition a reweighting of the MC events to the measured $\langle\mu\rangle$ profile is carried out. In *Run 1* the reweighting factors were varied and the difference to the nominal fit was used to estimate a corresponding uncertainty.

For *Run 2* this systematic is split into four independent up-down-variations. This is done because of the switch from 50 ns to 25 ns bunch spacing which increases the out-of-time pile-up while the increase to 13 TeV center-of-mass energy also increases the p_{T} dependence of the pile-up corrections. The following variations are considered [92]:

- Offset μ: Accounting for the dependence on the average interactions per bunch-crossing. Additional interactions and the resulting radiation hamper the reconstruction of the process of interest.
- Offset N_{PV}: In contrast to the number of interactions the number of **p**rimary **v**ertices (PVs) requires good quality tracks to reconstruct the vertex. Therefore, the dependence for additional, well reconstructed vertices is different than for the pure number of interactions.
- p_{T} Term: The pile-up correction is highly p_{T} dependent because of the steep fall in the cross section for higher momentum transfers in the additional minimum bias events.
- ρ Topology: The jet momentum density ρ is defined as the median of the momentum times jet area for all jets in the event. The jet area is determined by ghost-associating pseudo-particles with infinitesimal momentum to the jet. This part describes the dependence on the overall jet activity in the event.

Modeling of the b-Hadron Direction

The muon $p_{\mathrm{T}}^{\mathrm{rel}}$ depends on the relative direction between the hadron and the muon produced during the decay. For the calibration measurement jets are used instead

of the hadrons four momentum. Since the jet direction typically does not coincide exactly with the direction of the b-hadron a difference in the modeling on MC-level may have a non-negligible effect on the resulting templates. This effect is limited by the jet direction resolution and is studied comparing calorimeter jets to jets formed from particle tracks. The variation is found to be $\Delta\eta(\text{calo}, \text{track}) = 0.008$ and $\Delta\phi(\text{calo}, \text{track}) = 0.004$ [64]. While being a small variation with respect to the jet direction it corresponds to a variation of $O(10\%)$ on the relative hadron direction within the jet. This has been validated by a two-dimensional Gaussian fit to the difference in the b-hadron to jet direction as shown in Figure 9.3. Each jet momentum vector is varied in η and ϕ with a Gaussian smearing within these estimates. The $p_{\text{T}}^{\text{rel}}$-value is then calculated using the altered jet direction and new templates are generated.

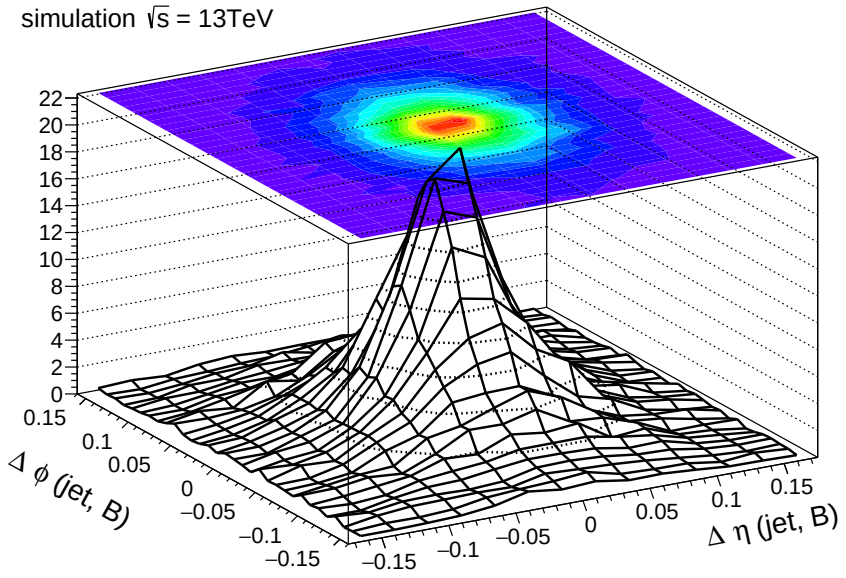

Figure 9.3.: Difference in the b-hadron direction compared to the jet direction in η and ϕ. The b-hadron direction is obtained from simulation "truth" information.

9.2. Simulation Statistics

Simulation Tagging Efficiency

The tagging efficiency in simulation ε^{sim}, as used in Equation (8.2), has a statistical uncertainty. This is calculated from the statistical uncertainties of the number of tagged and untagged b-jets in the simulated samples and propagated according to the definition in Equation (5.1), taking into account the correlation of the events in the nominator and denominator.

Template Statistics

The template fit relies on the prediction of the number of expected events in each $p_{\text{T}}^{\text{rel}}$-bin for the respective flavor-hypothesis. This is limited by the MC statistics or the number of events available for the light-template. To estimate the impact of the limited statistics on the template shape the template shape is varied in ten thousand pseudo-experiments. Therefore, templates are generated by generating Gaussian pseudo-data with the expectation value of the bin value. The Gaussian width is set to the statistical error of the respective bin. The template fit is done for all pseudo-templates and the mean value and the standard deviation are calculated for all results. The systematic uncertainty is taken as the standard deviation or the difference of the mean value to the nominal measurement, in cases where the measurement is not within 1σ.

9.3. Extrapolation Uncertainty

Scale Factor for inclusive b-Jets

As discussed in Section 1.5.2 only a tenth of b-hadrons decay into final states containing a muon. Therefore, despite the fact that the soft muon tagger as discussed in Section 5.1 is not used for high-level tagging algorithms, there might be a difference in the tagging efficiency for jets with or without a muon. Additionally, for the calculation of SFs the resulting efficiency is compared to the MC expectation and therefore phase-space related dependencies are expected to cancel out. This is limited by the modeling of the phase-space and the respective tagging efficiencies. In order to

estimate this effect a dedicated measurement has been performed, determining data-to-simulation SFs in a sample of $t\bar{t}$-events [77]. This measurement has been performed for jets with and without a muon in the jet under study and has been repeated for multiple tagging algorithms and **o**perating **p**oints (OPs). The measurements in the two regions agree within the achieved 4% uncertainties. Since no significant deviation was observed a conservative approach was chosen and the 4% uncertainty were assigned for the extrapolation from the $p_{\mathrm{T}}^{\mathrm{rel}}$-phase-space to the inclusive b-jets region.

9.4. Dependence on Run Conditions

During time some experimental conditions may change. There is a huge variety of factors that can vary during time. Besides unintended variations like unscheduled downtime of detector components or unexpected software behavior which occurs for some time period there are also intentional differences between run periods mostly due to modifications in the beam setup e.g. to increase the instantaneous luminosity. In order to adapt to the rising collision rates the trigger setup then also adapts during time. Furthermore, software running on some of the detector components get updated repeatedly to improve the system performance. These are just some examples of parameters that change during time. To investigate the impact of these variations the dataset under study has been split in disjoint data taking periods and the calibration has been performed for all of them individually.

Figure 9.4a shows the results of the efficiency measurement for different data taking periods. In order to evaluate the agreement within all periods a χ^2-test is performed. Since all data periods are statistically independent the χ^2 between two periods is calculated for all possible combinations. This is repeated in all jet momentum intervals which are also statistically independent. The $\log_{10}(\chi^2(\varepsilon_b^{\mathrm{data}}))$ for each jet-p_{T} bin and every permutation of data periods is then compared to a χ^2-distribution with one degree of freedom as shown in Figure 9.4b.

This procedure has been repeated for all tagger and OP combinations separately since they are not statistically independent. It has been found that systematic variations between OPs is bigger than the deviation from the expected χ^2-distribution. Therefore, the results are in agreement with statistical variations between the data taking periods and no dependence on run conditions is observed.

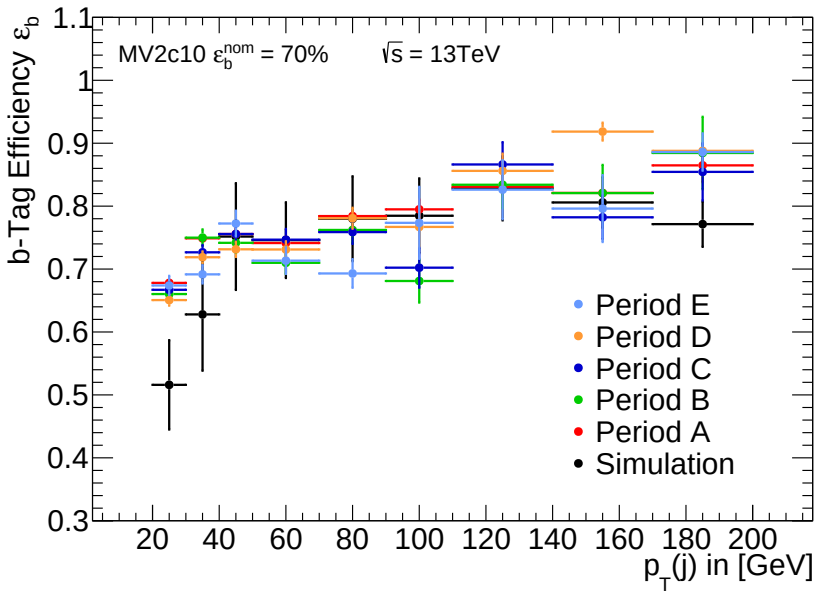

(a) Efficiencies.

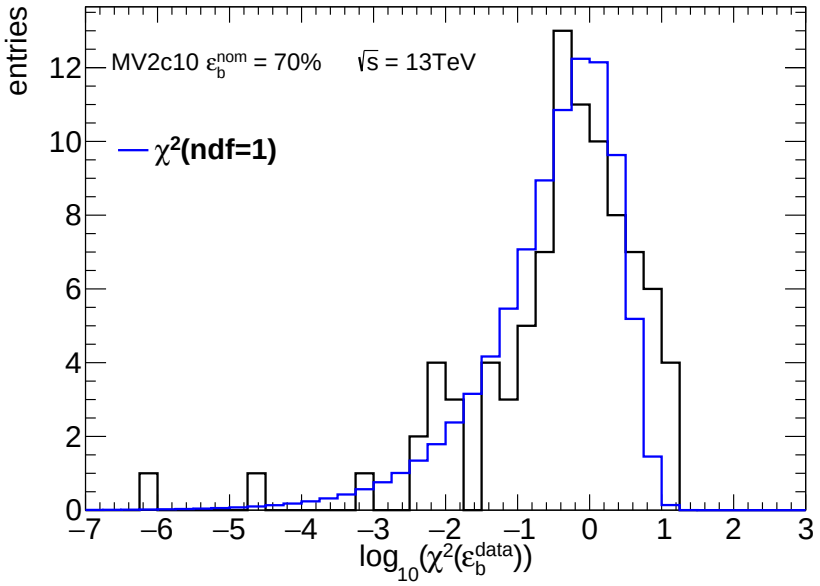

(b) Logarithmic χ^2 distribution.

Figure 9.4.: Comparison of efficiency measurements for different run periods at the top. For all permutations of pairs of data taking periods for each p_T^{jet}-bin a logarithmic χ^2 is calculated and shown at the bottom (black). It is compared to the expected distribution for one degree of freedom (blue).

10. Run 1 Trigger Calibration

Ich stand am Thor, ihr solltet Schlüssel seyn;
Zwar euer Bart ist kraus, doch hebt ihr nicht die Riegel.

FAUST

During data taking different trigger settings are used. This includes b-tagging triggers as described in Section 5.2. The $p_{\mathrm{T}}^{\mathrm{rel}}$-method has been used to also calibrate those triggers in *Run 1*. On trigger level different jet collections are available. Jets reconstructed based on **L**evel-**1** (L1) **f**ull **s**can (FS) or **R**egion **o**f **I**nterest (RoI) information can be utilized. Calibration measurements performed for the on-line SV1+IP3D algorithm in 2012 show no significant difference between those two options. Exemplary, the results for the FS version with the medium[24] **o**perating **p**oint (OP) are presented in the following sections. The jets reconstructed on trigger-level are not identical to the off-line reconstruction, which is usually used for the measurement. A cone based matching in the $\eta\phi$-plane is used to associate the jets of different reconstruction levels with each other before doing the measurement. Variables shown here are based on the objects reconstructed on the off-line level as described in Chapter 3.

10.1. Conditional Selection

The tagging algorithms deployed on the different levels of reconstruction are highly correlated. To take this correlation into account, the efficiency of the b-tagging trigger is measured depending on the off-line tagging decision. Therefore, two independent efficiency measurements are conducted for every OP. This ensures that the b-tagging trigger and an additional b-tagging algorithm can be utilized in parallel in a single analysis.

[24] The medium OP corresponds to a specific cut in the distribution of the tagging discriminant. This corresponds to a nominal b-tagging efficiency of 55%. Since the observed efficiency strongly depends on the conditional selection the OP is rather referred to as medium.

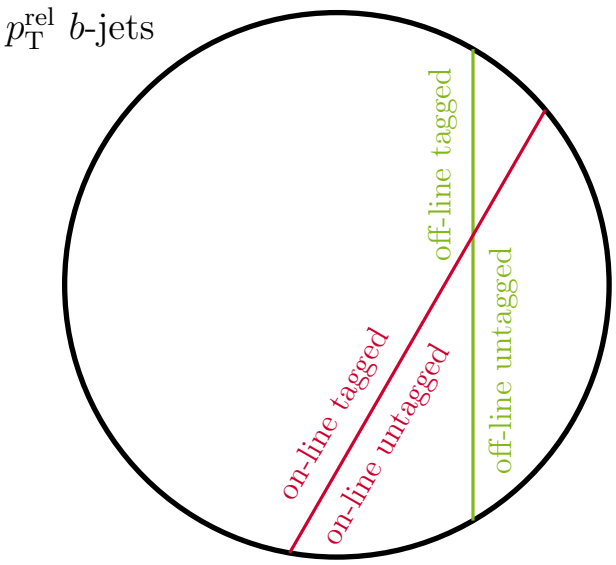

Figure 10.1.: Venn-like diagram showing all $p_{\mathrm{T}}^{\mathrm{rel}}$-candidates with a truth b-jet-match. The set is divided by applying an off-line b-tagging criterion (i.e. MV1) shown as the green line. Based on that an on-line tagging criterion, which is shown as the red line, is studied and the efficiency is measured on the left and right side independently. Due to high correlations the four generated sub-sets are very different in statistics.

This is achieved by first limiting the set of all $p_{\mathrm{T}}^{\mathrm{rel}}$-candidates to only the number of off-line jets that have a match to an on-line jet. Second, the remaining set of jets is divided by the off-line tagging algorithm MV1 as depicted as a green line in Figure 10.1. This results in an off-line tagged and an off-line untagged sub-set, shown left and right, respectively. In each of these sub-sets the b-tagging efficiency and the respective **s**cale **f**actors (SFs) are measured independently. Measuring this efficiency is done by dividing each sub-set again by applying the b-tagging criterion defined by the trigger algorithm which is depicted as the red line. Equation (8.1) can be altered with the following conditional notation:

- tag / $\overline{\text{tag}}$: passing / not passing the off-line tagging requirement,
- trig / $\overline{\text{trig}}$: passing / not passing the on-line trigger criterion,
- cond $\in \{\text{tag}, \overline{\text{tag}}\}$: the two possible off-line conditions,

to the following expression for the b-tagging efficiency:

$$\varepsilon_b^{\text{data|cond}} = \frac{f_b^{\text{trig|cond}} \cdot N_{\text{data}}^{\text{trig|cond}}}{f_b^{\text{trig|cond}} \cdot N_{\text{data}}^{\text{trig|cond}} + f_b^{\overline{\text{trig}}|\text{cond}} \cdot N_{\text{data}}^{\overline{\text{trig}}|\text{cond}}}. \tag{10.1}$$

This corresponds to two independent efficiency measurements $\varepsilon_b^{\text{data|tag}}$ (left from the green line in Figure 10.1) and $\varepsilon_b^{\text{data}|\overline{\text{tag}}}$ (right of the green line in Figure 10.1). Due to the high correlation of the two tagging criteria under study the different sub-sets are not of equal size. This results in very different statistical precision for the two sub-sets. This is partly accounted for by using a different binning in $p_{\text{T}}^{\text{jet}}$.

10.2. Template Fit

Due to the conditional approach described above, the amount of $p_{\text{T}}^{\text{rel}}$-fits doubles while the fit procedure remains the same as discussed in Chapter 7. As an example for the different combinations, a fit for each condition (trig|$\overline{\text{tag}}$, $\overline{\text{trig}}|\overline{\text{tag}}$, trig|tag, $\overline{\text{trig}}$|tag) is shown in Figure 10.2. Here, the on-line medium OP based on the decision of off-line MV1 with 70% nominal b-tagging efficiency is depicted. All distributions show the highest momentum bins which extend down to different regions (75 GeV or 110 GeV) based on the off-line tagger decision. It is clear that the usage of the off-line tagging algorithm leads to very different flavor compositions in the different sub-sets of jets the fit is performed on. The $p_{\text{T}}^{\text{rel}}$-measurement gives a reliable result for all the different regions, since it is not correlated with the tagging algorithms under study.

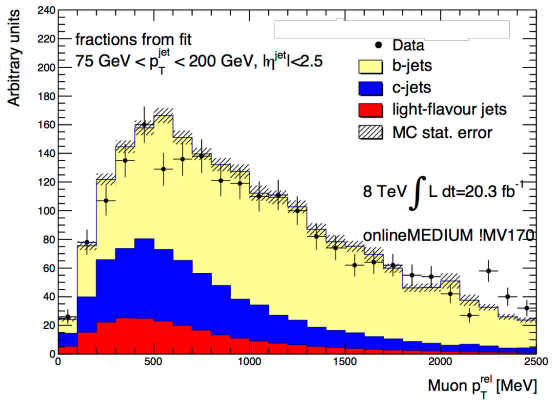

(a) Fit to the trig|$\overline{\text{tag}}$-distribution.

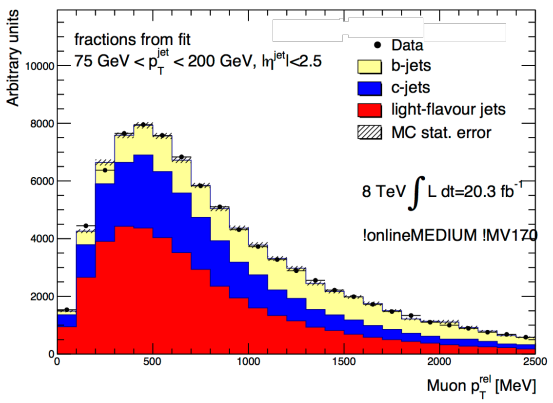

(b) Fit to the $\overline{\text{trig}}$|$\overline{\text{tag}}$-distribution.

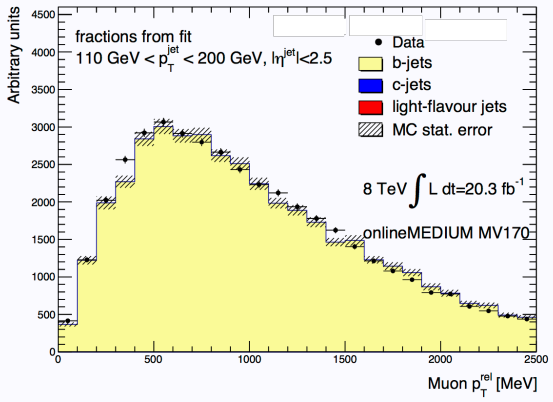

(c) Fit to the trig|tag-distribution.

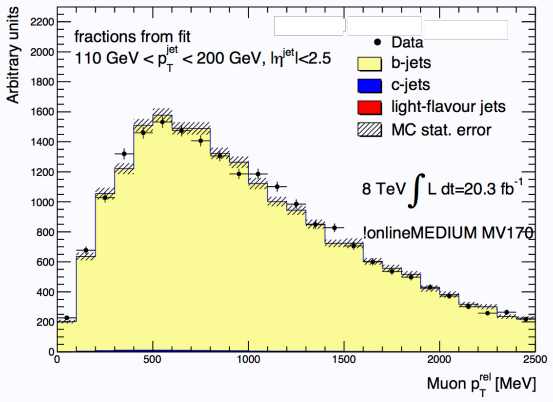

(d) Fit to the $\overline{\text{trig}}$|tag-distribution.

Figure 10.2.: Fits to the $p_{\mathrm{T}}^{\mathrm{rel}}$-distribution for the sub-set of jets rejected by the off-line tagger on top, and for the sub-set passing the off-line tagger criterion below. The fit to the sub-set tagged by the trigger-algorithm under study is depicted on the left and the rejected sub-set is shown on the right.

10.3. Efficiency and Scale Factors

The calibration measurement for the on-line algorithms and OPs is performed on a set of $p_{\mathrm{T}}^{\mathrm{rel}}$-candidates passing the off-line tagging criterion (left from the green line in Figure 10.1) or rejected by the off-line tagger (right of the green line in Figure 10.1). In Figure 10.3 exemplary results are presented for the on-line medium OP tagged by the off-line MV1 algorithm with 70% nominal b-tagging efficiency. Figure 10.3a shows the b-tagging efficiency for data and simulation in black and gray, respectively. It is noticeable that the simulation does reproduce the $p_{\mathrm{T}}^{\mathrm{jet}}$-dependence very well while overestimating the tagging efficiency in the full momentum range. This leads to the resulting SFs for the on-line medium OP in the off-line tagged case shown in Figure 10.3b. The observed SFs deviate from unity due to the overestimated efficiency in the simulation. The SFs slightly rise with increasing $p_{\mathrm{T}}^{\mathrm{jet}}$, which can be caused by the modeling of either the on-line or off-line kinematics. Therefore, the correct combination of on-line and off-line SFs has to be applied when utilizing both tagging algorithms in analyses.

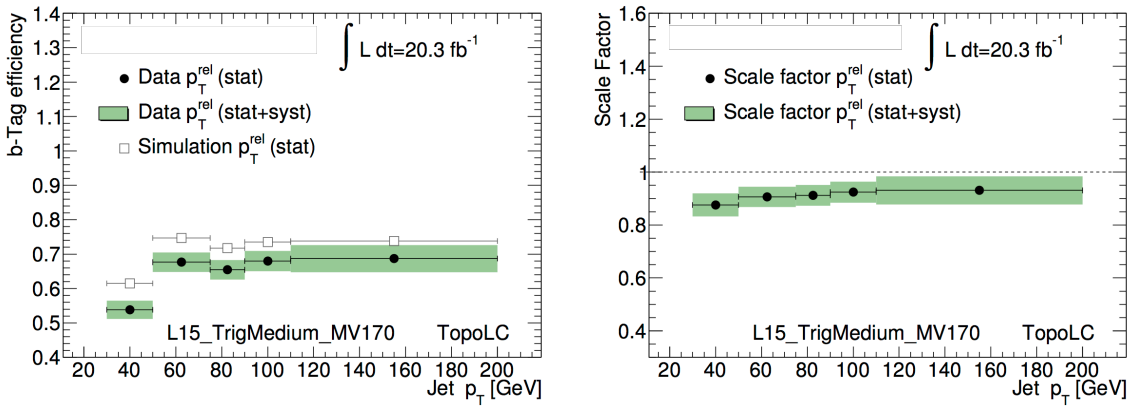

(a) Efficiency.

(b) Scale factors.

Figure 10.3.: Results for the on-line medium tagger based on a set of $p_{\mathrm{T}}^{\mathrm{rel}}$-candidates tagged by the off-line MV1 algorithm at an efficiency of 70%. Showing the measured efficiency (left) in black dots with systematic uncertainties in green bands. The simulation efficiency is shown in gray boxes. The calculated SFs (right) are shown as black dots with statistical and systematic errors in green.

10.4. Systematic Uncertainties

The systematic uncertainties presented in the following section correspond to the set of uncertainties used in the *Run 1* analysis[25]. These are discussed in Chapter 9 and are also the uncertainties used for the measurements presented in [64] and [76]. Table 10.1 lists the systematic and statistic uncertainties for the calibration measurement of the on-line trigger algorithm for the medium OP on the set of $p_{\mathrm{T}}^{\mathrm{rel}}$-candidates passing the off-line tagger MV1 with a nominal efficiency of 70%. Table 10.2 shows the same table of systematic and statistical uncertainties for the same on-line tagger and OP, but for the set of $p_{\mathrm{T}}^{\mathrm{rel}}$-candidates rejected by the off-line tagger.

The resulting uncertainties for the on-line calibration can differ rather strongly from the off-line systematics. This is due to the change in the flavor composition caused by the off-line tagger decision. For example is the light- and c-fraction in the set of $p_{\mathrm{T}}^{\mathrm{rel}}$-candidates tagged by the off-line algorithm significantly reduced, making it less prone to variations of the ℓc-ratio. In addition, a large set of **M**onte **C**arlo (MC) simulation was available at the end of *Run 1* reducing the respective uncertainty. This leads to the extrapolation to the inclusive b-jets (as explained in Section 9.3) being the limiting uncertainty for the calibration in the off-line tagged condition.

Due to the reduced amount of b-jets in the off-line untagged set and the high correlation between the tagging algorithms the measurement in this case is strongly limited by simulation statistics. This may also affect the estimation of some of the other uncertainties which could be prone to statistical fluctuations. This is mitigated by merging some of the high $p_{\mathrm{T}}^{\mathrm{jet}}$-bins. It was decided that no further optimization with respect to the uncertainties was necessary, since only a very small fraction of jets is scaled with the resulting SFs[26].

[25] The *Run 1* procedure does not preserve the sign of the uncertainty but only quotes the absolute value.

[26] The MV1 algorithm at an efficiency of 70% rejects $\sim$ 30% of b-jets. The on-line tagger at the medium OP only identifies less than 10% of those remaining b-jets due to the high correlation of the respective algorithms.

Table 10.1.: Systematic uncertainties for the FS trigger algorithm for the medium OP on a set of $p_{\mathrm{T}}^{\mathrm{rel}}$-candidates passing the MV1 tagging algorithm at 70% off-line b-tagging efficiency.

Trigger Medium | MV1 at 70%	p_{T} in GeV				
Systematics [%]	30-50	50-75	75-90	90-110	110-200
MC statistics	1.2	0.9	0.7	0.5	0.6
b-decay branching fractions	0.1	<0.1	<0.1	0.1	0.4
b-decay p* spectrum	<0.1	<0.1	0.2	0.2	1.8
b-fragmentation fraction	0.2	<0.1	0.2	0.4	0.1
b-fragmentation function	0.2	<0.1	0.2	0.2	0.7
charm-light ratio	0.2	0.1	<0.1	0.1	0.1
fake muons in b-jets	<0.1	<0.1	<0.1	<0.1	0.9
jet energy resolution	1.0	0.1	<0.1	0.2	0.2
jet energy scale	0.1	0.1	0.1	0.1	0.1
jet vertex fraction	0.3	<0.1	<0.1	<0.1	<0.1
modelling of b-production	<0.1	<0.1	<0.1	0.1	1.2
modelling of c-production	0.1	<0.1	0.2	0.5	0.7
modelling of the b-hadron direction	0.1	0.2	0.3	0.4	0.1
muon pT spectrum	<0.1	<0.1	0.1	0.1	3.0
pileup mu reweighting	<0.1	0.1	0.1	0.2	0.3
scale factor for inclusive b-jets	4.0	4.0	4.0	4.0	4.0
semileptonic correction	0.1	<0.1	<0.1	0.2	<0.1
simulation tagging efficiency	2.2	0.8	0.9	0.8	0.5
data statistics	1.1	0.6	0.9	1.1	0.7
total systematics	4.8	4.2	4.2	4.2	5.7

Table 10.2.: Systematic uncertainties for the FS trigger algorithm for the medium OP on a set of $p_{\mathrm{T}}^{\mathrm{rel}}$-candidates rejected by the MV1 tagging algorithm at 70% off-line b-tagging efficiency.

Trigger Medium | not MV1 at 70%	p_{T} in GeV		
Systematics [%]	30-50	50-75	75-200
MC statistics	13.7	9.5	7.1
b-decay branching fractions	0.5	0.2	0.3
b-decay p* spectrum	0.2	1.2	7.8
b-fragmentation fraction	1.0	1.3	2.1
b-fragmentation function	1.3	2.4	1.6
charm-light ratio	0.9	2.0	7.5
fake muons in b-jets	<0.1	0.3	0.2
jet energy resolution	14.7	6.3	6.4
jet energy scale	0.5	2.1	2.6
jet vertex fraction	0.9	<0.1	<0.1
modelling of b-production	0.6	2.2	2.8
modelling of c-production	2.1	1.2	9.1
modelling of the b-hadron direction	7.7	5.2	3.4
muon pT spectrum	1.1	0.7	7.4
pileup mu reweighting	2.7	2.3	0.9
scale factor for inclusive b-jets	4.0	4.0	4.0
semileptonic correction	0.4	1.7	1.0
simulation tagging efficiency	82.1	28.6	17.3
data statistics	9.2	5.3	6.7
total systematics	85.1	32.0	26.3

11. Summary and Conclusion

Da steh' ich nun, ich armer Thor!
Und bin so klug als wie zuvor;

FAUST

11.1. Summary

In this thesis, the first measurement of the b-tagging efficiency under *Run 2* conditions at a center of mass energy of $\sqrt{s} = 13\,\text{TeV}$ with the $p_{\text{T}}^{\text{rel}}$-method has been presented (as exemplary shown in Figure 11.1). For the new set of tagging algorithms, a reliable measurement has been achieved. The full list of systematic uncertainties used in *Run 1* has been adapted and extended to *Run 2* recommendations and has been evaluated for the presented measurement. It has been pointed out that an improvement of the precision of the measurement can be achieved. To attain such a progress, advances in the simulation with regard to trigger modeling as well as simulation statistics have to be made. This measurement currently represents the only b-tagging efficiency calibration not based on the $t\bar{t}$ final state within ATLAS. This provides a unique tool for analyses done in the same topology and phase-space as the $t\bar{t}$-based calibrations to assess the impact of b-tagging on their systematic uncertainty.

At this moment, an open comparison with other *Run 2* calibrations is not possible since other measurements are still in preparation for publication. The most commonly used calibration is the combinatorial likelihood approach (described in Section 5.3.1) due to the small uncertainties achieved by the high amount of $t\bar{t}$-pairs produced at the LHC in *Run 2*. Currently ongoing efforts concerning this method are internally documented in [98]. Comparing Figure 11.1 to results presented in that document show that the two measurements agree within their uncertainties except for the lowest $p_{\text{T}}^{\text{jet}}$-bin where the $t\bar{t}$-calibration gives a **s**cale **f**actor (SF) that is close to unity. In general, the combinatorial likelihood approach shows a slightly falling trend with $p_{\text{T}}^{\text{jet}}$, which is not observed by the $p_{\text{T}}^{\text{rel}}$-calibration.

A comparison between the $p_{\mathrm{T}}^{\mathrm{rel}}$-measurement for *Run 1* and *Run 2* shows that the SF for the MV2 algorithm has an upwards trend in the low $p_{\mathrm{T}}^{\mathrm{jet}}$ region in contrast to the SF measured for the MV1 algorithm in *Run 1*. However, there is no reason for the two algorithms to show the same $p_{\mathrm{T}}^{\mathrm{jet}}$-dependence. For the dominant systematic uncertainties, there are similarities to previous measurements. The limitation of the method in the high momentum region by the ℓc-ratio uncertainty is inherent to the method and not the algorithm under study. This behavior can be observed in the current results as discussed in Section 8.2 as well as in previous measurements [64, 76].

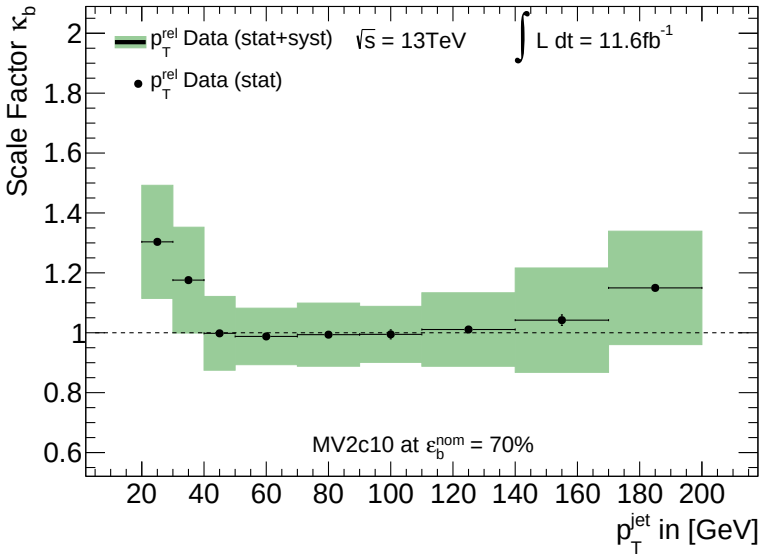

Figure 11.1.: Resulting SFs for the MV2c10 algorithm obtained by the $p_{\mathrm{T}}^{\mathrm{rel}}$-measurement at the nominal efficiency of 70%.

In addition to the first *Run 2* calibration, a measurement of the b-tagging efficiency of on-line tagging algorithms, implemented on trigger level, have been presented. Up to this point, the $p_{\mathrm{T}}^{\mathrm{rel}}$-method is the only available measurement of this kind within the ATLAS experiment. The conditional calibration discussed in Chapter 10 creates additional challenges especially for the available simulation statistics which limits the precision of the conducted measurement. Despite these challenging conditions a reliable measurement with the $p_{\mathrm{T}}^{\mathrm{rel}}$-method was achieved.

11.2. Outlook and Future Prospects

One inherent feature of performance measurements like the calibration of tagging efficiencies is that the finalization of one measurement is always the starting point of the next. In the context of the ongoing *Run 2* endeavors, this means that the $p_{\mathrm{T}}^{\mathrm{rel}}$ calibration method will be extended to the full data set recorded in 2016 with the ATLAS detector and that efforts to decrease systematic uncertainties will continue. As soon as data taking starts in 2017, efforts take place to provide an early calibration with the $p_{\mathrm{T}}^{\mathrm{rel}}$-method. For the upcoming data, the tagging algorithms discussed here also undergo further optimization and therefore have to be calibrated again. In addition, new tagging algorithms based on recurrent neural networks are under development (preparations for publication are internally documented in [99]).

The calibration using the $p_{\mathrm{T}}^{\mathrm{rel}}$-method can also be extended to include jets with different radius parameters, track-jets (clustered on particle tracks instead of calorimeter clusters), or particle flow jets (based on combining tracking and calorimeter information from all detector components) which are of particular interest for many future analyses.

Due to the low correlation between muon- and $t\bar{t}$-based calibration methods and the orthogonal phase-space, the different measurements of the b-tagging efficiency can be combined in a maximum likelihood approach. This has been done for *Run 1* calibrations as shown in Figure 11.2 [64].

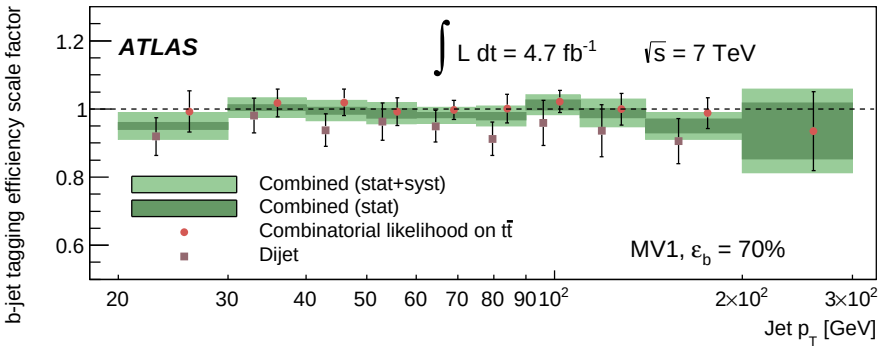

Figure 11.2.: Example for the combination of SFs as conducted in *Run 1* for the MV1 algorithm at a nominal efficiency of 70% [64].

Using b-tagging discriminants as an input for multivariate analysis techniques introduces a need for continuous calibration of the probability density function of the tagging algorithm. This can be achieved by a pseudo-continuous approach where the set of jets is divided in bins of the tagging discriminant. In each bin, the fit to the $p_{\mathrm{T}}^{\mathrm{rel}}$-variable can be performed, giving the fraction of b-jets which can be compared to **M**onte **C**arlo (MC) prediction. While this approach needs a higher amount of simulation statistics it is in principle achievable for upcoming *Run 2* measurements.

Another prospect currently under investigation is the possibility to use the $p_{\mathrm{T}}^{\mathrm{rel}}$-method for on-line monitoring of the **T**rigger and **D**ata **Aq**uisition (TDAQ) system. This means measuring the tagging efficiency on the recorded data directly before the full reconstruction chain. The most time consuming part of the measurement is the generation of the MC-templates, which can be done in advance. The required amount of data is much lower for the $p_{\mathrm{T}}^{\mathrm{rel}}$-method than for $t\bar{t}$-based methods, meaning the measurement can quickly and repeatedly be performed on incoming data. This would be a innovative way of monitoring the quality of flavor-tagging sensitive steps in the data taking and reconstruction chain and perform a direct measurement of on-line tagging algorithms.

The identification of b-jets is an important instrument in the search for **B**eyond **S**tandard **M**odel (BSM) physics, as mentioned before. However, with the increased center of mass energy and additional searches for boosted objects from high mass resonances, t-tagging becomes an increasingly important part of the flavor identification efforts in ATLAS as well. Current tagging techniques identify highly boosted t-quarks that decay hadronically into three jets that merge to one large-R jet that cannot properly be resolved. These large-R jets are probed for possible substructure giving hints to their origin. Since the branching fraction is largest for hadronically decaying t-quarks, currently all efforts are focused on that particular decay channel. However, in semileptonic t-quark decays, a similar problem can occur. While in the resolved regime, a lepton, a b-jet, and **m**issing $\boldsymbol{E}_{\mathbf{T}}$ (MET) can be selected, the lepton and jet become non-isolated in the boosted case. Here, the sensitivity of the $p_{\mathrm{T}}^{\mathrm{rel}}$-variable to the mass of the weakly decaying particle can be exploited. The decay kinematics of the $t \to Wb \to \mu\nu_{\mu}b$ is different to muons from other decays (i.e. b-, c-, or light-jets) due to the high W-mass. Therefore, the $p_{\mathrm{T}}^{\mathrm{rel}}$ of the muon in the b-jet or similar variables could be used to tag boosted semileptonic t-decays in the future.

A. Appendix

A.1. Check for η-Dependence

During *Run 1* calibration efforts, **s**cale **f**actors (SFs) have been calculated within bins of the pseudorapidity η^{jet}. No significant change in the measured SFs with respect to η^{jet} was observed. This is checked in *Run 2* as well, by dividing the data in each $p_{\text{T}}^{\text{jet}}$-bin into four η^{jet} bins with boundaries $[-2.5, -1.2, 0.0, 1.2, 2.5]$. The $p_{\text{T}}^{\text{rel}}$-distributions are then compared to each other in Figure A.1. No significant difference in the shapes is observed. An example for the modeling of the η^{jet} is also shown in Figure A.2 as well as the η^{jet}-dependence of the b-tagging efficiency in simulation. Despite the η^{jet}-distribution being dominated by structures generated by detector and reconstruction effects, the tagging efficiency has no systematic η^{jet}-dependence. While some deviations from an all flat efficiency can occur, as seen for the highest $p_{\text{T}}^{\text{jet}}$-bin in blue, no systematic dependence is visible.

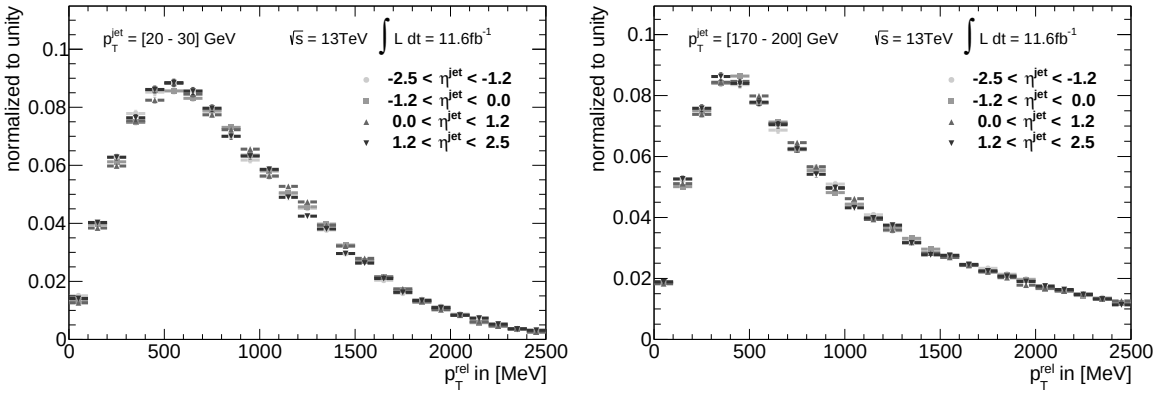

Figure A.1.: Distribution of $p_{\text{T}}^{\text{rel}}$ observed in data. Each $p_{\text{T}}^{\text{jet}}$-bin is divided into four η-bins as indicated by the different markers.

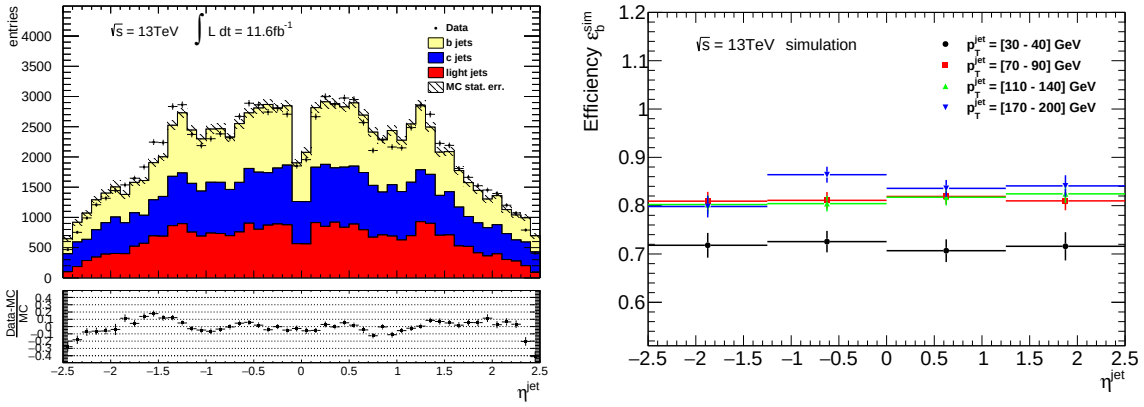

Figure A.2.: η^{jet}-distribution for jets compared to the MC prediction for the 50-70 GeV $p_{\text{T}}^{\text{jet}}$-bin (left). Dependence of the b-tagging efficiency on the η^{jet} for multiple $p_{\text{T}}^{\text{jet}}$-bins (right) determined on the muon filtered simulation.

A.2. The $p_{\mathrm{T}}^{\mathrm{rel}}$-Distributions

For the calibration measurement a high amount of $p_{\mathrm{T}}^{\mathrm{rel}}$-distributions is analyzed as discussed in Chapter 7. In *Run 2* a total of 4 **o**perating **p**oints (OPs) have been calibrated for 2 tagging algorithms in 9 bins of $p_{\mathrm{T}}^{\mathrm{jet}}$, each. Every SF determined this way relies on 2 fit results compared to 2 **M**onte **C**arlo (MC) flavor-fractions resulting in 4 histograms. This results in a total of 288 histograms for the nominal values. With about 30 uncertainties (including up and down variations) this procedure relies on $O(10^4)$ histograms which is neither practical nor particular useful to be printed here. In the following (Figures A.3 - A.5) the MV2c20 algorithm with the $\varepsilon_b^{\mathrm{nom.}} = 77\%$ is used to exemplary show the tagged and untagged fit in all $p_{\mathrm{T}}^{\mathrm{jet}}$-bins. For comparison the MC prediction for the same distribution is shown as well (Figures A.6 - A.8).

A.2.1. Fractions from Fit

The following histograms show the $p_{\mathrm{T}}^{\mathrm{rel}}$-distribution for the MV2c20 algorithm with the nominal efficiency $\varepsilon_b^{\mathrm{nom.}} = 77\%$ with the b-fraction obtained by the log-likelihood fit.

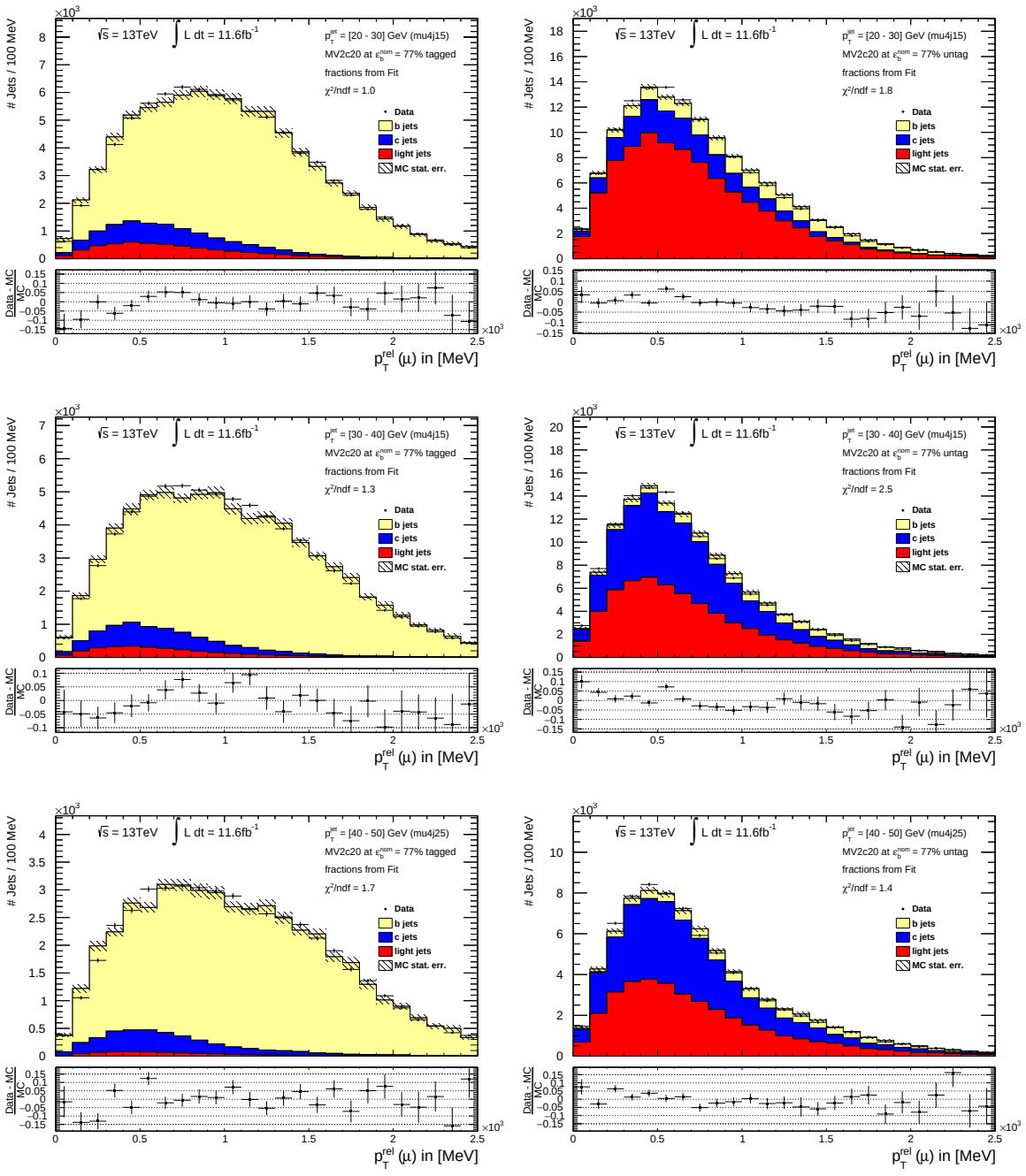

Figure A.3.: Distributions of $p_{\mathrm{T}}^{\mathrm{rel}}$ using b-tagged jets (left) and untagged jets (right). The black dots show the data while the templates are shown as a colored stack. The flavor fractions have been determined by the log-likelihood fit.

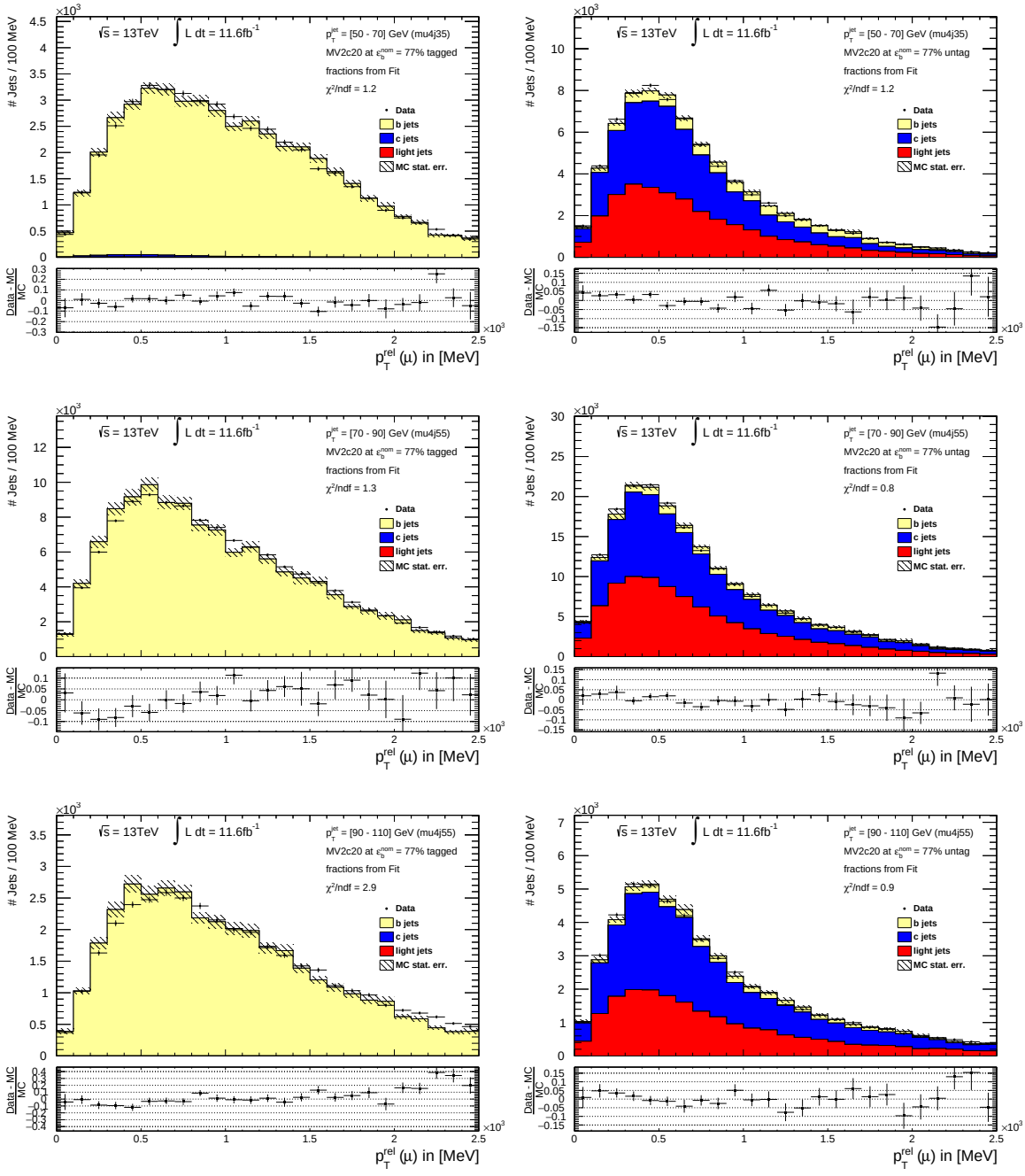

Figure A.4.: Distributions of $p_{\mathrm{T}}^{\mathrm{rel}}$ using b-tagged jets (left) and untagged jets (right). The black dots show the data while the templates are shown as a colored stack. The flavor fractions have been determined by the log-likelihood fit.

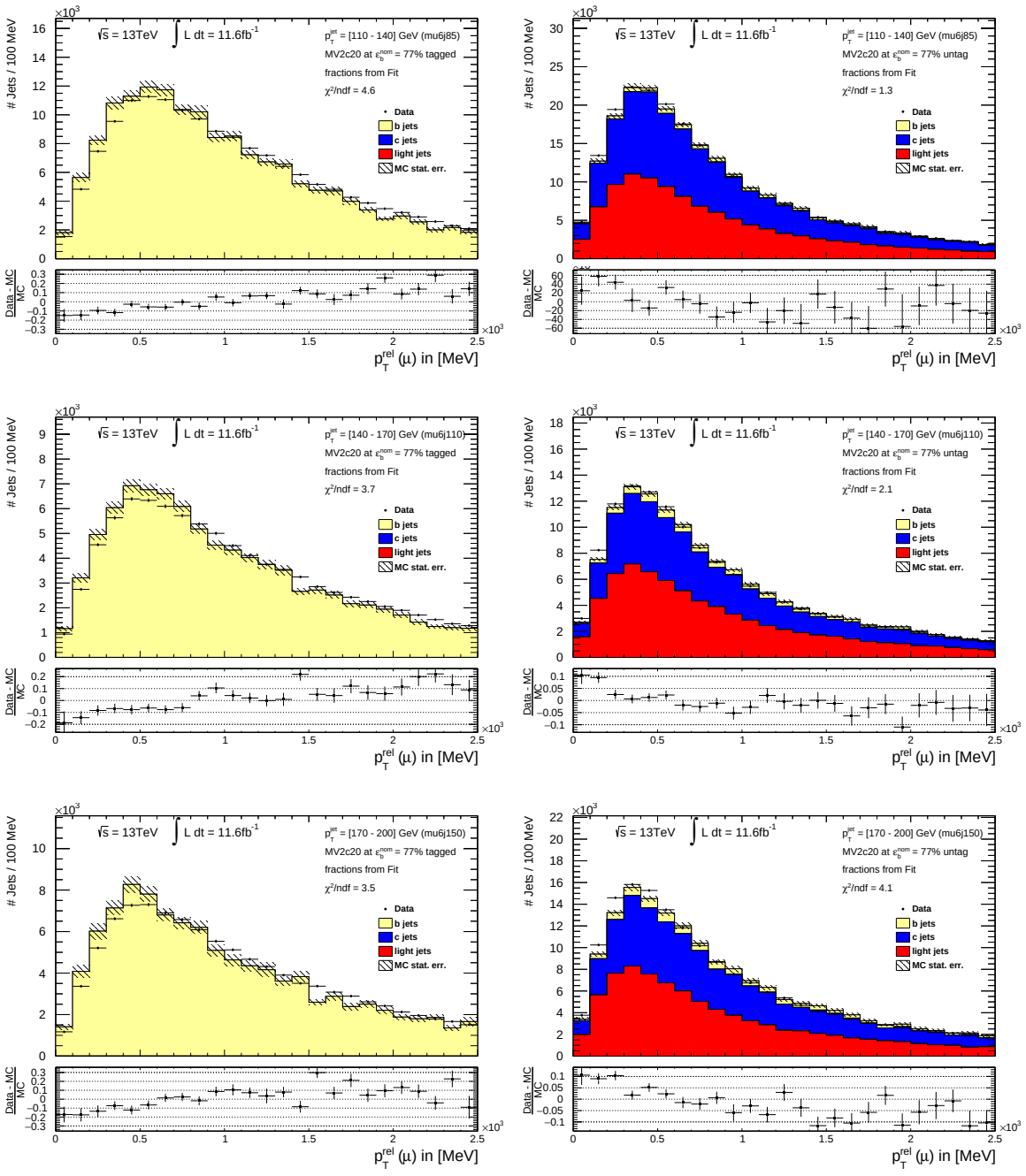

Figure A.5.: Distributions of $p_{\mathrm{T}}^{\mathrm{rel}}$ using b-tagged jets (left) and untagged jets (right). The black dots show the data while the templates are shown as a colored stack. The flavor fractions have been determined by the log-likelihood fit.

A.2.2. Fractions from Simulation

The following histograms show the $p_{\mathrm{T}}^{\mathrm{rel}}$-distribution for the MV2c20 algorithm with the nominal efficiency $\varepsilon_b^{\mathrm{nom.}} = 77\%$ with the b-fraction extracted from simulation.

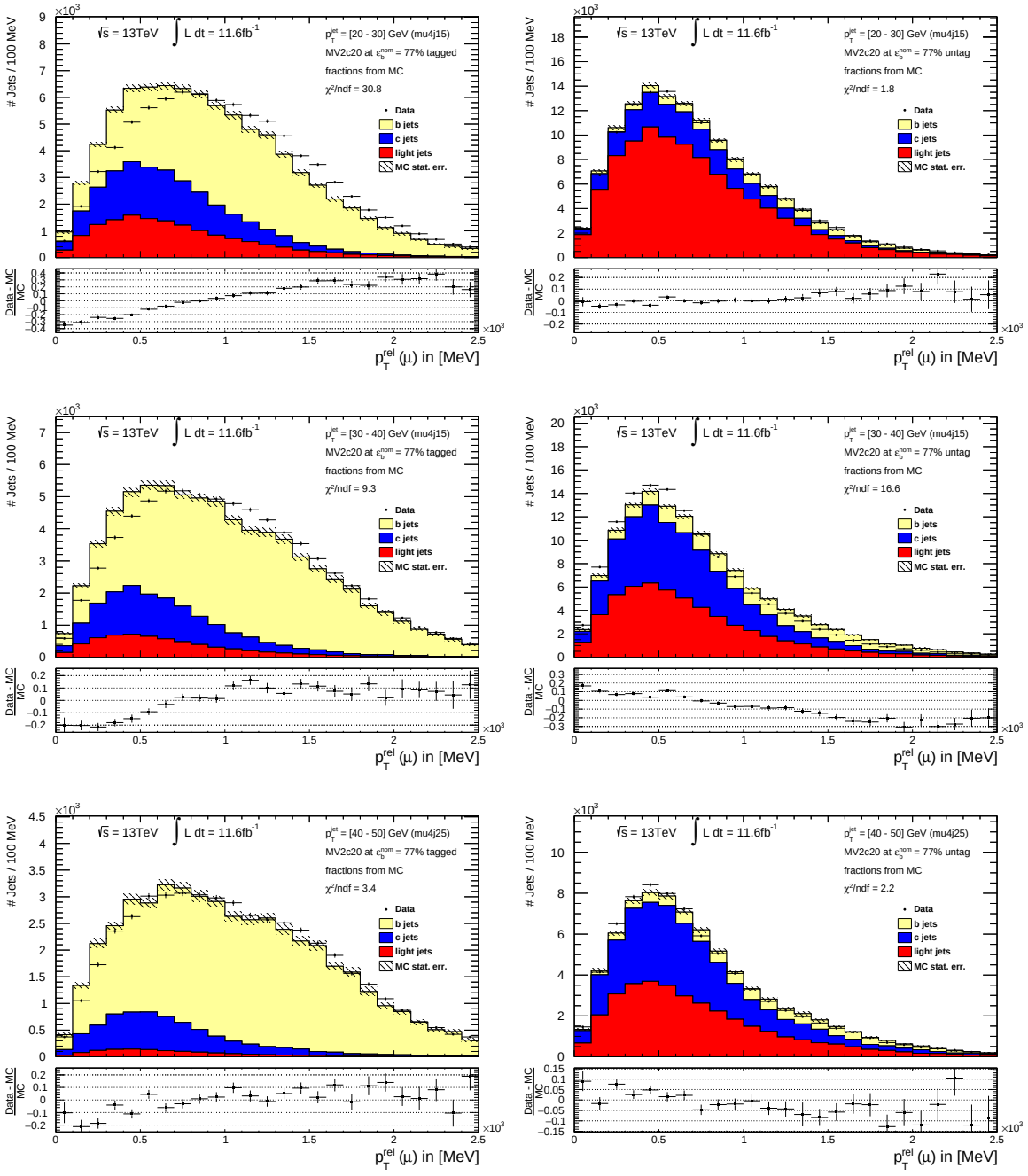

Figure A.6.: Distributions of $p_{\mathrm{T}}^{\mathrm{rel}}$ using b-tagged jets (left) and untagged jets (right). The black dots show the data while the templates are shown as a colored stack. The flavor fractions have been extracted from simulation.

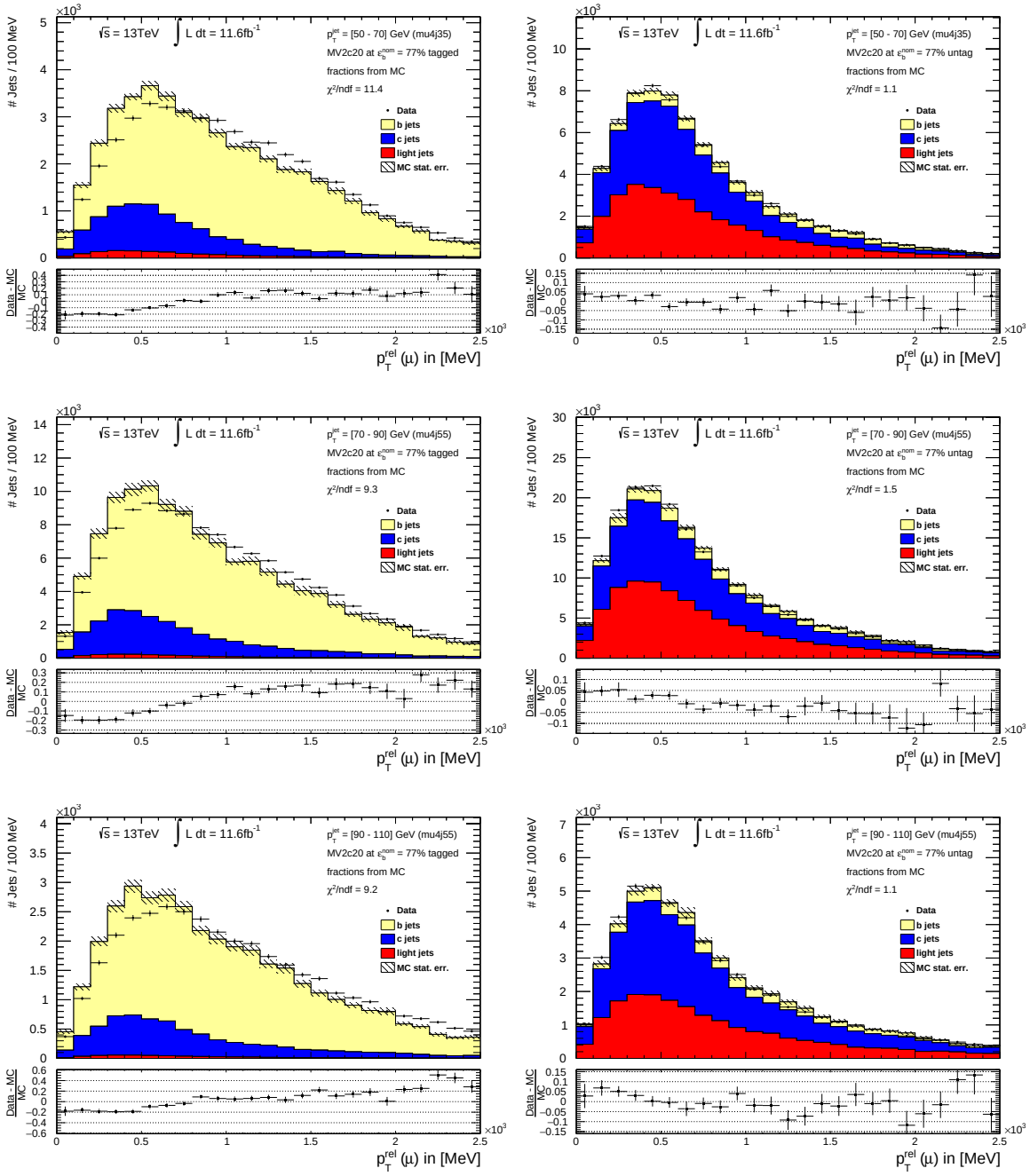

Figure A.7.: Distributions of $p_{\mathrm{T}}^{\mathrm{rel}}$ using b-tagged jets (left) and untagged jets (right). The black dots show the data while the templates are shown as a colored stack. The flavor fractions have been extracted from simulation.

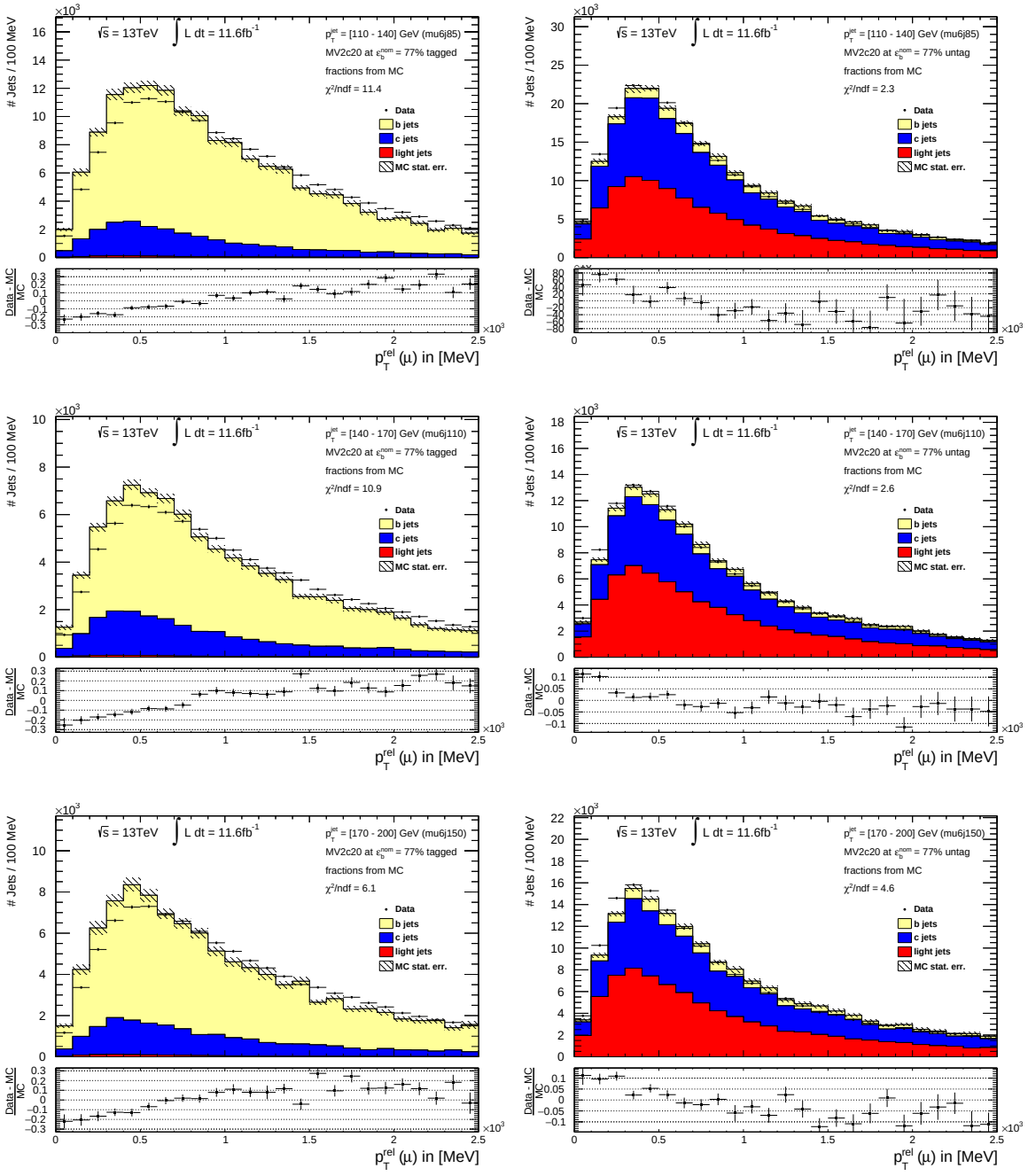

Figure A.8.: Distributions of $p_{\mathrm{T}}^{\mathrm{rel}}$ using b-tagged jets (left) and untagged jets (right). The black dots show the data while the templates are shown as a colored stack. The flavor fractions have been extracted from simulation.

A.3. Results of the Run 2 Calibration

As discussed in Chapter 8 the $p_{\mathrm{T}}^{\mathrm{rel}}$-fit has been used to measure the $p_{\mathrm{T}}^{\mathrm{jet}}$-dependent b-tagging efficiency. This has been done for the MV2c10 and MV2c20 tagging algorithms for four OPs as shown in Figure A.9. The results are shown in black dots with green uncertainty bands. The efficiency extracted from simulation is shown in gray. The nominal efficiency is indicated by a horizontal dashed line.

Comparing the efficiency to the expected values in simulation gives the SF $\kappa_b^{data/sim}$. Results obtained within this thesis are shown in Figure A.10 as black dots with green uncertainty bands. The OPs are shown with increasing $\varepsilon_b^{\mathrm{nom}}$ from top to bottom and the algorithms MV2c20 on the left and MV2c10 on the right.

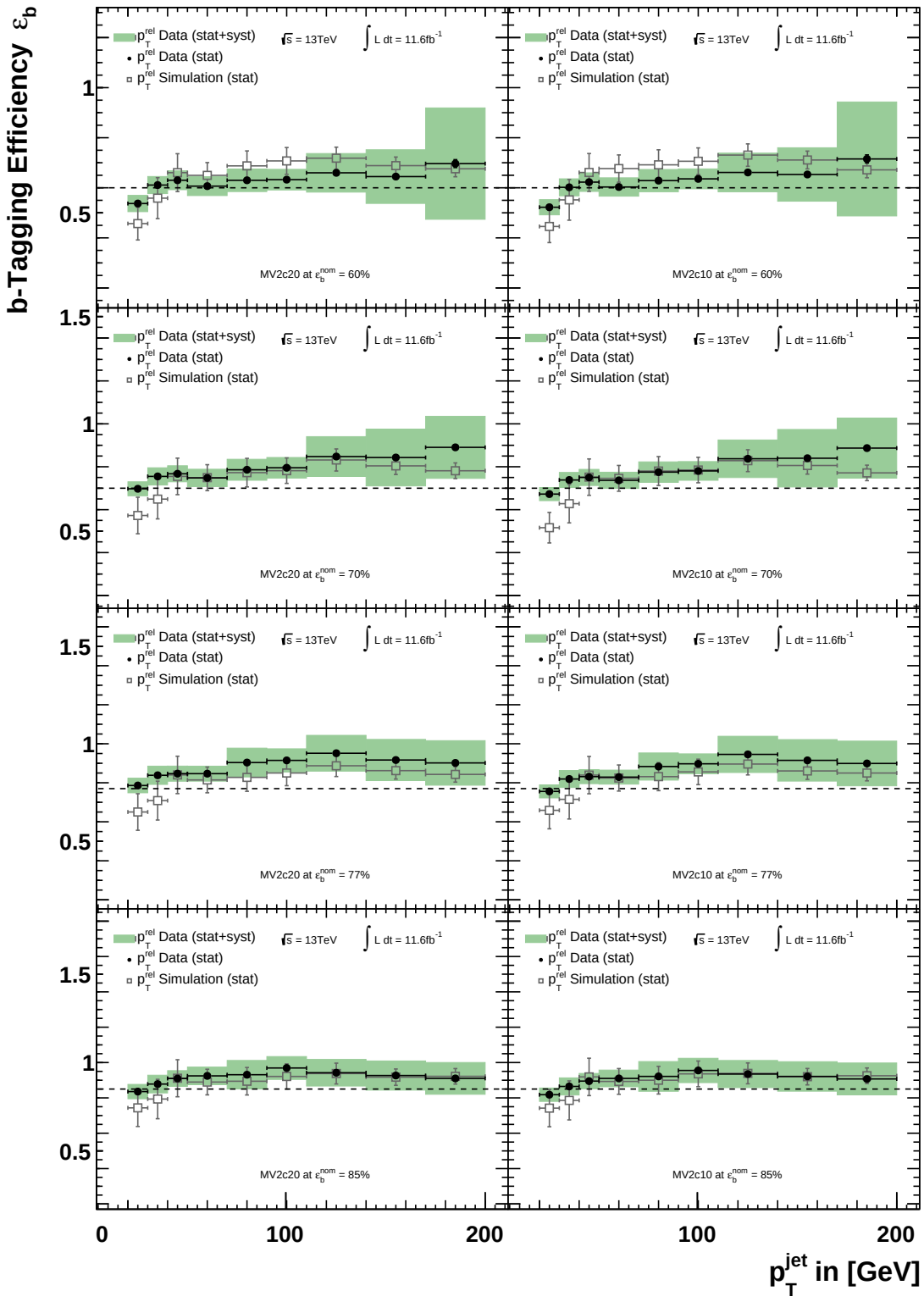

Figure A.9.: Results for ε_b measured by the p_T^{rel}-techniques (black) including uncertainties (green) compared to predictions from simulation (gray). Results are shown for different OPs (from top to bottom 60%, 70%, 77%, 85%) and taggers MV2c20 (left) and MV2c10 (right).

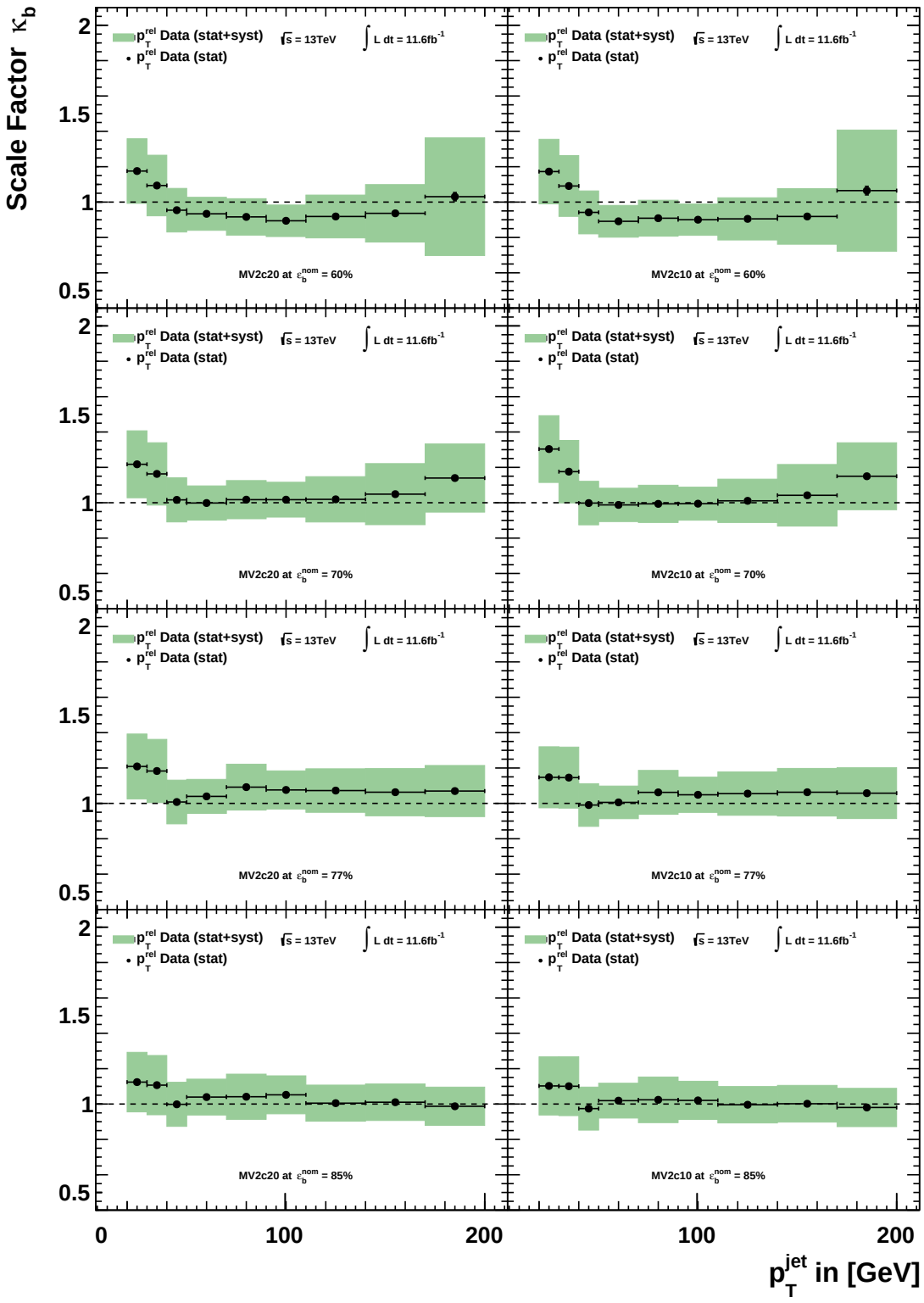

Figure A.10.: Scale factors as computed from the efficiency measurement are shown as black dots with green bands for systematic uncertainties. Results are shown for different OPs (from top to bottom 60%, 70%, 77%, 85%) for the MV2c20 tagger (left) and the MV2c10 tagger (right).

A.4. Run 2 Systematics Tables

For *Run 2* four OPs for two different trainings of the MV2 algorithm have been calibrated. Each of those corresponds to a separate measurement with the results shown in A.3. The uncertainty bands are computed by summing the respective uncertainties as discussed in Chapter 9 in quadrature. In the following the contributions are listed in tables to quantify the contribution of each systematic to each of the measurements.

Table A.1.: Systematic uncertainties for the MV2c10 tagging algorithm at 60% nominal b-tagging efficiency.

MV2c10 at $\varepsilon_b^{\text{nom}} = 60\%$	p_{T} in GeV								
Systematics [%]	20-30	30-40	40-50	50-70	70-90	90-110	110-140	140-170	170-200
Axis Smearing	0.4	0.7	0.8	0.7	2.4	2.3	7.3	8.0	12.5
B Fragmentation Fractions	-0.3	-0.5	-0.7	-0.4	-0.3	-0.3	-0.5	-0.3	-0.2
B Fragmentation Function	0.4	-0.1	-0.4	-0.2	-0.3	-0.5	-0.7	-1.2	-1.8
B JES Response	<0.1	0.2	0.4	0.5	0.3	<0.1	0.2	-0.1	0.4
B-Decay p* Spectrum	-3.5	-3.1	-2.8	-3.0	-2.5	-1.4	-0.8	-0.8	-1.1
BDecayFractions	0.5	0.6	0.7	0.9	1.2	1.1	1.2	1.2	1.3
Effective NP 1	0.7	1.2	1.5	1.0	-0.2	-0.3	0.8	-0.3	1.5
Effective NP 2	-0.1	<0.1	<0.1	0.1	0.1	<0.1	0.7	-1.0	-0.3
Effective NP 3	<0.1	<0.1	-0.2	<0.1	0.1	0.1	-0.4	0.1	-0.4
Effective NP 4	<0.1	<0.1	0.1	<0.1	-0.1	0.3	<0.1	0.3	-0.1
Effective NP 5	<0.1	<0.1	<0.1	<0.1	<0.1	0.1	<0.1	0.1	0.3
Effective NP Rest Term	<0.1	<0.1	0.2	0.1	-0.1	0.2	-0.1	0.2	0.3
Eta Intercalibration Modeling	0.3	0.5	0.7	0.4	-0.3	-0.7	0.7	-0.7	-0.1
Eta Intercalibration Total Stat	<0.1	0.2	0.3	0.2	-0.1	<0.1	<0.1	0.1	0.9
Fake Muons	-0.5	-0.2	-0.1	0.6	-0.4	2.2	0.7	-0.7	-1.9
Flavor Composition	0.8	0.6	0.9	0.6	-1.4	-1.0	0.8	-0.7	1.7
Flavor Response	-0.2	-0.1	-0.4	-0.1	0.6	0.4	-0.1	-0.3	-0.4
Gluon Splitting B	<0.1	0.1	0.5	1.1	2.3	2.0	3.3	4.8	5.9
Gluon Splitting C	<0.1	0.1	0.1	0.3	1.0	0.8	1.8	1.7	2.4
JER Single NP	-0.2	0.5	0.7	1.4	0.5	-0.6	-2.0	1.9	-2.6
JVT Efficiency	0.4	0.1	-0.8	-0.8	-0.7	<0.1	-1.0	-1.2	-1.1
LC-Ratio	1.1	-1.4	1.5	0.9	-3.1	<0.1	-6.0	-12.0	-27.5
Light Template Contamination	<0.1	<0.1	<0.1	<0.1	<0.1	<0.1	<0.1	<0.1	<0.1
Muon ID	<0.1	<0.1	<0.1	-0.1	0.2	0.1	-0.4	-0.1	<0.1
Muon MS	<0.1	<0.1	<0.1	<0.1	<0.1	0.1	0.3	-0.1	0.2
Muon Scale	-0.1	-0.1	<0.1	<0.1	-0.1	-0.1	-0.5	<0.1	-0.4
Pileup Offset Mu	<0.1	0.3	0.4	0.4	-0.1	-0.1	0.1	<0.1	1.1
Pileup Offset NPV	<0.1	0.3	<0.1	0.3	-0.2	-0.1	0.1	0.1	0.9
Pileup Pt Term	<0.1	<0.1	<0.1	<0.1	<0.1	<0.1	0.3	-0.1	-0.8
Pileup Rho Topology	0.2	0.3	0.7	0.3	-0.3	0.1	-0.1	0.7	1.6
SF to Inclusive	4.0	4.0	4.0	4.0	4.0	4.0	4.0	4.0	4.0
Template Statistics	1.2	0.8	-1.3	-1.6	-0.2	0.1	-2.0	1.3	-3.5
Simulation Statistics	14.4	14.7	11.4	8.1	8.7	7.6	6.1	5.0	4.7
Data Statistics	0.7	0.6	0.2	0.9	0.8	1.7	1.1	1.8	2.3
Total Systematics	15.6	15.7	12.9	10.1	11.2	9.7	13.1	17.0	32.1

Table A.2.: Systematic uncertainties for the MV2c10 tagging algorithm at 70% nominal b-tagging efficiency.

MV2c10 at $\varepsilon_b^{\text{nom}} = 70\%$	p_{T} in GeV								
Systematics [%]	20-30	30-40	40-50	50-70	70-90	90-110	110-140	140-170	170-200
Axis Smearing	0.3	0.5	0.8	0.5	2.0	2.0	6.4	6.9	0.3
B Fragmentation Fractions	0.1	-0.2	0.1	-0.3	-0.1	-0.2	-0.2	0.2	<0.1
B Fragmentation Function	0.2	0.1	<0.1	-0.1	-0.2	-0.3	-0.2	-0.4	-0.1
B JES Response	<0.1	<0.1	<0.1	0.3	0.1	<0.1	0.1	<0.1	<0.1
B-Decay p* Spectrum	-1.4	-1.1	-1.2	-1.9	-1.3	-0.7	-0.1	-0.1	<0.1
BDecayFractions	<0.1	<0.1	<0.1	0.6	0.6	0.6	0.5	0.4	<0.1
Effective NP 1	0.7	0.5	0.7	0.7	-0.4	-0.4	0.6	-0.2	0.1
Effective NP 2	-0.1	<0.1	<0.1	0.1	<0.1	-0.1	0.7	-0.8	<0.1
Effective NP 3	<0.1	<0.1	-0.1	<0.1	0.2	0.1	-0.4	<0.1	<0.1
Effective NP 4	<0.1	<0.1	<0.1	<0.1	-0.1	0.2	0.1	0.2	<0.1
Effective NP 5	-0.1	<0.1	<0.1	0.1	<0.1	0.1	<0.1	0.1	<0.1
Effective NP Rest Term	<0.1	<0.1	0.1	0.1	-0.1	0.1	<0.1	0.2	<0.1
Eta Intercalibration Modeling	0.1	0.2	0.4	0.3	-0.4	-0.7	0.6	-0.6	<0.1
Eta Intercalibration Total Stat	0.1	<0.1	0.2	0.1	-0.2	-0.1	<0.1	0.1	<0.1
Fake Muons	-0.1	0.2	0.2	0.5	-0.4	1.8	0.2	-0.5	-0.2
Flavor Composition	0.7	0.4	0.8	0.5	-1.2	-1.0	0.7	-0.7	0.1
Flavor Response	-0.2	-0.1	-0.4	-0.1	0.6	0.4	-0.1	-0.3	<0.1
Gluon Splitting B	<0.1	<0.1	<0.1	0.7	1.3	1.0	1.1	1.5	0.2
Gluon Splitting C	<0.1	0.1	0.1	0.3	0.9	0.7	1.7	1.6	0.1
JER Single NP	0.2	0.5	0.1	1.2	0.5	-0.6	-2.5	2.2	-0.1
JVT Efficiency	<0.1	-0.1	-0.6	-0.7	-0.5	0.2	-0.8	-1.0	-0.1
LC-Ratio	-0.2	-2.0	1.4	0.9	-3.0	<0.1	-6.1	-12.5	-15.3
Light Template Contamination	<0.1	<0.1	<0.1	<0.1	<0.1	<0.1	<0.1	<0.1	<0.1
Muon ID	<0.1	<0.1	-0.1	-0.1	0.1	0.1	-0.3	-0.1	<0.1
Muon MS	<0.1	<0.1	<0.1	<0.1	<0.1	<0.1	0.3	-0.1	<0.1
Muon Scale	<0.1	-0.1	<0.1	<0.1	-0.1	-0.1	-0.5	<0.1	<0.1
Pileup Offset Mu	<0.1	0.1	0.3	0.3	-0.2	-0.1	0.1	<0.1	<0.1
Pileup Offset NPV	0.1	0.2	-0.1	0.3	-0.2	-0.1	0.1	0.1	<0.1
Pileup Pt Term	<0.1	<0.1	-0.1	<0.1	<0.1	<0.1	0.3	<0.1	<0.1
Pileup Rho Topology	0.2	0.1	0.4	0.2	-0.4	0.1	-0.1	0.7	0.1
SF to Inclusive	4.0	4.0	4.0	4.0	4.0	4.0	4.0	4.0	4.0
Template Statistics	1.0	-0.2	1.4	-0.8	-0.6	-0.7	<0.1	4.3	-0.3
Simulation Statistics	13.8	14.2	11.3	8.1	8.6	7.6	6.1	5.0	4.7
Data Statistics	0.6	0.5	0.7	0.8	0.8	1.5	1.1	1.7	0.5
Total Systematics	14.5	15.0	12.3	9.5	10.6	9.3	12.1	16.6	16.5

Table A.3.: Systematic uncertainties for the MV2c10 tagging algorithm at 77% nominal b-tagging efficiency.

MV2c10 at $\varepsilon_b^{\text{nom}} = 77\%$	p_{T} in GeV								
Systematics [%]	20-30	30-40	40-50	50-70	70-90	90-110	110-140	140-170	170-200
Axis Smearing	0.2	0.5	0.6	0.3	1.6	1.6	0.4	0.3	0.3
B Fragmentation Fractions	0.1	-0.1	0.1	<0.1	<0.1	-0.1	<0.1	<0.1	<0.1
B Fragmentation Function	0.1	<0.1	<0.1	<0.1	-0.1	-0.1	<0.1	<0.1	-0.1
B JES Response	<0.1	<0.1	<0.1	<0.1	<0.1	-0.1	<0.1	<0.1	<0.1
B-Decay p* Spectrum	-0.1	-0.2	<0.1	-0.4	-0.4	<0.1	<0.1	<0.1	-0.1
BDecayFractions	<0.1	-0.1	<0.1	-0.1	0.3	0.2	<0.1	<0.1	0.1
Effective NP 1	0.5	0.3	0.6	0.3	-0.4	-0.4	<0.1	<0.1	0.1
Effective NP 2	-0.1	<0.1	<0.1	<0.1	<0.1	-0.1	<0.1	<0.1	<0.1
Effective NP 3	<0.1	<0.1	<0.1	<0.1	0.2	0.1	<0.1	<0.1	<0.1
Effective NP 4	<0.1	<0.1	<0.1	-0.1	-0.1	0.1	<0.1	<0.1	<0.1
Effective NP 5	<0.1	<0.1	<0.1	0.1	<0.1	0.1	<0.1	<0.1	<0.1
Effective NP Rest Term	<0.1	<0.1	0.1	0.1	-0.1	0.1	<0.1	<0.1	<0.1
Eta Intercalibration Modeling	0.1	0.1	0.3	0.2	-0.4	-0.6	<0.1	<0.1	<0.1
Eta Intercalibration Total Stat	0.1	<0.1	0.2	<0.1	-0.2	-0.2	<0.1	<0.1	<0.1
Fake Muons	<0.1	0.2	0.2	0.4	-0.3	1.5	<0.1	<0.1	-0.1
Flavor Composition	0.5	0.3	0.7	0.5	-1.0	-0.9	<0.1	<0.1	0.1
Flavor Response	-0.2	<0.1	-0.3	-0.1	0.4	0.4	<0.1	<0.1	<0.1
Gluon Splitting B	<0.1	<0.1	<0.1	<0.1	0.5	0.2	<0.1	0.1	0.3
Gluon Splitting C	<0.1	0.1	0.1	0.3	0.8	0.6	0.1	0.1	<0.1
JER Single NP	0.2	0.4	0.1	0.9	0.4	-0.4	-0.2	<0.1	-0.1
JVT Efficiency	-0.1	-0.1	-0.5	-0.6	-0.3	0.4	<0.1	-0.1	<0.1
LC-Ratio	-1.6	-3.4	-0.7	-0.4	-5.5	-2.2	-9.0	-10.9	-12.1
Light Template Contamination	<0.1	<0.1	<0.1	<0.1	<0.1	<0.1	<0.1	<0.1	<0.1
Muon ID	<0.1	<0.1	<0.1	-0.1	0.1	0.1	<0.1	<0.1	<0.1
Muon MS	<0.1	<0.1	<0.1	<0.1	<0.1	<0.1	<0.1	<0.1	<0.1
Muon Scale	<0.1	<0.1	<0.1	<0.1	-0.1	-0.1	<0.1	<0.1	<0.1
Pileup Offset Mu	<0.1	0.1	0.3	0.1	-0.2	-0.1	<0.1	<0.1	<0.1
Pileup Offset NPV	<0.1	0.2	-0.1	0.1	-0.2	-0.1	<0.1	<0.1	<0.1
Pileup Pt Term	<0.1	<0.1	-0.1	<0.1	<0.1	<0.1	<0.1	<0.1	<0.1
Pileup Rho Topology	0.1	0.1	0.3	0.1	-0.3	<0.1	<0.1	<0.1	<0.1
SF to Inclusive	4.0	4.0	4.0	4.0	4.0	4.0	4.0	4.0	4.0
Template Statistics	0.6	0.4	0.1	0.3	3.1	1.5	-0.3	0.8	-0.3
Simulation Statistics	14.4	14.1	11.4	8.1	8.6	7.6	6.2	5.0	4.7
Data Statistics	0.5	0.5	0.6	0.8	0.7	1.4	0.3	0.4	0.4
Total Systematics	15.0	15.1	12.2	9.2	11.7	9.4	11.6	12.7	13.6

Table A.4.: Systematic uncertainties for the MV2c10 tagging algorithm at 85% nominal b-tagging efficiency.

MV2c10 at $\varepsilon_b^{\text{nom}} = 85\%$	p_{T} in GeV								
Systematics [%]	20-30	30-40	40-50	50-70	70-90	90-110	110-140	140-170	170-200
Axis Smearing	<0.1	0.1	0.3	0.2	0.1	0.1	0.2	0.2	0.2
B Fragmentation Fractions	0.1	<0.1	0.1	<0.1	0.1	<0.1	<0.1	<0.1	<0.1
B Fragmentation Function	<0.1	<0.1	<0.1	<0.1	<0.1	<0.1	<0.1	-0.1	-0.1
B JES Response	<0.1	<0.1	-0.1	<0.1	-0.1	<0.1	<0.1	<0.1	<0.1
B-Decay p* Spectrum	0.3	0.5	0.4	0.3	0.4	0.1	-0.1	-0.1	-0.1
BDecayFractions	-0.1	-0.1	-0.1	-0.1	-0.2	-0.1	0.1	0.1	0.1
Effective NP 1	0.1	<0.1	0.3	0.1	-0.1	-0.1	<0.1	<0.1	<0.1
Effective NP 2	<0.1	<0.1	<0.1	<0.1	<0.1	<0.1	<0.1	<0.1	<0.1
Effective NP 3	<0.1	<0.1	<0.1	<0.1	0.1	<0.1	<0.1	<0.1	<0.1
Effective NP 4	<0.1	<0.1	<0.1	<0.1	<0.1	<0.1	<0.1	<0.1	<0.1
Effective NP 5	<0.1	<0.1	<0.1	0.1	<0.1	<0.1	<0.1	<0.1	<0.1
Effective NP Rest Term	<0.1	<0.1	0.1	0.1	<0.1	<0.1	<0.1	<0.1	<0.1
Eta Intercalibration Modeling	<0.1	<0.1	0.2	0.1	-0.1	-0.1	<0.1	<0.1	<0.1
Eta Intercalibration Total Stat	<0.1	<0.1	0.1	<0.1	<0.1	<0.1	<0.1	<0.1	<0.1
Fake Muons	0.1	0.1	0.2	0.3	<0.1	0.1	<0.1	<0.1	<0.1
Flavor Composition	<0.1	<0.1	0.4	0.2	-0.1	-0.1	<0.1	<0.1	<0.1
Flavor Response	<0.1	<0.1	-0.2	-0.1	<0.1	<0.1	<0.1	<0.1	<0.1
Gluon Splitting B	<0.1	<0.1	<0.1	-0.1	-0.4	-0.2	<0.1	<0.1	-0.1
Gluon Splitting C	<0.1	<0.1	0.1	0.2	0.1	<0.1	<0.1	<0.1	<0.1
JER Single NP	0.2	0.1	0.1	0.4	<0.1	<0.1	<0.1	<0.1	<0.1
JVT Efficiency	-0.1	<0.1	-0.3	-0.4	<0.1	0.1	<0.1	<0.1	<0.1
LC-Ratio	-2.3	-3.9	-2.4	-3.0	-8.2	-6.0	-7.2	-8.1	-9.1
Light Template Contamination	<0.1	<0.1	<0.1	<0.1	<0.1	<0.1	<0.1	<0.1	<0.1
Muon ID	<0.1	<0.1	<0.1	-0.1	<0.1	<0.1	<0.1	<0.1	<0.1
Muon MS	<0.1	<0.1	<0.1	<0.1	<0.1	<0.1	<0.1	<0.1	<0.1
Muon Scale	<0.1	<0.1	<0.1	<0.1	<0.1	<0.1	<0.1	<0.1	<0.1
Pileup Offset Mu	<0.1	<0.1	0.2	0.1	<0.1	<0.1	<0.1	<0.1	<0.1
Pileup Offset NPV	<0.1	<0.1	-0.1	0.1	-0.1	<0.1	<0.1	<0.1	<0.1
Pileup Pt Term	<0.1	<0.1	<0.1	<0.1	<0.1	<0.1	<0.1	<0.1	<0.1
Pileup Rho Topology	<0.1	<0.1	0.2	<0.1	-0.1	<0.1	<0.1	<0.1	<0.1
SF to Inclusive	4.0	4.0	4.0	4.0	4.0	4.0	4.0	4.0	4.0
Template Statistics	<0.1	-0.2	-0.7	-0.9	-0.3	-0.3	<0.1	0.4	-0.3
Simulation Statistics	14.2	14.0	11.5	8.2	8.7	7.8	6.3	5.0	4.8
Data Statistics	0.3	0.3	0.6	0.7	0.2	0.4	0.2	0.3	0.3
Total Systematics	14.9	15.1	12.5	9.7	12.6	10.6	10.3	10.4	11.0

Table A.5.: Systematic uncertainties for the MV2c20 tagging algorithm at 60% nominal b-tagging efficiency.

MV2c20 at $\varepsilon_b^{\text{nom}} = 60\%$	p_{T} in GeV								
Systematics [%]	20-30	30-40	40-50	50-70	70-90	90-110	110-140	140-170	170-200
Axis Smearing	0.4	0.7	0.8	0.7	2.5	2.2	7.4	8.0	12.6
B Fragmentation Fractions	-0.3	-0.5	-0.6	-0.4	-0.3	-0.3	-0.4	-0.3	-0.1
B Fragmentation Function	0.4	-0.1	-0.4	-0.2	-0.3	-0.5	-0.8	-1.2	-1.9
B JES Response	<0.1	0.2	0.3	0.5	0.3	<0.1	0.2	-0.1	0.4
B-Decay p* Spectrum	-3.4	-3.0	-2.8	-3.0	-2.5	-1.4	-0.8	-0.8	-1.2
BDecayFractions	0.4	0.6	0.7	0.9	1.1	1.1	1.2	1.2	1.4
Effective NP 1	0.7	1.1	1.5	1.0	-0.3	-0.3	0.9	-0.3	1.5
Effective NP 2	-0.1	<0.1	<0.1	0.1	0.1	<0.1	0.8	-1.0	-0.3
Effective NP 3	<0.1	<0.1	-0.2	<0.1	0.1	0.1	-0.5	0.1	-0.5
Effective NP 4	<0.1	<0.1	0.1	<0.1	-0.1	0.3	<0.1	0.3	<0.1
Effective NP 5	<0.1	<0.1	<0.1	<0.1	<0.1	0.1	<0.1	0.1	0.3
Effective NP Rest Term	<0.1	<0.1	0.2	0.1	-0.1	0.2	-0.1	0.2	0.3
Eta Intercalibration Modeling	0.3	0.5	0.7	0.4	-0.3	-0.7	0.7	-0.7	-0.1
Eta Intercalibration Total Stat	<0.1	0.2	0.3	0.2	-0.2	<0.1	<0.1	0.1	0.9
Fake Muons	-0.5	-0.2	-0.1	0.6	-0.4	2.2	0.7	-0.8	-1.8
Flavor Composition	0.8	0.6	0.9	0.6	-1.4	-1.1	0.8	-0.7	1.6
Flavor Response	-0.2	-0.1	-0.4	-0.1	0.6	0.4	-0.1	-0.3	-0.4
Gluon Splitting B	<0.1	0.1	0.5	1.1	2.3	2.1	3.4	4.9	6.3
Gluon Splitting C	<0.1	0.1	0.1	0.3	1.0	0.8	1.8	1.8	2.4
JER Single NP	-0.2	0.5	0.7	1.4	0.6	-0.6	-2.0	1.9	-2.5
JVT Efficiency	0.3	0.1	-0.8	-0.9	-0.7	0.1	-1.0	-1.2	-1.1
LC-Ratio	1.2	-1.4	1.5	0.9	-3.2	<0.1	-6.1	-12.1	-27.2
Light Template Contamination	<0.1	<0.1	<0.1	<0.1	<0.1	<0.1	<0.1	<0.1	<0.1
Muon ID	<0.1	<0.1	-0.1	-0.1	0.2	0.1	-0.4	-0.1	<0.1
Muon MS	<0.1	<0.1	<0.1	<0.1	<0.1	0.1	0.3	-0.1	0.2
Muon Scale	<0.1	-0.1	<0.1	<0.1	-0.1	-0.2	-0.5	<0.1	-0.4
Pileup Offset Mu	<0.1	0.3	0.4	0.4	-0.2	-0.1	0.1	<0.1	1.1
Pileup Offset NPV	<0.1	0.3	<0.1	0.3	-0.2	-0.1	0.1	0.1	0.9
Pileup Pt Term	<0.1	<0.1	<0.1	<0.1	<0.1	<0.1	0.3	-0.1	-0.8
Pileup Rho Topology	0.2	0.3	0.7	0.3	-0.4	0.1	-0.1	0.7	1.6
SF to Inclusive	4.0	4.0	4.0	4.0	4.0	4.0	4.0	4.0	4.0
Template Statistics	-2.2	-0.3	-1.4	-2.0	-0.3	-1.7	<0.1	-2.6	5.3
Simulation Statistics	14.3	14.6	11.5	7.8	8.7	7.6	6.1	5.0	4.7
Data Statistics	0.7	0.6	0.2	1.0	0.8	1.7	1.1	1.8	2.3
Total Systematics	15.5	15.7	12.9	10.0	11.2	9.8	13.1	17.3	32.2

Table A.6.: Systematic uncertainties for the MV2c20 tagging algorithm at 70% nominal b-tagging efficiency.

MV2c20 at $\varepsilon_b^{\text{nom}} = 70\%$	p_{T} in GeV								
Systematics [%]	20-30	30-40	40-50	50-70	70-90	90-110	110-140	140-170	170-200
Axis Smearing	0.3	0.6	0.7	0.5	2.0	2.0	6.5	7.0	0.3
B Fragmentation Fractions	0.1	-0.2	-0.4	-0.3	-0.1	-0.2	-0.2	0.2	<0.1
B Fragmentation Function	0.2	0.1	-0.1	-0.1	-0.2	-0.2	-0.2	-0.4	<0.1
B JES Response	<0.1	<0.1	0.1	0.3	0.1	-0.1	0.1	<0.1	<0.1
B-Decay p* Spectrum	-1.9	-1.5	-1.7	-1.9	-1.3	-0.6	-0.1	-0.2	<0.1
BDecayFractions	<0.1	<0.1	0.2	0.6	0.6	0.6	0.5	0.4	<0.1
Effective NP 1	0.7	0.5	1.0	0.7	-0.4	-0.4	0.6	-0.2	0.1
Effective NP 2	-0.1	<0.1	<0.1	<0.1	<0.1	-0.1	0.7	-0.8	<0.1
Effective NP 3	<0.1	<0.1	-0.1	<0.1	0.2	0.2	-0.4	<0.1	<0.1
Effective NP 4	<0.1	<0.1	0.1	<0.1	-0.1	0.2	0.1	0.3	<0.1
Effective NP 5	-0.1	<0.1	<0.1	0.1	<0.1	0.1	<0.1	0.1	<0.1
Effective NP Rest Term	<0.1	<0.1	0.1	0.1	-0.1	0.1	<0.1	0.2	<0.1
Eta Intercalibration Modeling	0.1	0.2	0.5	0.3	-0.4	-0.7	0.6	-0.6	<0.1
Eta Intercalibration Total Stat	0.1	<0.1	0.3	0.1	-0.2	-0.1	<0.1	0.1	<0.1
Fake Muons	-0.1	0.2	<0.1	0.5	-0.4	1.9	0.2	-0.5	-0.2
Flavor Composition	0.7	0.4	0.8	0.6	-1.3	-1.1	0.7	-0.7	0.1
Flavor Response	-0.2	-0.1	-0.4	-0.1	0.6	0.4	-0.1	-0.3	<0.1
Gluon Splitting B	<0.1	<0.1	0.2	0.7	1.2	0.9	1.0	1.4	0.2
Gluon Splitting C	<0.1	0.1	0.1	0.3	0.9	0.7	1.7	1.7	0.1
JER Single NP	0.1	0.6	0.1	1.2	0.5	-0.6	-2.7	2.2	-0.1
JVT Efficiency	<0.1	-0.1	-0.6	-0.8	-0.5	0.3	-0.8	-1.0	-0.1
LC-Ratio	-0.7	-2.5	0.9	0.9	-3.1	<0.1	-6.3	-12.6	-15.3
Light Template Contamination	<0.1	<0.1	<0.1	<0.1	<0.1	<0.1	<0.1	<0.1	<0.1
Muon ID	<0.1	<0.1	<0.1	-0.1	0.1	0.1	-0.3	-0.1	<0.1
Muon MS	<0.1	<0.1	<0.1	<0.1	<0.1	<0.1	0.3	-0.1	<0.1
Muon Scale	<0.1	-0.1	<0.1	<0.1	-0.1	-0.1	-0.5	-0.1	<0.1
Pileup Offset Mu	<0.1	0.1	0.4	0.3	-0.2	-0.1	0.1	0.1	<0.1
Pileup Offset NPV	0.1	0.2	-0.1	0.3	-0.2	-0.1	0.1	0.1	<0.1
Pileup Pt Term	<0.1	<0.1	<0.1	<0.1	<0.1	<0.1	0.3	<0.1	<0.1
Pileup Rho Topology	0.2	0.1	0.5	0.2	-0.4	0.1	-0.1	0.7	0.1
SF to Inclusive	4.0	4.0	4.0	4.0	4.0	4.0	4.0	4.0	4.0
Template Statistics	-0.1	1.6	0.1	-1.9	-0.8	-2.4	2.5	2.8	-3.6
Simulation Statistics	14.8	14.2	11.3	8.1	8.6	7.6	6.2	5.0	4.7
Data Statistics	0.6	0.5	0.7	0.8	0.8	1.6	1.1	1.7	0.5
Total Systematics	15.6	15.2	12.3	9.7	10.6	9.6	12.5	16.4	16.9

Table A.7.: Systematic uncertainties for the MV2c20 tagging algorithm at 77% nominal b-tagging efficiency.

MV2c20 at $\varepsilon_b^{\text{nom}} = 77\%$	p_{T} in GeV								
Systematics [%]	20-30	30-40	40-50	50-70	70-90	90-110	110-140	140-170	170-200
Axis Smearing	0.2	0.5	0.6	0.3	1.7	1.7	0.4	0.3	0.3
B Fragmentation Fractions	0.1	-0.1	0.1	<0.1	<0.1	-0.1	<0.1	<0.1	<0.1
B Fragmentation Function	0.1	<0.1	<0.1	<0.1	-0.1	-0.1	<0.1	<0.1	-0.1
B JES Response	<0.1	<0.1	<0.1	<0.1	<0.1	-0.1	<0.1	<0.1	<0.1
B-Decay p* Spectrum	-0.1	-0.1	<0.1	-0.8	-0.3	<0.1	<0.1	<0.1	-0.1
BDecayFractions	<0.1	-0.1	<0.1	<0.1	0.2	0.2	<0.1	<0.1	0.1
Effective NP 1	0.5	0.4	0.6	0.3	-0.4	-0.5	<0.1	<0.1	0.1
Effective NP 2	-0.1	<0.1	<0.1	<0.1	<0.1	-0.2	<0.1	<0.1	<0.1
Effective NP 3	<0.1	<0.1	<0.1	<0.1	0.2	0.2	<0.1	<0.1	<0.1
Effective NP 4	<0.1	<0.1	<0.1	-0.1	-0.1	0.1	<0.1	<0.1	<0.1
Effective NP 5	<0.1	<0.1	<0.1	0.1	<0.1	0.1	<0.1	<0.1	<0.1
Effective NP Rest Term	<0.1	<0.1	0.1	0.1	-0.1	0.1	<0.1	<0.1	<0.1
Eta Intercalibration Modeling	0.1	0.1	0.3	0.2	-0.4	-0.7	<0.1	<0.1	<0.1
Eta Intercalibration Total Stat	0.1	<0.1	0.2	<0.1	-0.2	-0.2	<0.1	<0.1	<0.1
Fake Muons	<0.1	0.2	0.2	0.4	-0.3	1.5	<0.1	<0.1	-0.1
Flavor Composition	0.5	0.3	0.7	0.5	-1.0	-1.0	<0.1	<0.1	0.1
Flavor Response	-0.2	<0.1	-0.3	-0.1	0.5	0.4	<0.1	<0.1	<0.1
Gluon Splitting B	<0.1	<0.1	<0.1	0.1	0.3	0.1	<0.1	0.1	0.3
Gluon Splitting C	<0.1	0.1	0.1	0.3	0.8	0.7	0.1	0.1	<0.1
JER Single NP	0.2	0.4	0.1	0.9	0.4	-0.6	-0.2	<0.1	-0.1
JVT Efficiency	-0.1	-0.1	-0.5	-0.7	-0.3	0.4	<0.1	-0.1	<0.1
LC-Ratio	-2.3	-3.6	-1.1	-0.9	-6.4	-3.1	-8.7	-10.8	-12.0
Light Template Contamination	<0.1	<0.1	<0.1	<0.1	<0.1	<0.1	<0.1	<0.1	<0.1
Muon ID	<0.1	<0.1	<0.1	-0.1	0.1	0.1	<0.1	<0.1	<0.1
Muon MS	<0.1	<0.1	<0.1	<0.1	<0.1	<0.1	<0.1	<0.1	<0.1
Muon Scale	<0.1	-0.1	<0.1	<0.1	-0.1	-0.1	<0.1	<0.1	<0.1
Pileup Offset Mu	<0.1	0.1	0.3	0.1	-0.2	-0.1	<0.1	<0.1	<0.1
Pileup Offset NPV	<0.1	0.2	-0.1	0.1	-0.3	-0.2	<0.1	<0.1	<0.1
Pileup Pt Term	<0.1	<0.1	-0.1	<0.1	<0.1	-0.1	<0.1	<0.1	<0.1
Pileup Rho Topology	0.1	0.1	0.4	0.1	-0.4	<0.1	<0.1	<0.1	<0.1
SF to Inclusive	4.0	4.0	4.0	4.0	4.0	4.0	4.0	4.0	4.0
Template Statistics	-0.9	-1.0	-1.2	-0.8	-1.9	-2.5	-0.7	-0.2	0.4
Simulation Statistics	14.4	14.1	11.4	8.1	8.6	7.6	6.2	5.0	4.7
Data Statistics	0.5	0.5	0.6	0.7	0.7	1.4	0.3	0.4	0.4
Total Systematics	15.2	15.1	12.3	9.2	11.9	9.9	11.5	12.6	13.5

Table A.8.: Systematic uncertainties for the MV2c20 tagging algorithm at 85% nominal b-tagging efficiency.

MV2c20 at $\varepsilon_b^{\text{nom}} = 85\%$	p_{T} in GeV								
Systematics [%]	20-30	30-40	40-50	50-70	70-90	90-110	110-140	140-170	170-200
Axis Smearing	<0.1	0.1	0.2	<0.1	0.1	0.1	0.2	0.2	0.2
B Fragmentation Fractions	0.1	<0.1	0.1	0.1	0.1	<0.1	<0.1	<0.1	<0.1
B Fragmentation Function	<0.1	<0.1	0.1	<0.1	<0.1	<0.1	-0.1	-0.1	-0.1
B JES Response	<0.1	<0.1	-0.1	-0.1	-0.1	<0.1	<0.1	<0.1	<0.1
B-Decay p* Spectrum	0.7	0.4	0.5	0.4	0.3	<0.1	-0.1	-0.1	-0.1
BDecayFractions	-0.1	-0.1	-0.1	-0.1	-0.2	<0.1	0.1	0.1	0.1
Effective NP 1	0.1	<0.1	0.2	<0.1	-0.1	<0.1	<0.1	<0.1	<0.1
Effective NP 2	<0.1	<0.1	<0.1	<0.1	<0.1	<0.1	<0.1	<0.1	<0.1
Effective NP 3	<0.1	<0.1	<0.1	<0.1	0.1	<0.1	<0.1	<0.1	<0.1
Effective NP 4	<0.1	<0.1	<0.1	<0.1	<0.1	<0.1	<0.1	<0.1	<0.1
Effective NP 5	<0.1	<0.1	<0.1	<0.1	<0.1	<0.1	<0.1	<0.1	<0.1
Effective NP Rest Term	<0.1	<0.1	<0.1	<0.1	<0.1	<0.1	<0.1	<0.1	<0.1
Eta Intercalibration Modeling	<0.1	<0.1	<0.1	<0.1	-0.1	-0.1	<0.1	<0.1	<0.1
Eta Intercalibration Total Stat	<0.1	<0.1	<0.1	<0.1	<0.1	<0.1	<0.1	<0.1	<0.1
Fake Muons	0.1	0.1	0.1	0.1	<0.1	0.1	<0.1	<0.1	<0.1
Flavor Composition	0.1	0.1	0.3	0.1	-0.1	-0.1	<0.1	<0.1	<0.1
Flavor Response	<0.1	<0.1	-0.1	<0.1	<0.1	<0.1	<0.1	<0.1	<0.1
Gluon Splitting B	<0.1	<0.1	-0.1	-0.2	-0.3	<0.1	0.1	0.2	0.1
Gluon Splitting C	<0.1	<0.1	<0.1	0.1	0.1	<0.1	<0.1	<0.1	<0.1
JER Single NP	0.1	0.2	<0.1	0.2	<0.1	-0.1	<0.1	<0.1	<0.1
JVT Efficiency	-0.1	<0.1	-0.2	-0.1	<0.1	<0.1	<0.1	<0.1	<0.1
LC-Ratio	-2.7	-4.1	-2.7	-3.5	-7.7	-5.3	-6.9	-7.9	-9.0
Light Template Contamination	<0.1	<0.1	<0.1	<0.1	<0.1	<0.1	<0.1	<0.1	<0.1
Muon ID	<0.1	<0.1	<0.1	<0.1	<0.1	<0.1	<0.1	<0.1	<0.1
Muon MS	<0.1	<0.1	<0.1	<0.1	<0.1	<0.1	<0.1	<0.1	<0.1
Muon Scale	<0.1	<0.1	<0.1	<0.1	<0.1	<0.1	<0.1	<0.1	<0.1
Pileup Offset Mu	<0.1	<0.1	0.1	<0.1	<0.1	<0.1	<0.1	<0.1	<0.1
Pileup Offset NPV	<0.1	<0.1	-0.1	<0.1	-0.1	<0.1	<0.1	<0.1	<0.1
Pileup Pt Term	<0.1	<0.1	<0.1	<0.1	<0.1	<0.1	<0.1	<0.1	<0.1
Pileup Rho Topology	<0.1	<0.1	0.1	<0.1	-0.1	<0.1	<0.1	<0.1	<0.1
SF to Inclusive	4.0	4.0	4.0	4.0	4.0	4.0	4.0	4.0	4.0
Template Statistics	-0.2	-0.1	0.1	0.2	-0.5	0.4	0.1	-0.7	-0.6
Simulation Statistics	14.2	14.0	11.5	8.1	8.7	7.7	6.3	5.0	4.8
Data Statistics	0.3	0.3	0.4	0.4	0.2	0.4	0.2	0.3	0.3
Total Systematics	15.0	15.1	12.5	9.8	12.3	10.2	10.2	10.2	11.0

Acronyms

ALFA **A**bsolute **L**uminosity **F**or **A**TLAS.

BCM **B**eam **C**onditions **M**onitor.

BDT **b**oosted **d**ecision **t**ree.

BR **b**ranching **r**atio.

BSM **B**eyond **S**tandard **M**odel.

BT **b**ack**t**ag.

CB **c**om**b**ined.

CC **C**harged **C**urrent.

CKM **C**abibbo-**K**obayashi-**M**askawa.

CSC **C**athode-**S**trip **C**hambers.

DAQ **D**ata **Aq**uisition.

EF **E**vent **F**ilter.

EM **e**lectro**m**agnetic.

FS **f**ull **s**can.

FSR **f**inal **s**tate **r**adiation.

GRL **g**ood **r**uns **l**ist.

HFAG **H**eavy **F**lavor **A**veraging **G**roup.

HLT **H**igh **L**evel **T**rigger.

IBL **I**nsertable **B**-**L**ayer.

ID **I**nner **D**etector.

IP **i**mpact **p**arameter.

ISR **I**nitial **S**tate **R**adiation.

JER **j**et **e**nergy **r**esolution.

JES **j**et **e**nergy **s**cale.

JVF **J**et **V**ertex **F**raction.

JVT **J**et **V**ertex **T**agger.

L1 **L**evel-**1**.

L2 **L**evel-**2**.

LAr liquid **ar**gon.

LC **l**ocally **c**alibrated.

LCW **l**ocal hadronic **c**ell **w**eighting.

LEP **L**arge **E**lectron **P**ositron Collider.

LHC **L**arge **H**adron **C**ollider.

LS1 **L**ong **S**hutdown period 1.

LUCID **Lu**minosity measurement using **C**erenkov **I**ntegrating **D**etector.

MC **M**onte **C**arlo.

MDT **M**onitored **D**rift **T**ube Chamber.

MET **m**issing $\boldsymbol{E_T}$.

MIP **m**inimal **i**onizing **p**article.

MS **M**uon **S**pectrometer.

NC **N**eutral **C**urrent.

NEWT **New T**racking.

NN **n**eural **n**etwork.

NP **n**uisance **p**arameter.

OP **o**perating **p**oint.

OS **o**pposite **s**ign.

PDF **P**arton **D**istribution **F**unction.

PS **P**roton **S**ynchrotron.

PSB **P**roton **S**ynchrotron **B**ooster.

PV **p**rimary **v**ertex.

QCD **q**uantum **c**hromo**d**ynamics.

QED **q**uantum **e**lectro**d**ynamics.

QFT **q**uantum **f**ield **t**heory.

ROC **r**eceiver **o**perating **c**haracteristic.

RoI **R**egion **o**f **I**nterest.

RPC **R**esistive **P**late **C**hamber.

SA **s**tand-**a**lone.

SCT **s**emi**c**onductor **t**racker.

SF **s**cale **f**actor.

SM **S**tandard **M**odel.

sMDT **s**mall-diameter **M**onitored **D**rift **T**ube Chambers.

SMT **s**oft **m**uon **t**agger.

SPS **S**uper **P**roton **S**ynchrotron.

SS **s**ame **s**ign.

ST **s**egment-**t**agged.

SV **s**econdary **v**ertex.

TDAQ **T**rigger and **D**ata **Aq**uisition.

TGC **T**hin **G**ap **C**hambers.

TMVA **T**oolkit for **M**ulti**v**ariate **A**nalysis.

TRT **T**ransition **R**adiation **T**racker.

vdM **v**an **d**er **M**eer.

VLQ **v**ector-**l**ike **q**uark.

ZDC **Z**ero-**D**egree **C**alorimeter.

List of Figures

List of Tables

Bibliography

[1] F. Englert and R. Brout. "Broken Symmetry and the Mass of Gauge Vector Mesons". *Phys. Rev. Lett.* 13 (9 Aug. 1964), pp. 321–323. DOI: 10.1103/PhysRevLett.13.321.

[2] P. W. Higgs. "Spontaneous Symmetry Breakdown without Massless Bosons". *Phys. Rev.* 145 (4 May 1966), pp. 1156–1163. DOI: 10.1103/PhysRev.145.1156.

[3] ATLAS Collaboration. "Observation of a new particle in the search for the Standard Model Higgs boson with the ATLAS detector at the LHC". *Physics Letters B* 716.1 (2012), pp. 1–29. DOI: 10.1016/j.physletb.2012.08.020.

[4] CMS Collaboration. "Observation of a new boson at a mass of 125 GeV with the CMS experiment at the LHC". *Physics Letters B* 716.1 (2012), pp. 30–61. DOI: 10.1016/j.physletb.2012.08.021.

[5] A. Denner et al. "Standard Model Higgs-Boson Branching Ratios with Uncertainties". *Eur. Phys. J.* C71 (2011), p. 1753. DOI: 10.1140/epjc/s10052-011-1753-8. arXiv: 1107.5909 [hep-ph].

[6] F. Abe et al. "Observation of Top Quark Production in $\overline{p}p$ Collisions with the Collider Detector at Fermilab". *Phys. Rev. Lett.* 74 (14 Apr. 1995), pp. 2626–2631. DOI: 10.1103/PhysRevLett.74.2626.

[7] S. Abachi et al. "Search for High Mass Top Quark Production in $p\overline{p}$ Collisions at $\sqrt{s} = 1.8$ TeV". *Phys. Rev. Lett.* 74 (13 Mar. 1995), pp. 2422–2426. DOI: 10.1103/PhysRevLett.74.2422.

[8] K. Kröninger and A. B. Meyer and P. Uwer. "Top-Quark Physics at the LHC". *The Large Hadron Collider: Harvest of Run 1*. Ed. by Schörner-Sadenius, Thomas. 2015, pp. 259–300. DOI: 10.1007/978-3-319-15001-7_7. arXiv: 1506.02800 [hep-ex].

[9] ATLAS Collaboration. "Search for production of vector-like quark pairs and of four top quarks in the lepton-plus-jets final state in pp collisions at $\sqrt{s} =$ 8 TeV with the ATLAS detector". *JHEP* 08 (2015), p. 105. DOI: 10.1007/JHEP08(2015)105. arXiv: 1505.04306 [hep-ex].

[10] A. Pich. "The Standard Model of Electroweak Interactions". *Proceedings, 18th European School for High-energy Physics (ESHEP 2010)*. 2012, pp. 1–50. arXiv: 1201.0537 [hep-ph].

[11] K. A. Olive et al. (Particle Data Group). "Review of Particle Physics". *Chin. Phys.* C38 (2014). 090001. DOI: 10.1088/1674-1137/38/9/090001.

[12] The Nobel Foundation. *"The Nobel Prize in Physics 2013"*. Retrieved from http://www.nobelprize.org/nobel_prizes/physics/laureates/2013/ on May 11, 2016.

[13] R. Placakyte. "Parton Distribution Functions". *Proceedings, 31st International Conference on Physics in collisions (PIC 2011)*. contribution 15. 2011. arXiv: 1111.5452 [hep-ph]. URL: https://inspirehep.net/record/954990.

[14] The Nobel Foundation. *"The Nobel Prize in Physics 2015"*. Retrieved from http://www.nobelprize.org/nobel_prizes/physics/laureates/2015/ on May 11, 2016.

[15] Y. Amhis et al. "Averages of b-hadron, c-hadron, and τ-lepton properties as of summer 2014" (2014). arXiv: 1412.7515 [hep-ex].

[16] CERN 2016. *website*. Retrieved from https://press.cern/press-releases/2016/07/cern-welcomes-romania-its-twenty-second-member-state on July 26, 2016.

[17] CERN 2016. *website*. Retrieved from http://home.cern/about/member-states on July 26, 2016.

[18] L. Evans and P. Bryant. "LHC Machine". *JINST* 3 (2008), S08001. DOI: 10.1088/1748-0221/3/08/S08001.

[19] J. Haffner. "The CERN accelerator complex. Complexe des accélérateurs du CERN". *OPEN-PHO-ACCEL-2013-056* (Oct. 2013). URL: https://cds.cern.ch/record/1621894.

[20] ATLAS Collaboration. "The ATLAS Experiment at the CERN Large Hadron Collider". *JINST* 3 (2008), S08003. DOI: 10.1088/1748-0221/3/08/S08003.

[21] ATLAS Collaboration. "ATLAS pixel detector electronics and sensors". *Journal of Instrumentation* 3.07 (2008), P07007. URL: http://stacks.iop.org/1748-0221/3/i=07/a=P07007.

[22] ATLAS Collaboration. "ATLAS Insertable B-Layer Technical Design Report". *ATLAS-TDR-19* (2010). URL: http://cds.cern.ch/record/1291633. Addendum, *ATLAS-TDR-19-ADD-1* (2012). URL: http://cds.cern.ch/record/1451888.

[23] ATLAS Collaboration. "Track Reconstruction Performance of the ATLAS Inner Detector at $\sqrt{s} = 13$ TeV". *ATL-PHYS-PUB-2015-018* (July 2015). URL: https://cds.cern.ch/record/2037683.

[24] A. Yamamoto et al. "The ATLAS central solenoid". *Nuclear Instruments and Methods in Physics Research Section A: Accelerators, Spectrometers, Detectors and Associated Equipment* 584.1 (2008), pp. 53–74. DOI: 10.1016/j.nima.2007.09.047.

[25] ATLAS Collaboration. "ATLAS central solenoid: Technical Design Report". *Technical Design Report ATLAS, ATLAS-TDR-9* (1997). URL: https://cds.cern.ch/record/331067.

[26] N. Nikiforou. "Performance of the ATLAS Liquid Argon Calorimeter after three years of LHC operation and plans for a future upgrade". *Proceedings, 3rd International Conference on Advancements in Nuclear Instrumentation Measurement Methods and their Applications (ANIMMA 2013)*. 2013. DOI: 10.1109/ANIMMA.2013.6728060. arXiv: 1306.6756 [physics.ins-det].

[27] J. P. Badiou et al. "ATLAS barrel toroid: Technical Design Report". *Technical Design Report ATLAS, ATLAS-TDR-7* (1997). URL: https://cds.cern.ch/record/331065.

[28] ATLAS Collaboration. "Measurement of the muon reconstruction performance of the ATLAS detector using 2011 and 2012 LHC proton–proton collision data". *The European Physical Journal C* 74.11 (2014), pp. 1–34. DOI: 10.1140/epjc/s10052-014-3130-x.

[29] C. Ferretti. "Upgrades Of The ATLAS Muon Spectrometer With sMDT Chambers". *ATL-MUON-SLIDE-2015-306* (June 2015). URL: https://cds.cern.ch/record/2021528.

[30] ATLAS Collaboration. "Improved luminosity determination in *pp* collisions at $\sqrt{s} = 7$ TeV using the ATLAS detector at the LHC". *Eur. Phys. J. C* 73 (2013), p. 2518. DOI: 10.1140/epjc/s10052-013-2518-3. arXiv: 1302.4393 [hep-ex].

[31] M. Backes. "The ATLAS Trigger System - Ready for Run-2". *ATL-DAQ-PROC-2015-041* (Oct. 2015). URL: https://cds.cern.ch/record/2058618.

[32] ATLAS Collaboration. "2015 start-up trigger menu and initial performance assessment of the ATLAS trigger using Run-2 data". *ATL-DAQ-PUB-2016-001* (Mar. 2016). URL: https://cds.cern.ch/record/2136007.

[33] ATLAS Collaboration. "Technical Design Report for the Phase-I Upgrade of the ATLAS TDAQ System". *CERN-LHCC-2013-018, ATLAS-TDR-023* (Sept. 2013). URL: https://cds.cern.ch/record/1602235.

[34] ATLAS Collaboration. "The performance of the jet trigger for the ATLAS detector during 2011 data taking". *CERN-EP-2016-031* (2016). arXiv: 1606.07759 [hep-ex].

[35] T. Cornelissen et al. "Concepts, Design and Implementation of the ATLAS New Tracking (NEWT)". *ATL-SOFT-PUB-2007-007, ATL-COM-SOFT-2007-002* (Mar. 2007). URL: https://cds.cern.ch/record/1020106.

[36] R. Frühwirth. "Application of Kalman filtering to track and vertex fitting". *Nucl. Instrum. Meth.* A262 (1987), pp. 444–450. DOI: 10.1016/0168-9002(87)90887-4.

[37] ATLAS Collaboration. "Early Inner Detector Tracking Performance in the 2015 Data at $\sqrt{s}$ = 13 TeV". *ATL-PHYS-PUB-2015-051* (2015). URL: http://cdsweb.cern.ch/record/2110140.

[38] ATLAS Collaboration. "Performance of primary vertex reconstruction in proton–proton collisions at $\sqrt{s}$ = 7 TeV in the ATLAS experiment". *ATLAS-CONF-2010-069* (2010). URL: http://cdsweb.cern.ch/record/1281344.

[39] R. Frühwirth et al. "Adaptive Vertex Fitting". *CMS-NOTE-2007-008* (Mar. 2007). URL: https://cds.cern.ch/record/1027031.

[40] A. Wildauer et al. "Update of primary vertex plots on 7 TeV data from 2011". *ATL-COM-PHYS-2011-571* (May 2011). URL: https://twiki.cern.ch/twiki/bin/view/AtlasPublic/InDetTrackingPerformanceApprovedPlots#Vertex_performance.

[41] S. Hageböck and E. von Toerne. "Medical Imaging Inspired Vertex Reconstruction at LHC". *Journal of Physics: Conference Series* 396.2 (2012). 022021. URL: http://stacks.iop.org/1742-6596/396/i=2/a=022021.

[42] ATLAS Collaboration. "Vertex Reconstruction Performance of the ATLAS Detector at $\sqrt{s}$ = 13 TeV". *ATL-PHYS-PUB-2015-026* (2015). URL: http://cdsweb.cern.ch/record/2037717.

[43] ATLAS Collaboration. "Expected Performance of the ATLAS Experiment - Detector, Trigger and Physics". *CERN-OPEN-2008-020* (2009). arXiv: 0901.0512 [hep-ex].

[44] W. Lampl et al. "Calorimeter Clustering Algorithms: Description and Performance". *ATL-LARG-PUB-2008-002* (Apr. 2008). URL: https://cds.cern.ch/record/1099735.

[45] ATLAS Collaboration. "Topological cell clustering in the ATLAS calorimeters and its performance in LHC Run 1". *CERN-PH-EP-2015-304* (2016). arXiv: 1603.02934 [hep-ex].

[46] ATLAS Collaboration. "Properties of jets and inputs to jet reconstruction and calibration with the ATLAS detector using proton–proton collisions at $\sqrt{s}$ =

13 TeV". *ATL-PHYS-PUB-2015-036* (2015). URL: http://cdsweb.cern.ch/record/2044564.

[47] ATLAS Collaboration. "The overview of the ATLAS local hadronic calibration". *Journal of Physics: Conference Series* 160 (2009). 012079. DOI: 10.1088/1742-6596/160/1/012079.

[48] M. Cacciari et al. "The anti-k_t jet clustering algorithm". *JHEP* 04 (2008), p. 063. DOI: 10.1088/1126-6708/2008/04/063. arXiv: 0802.1189 [hep-ph].

[49] ATLAS Collaboration. "Performance of pile-up mitigation techniques for jets in pp collisions at $\sqrt{s} = 8$ TeV using the ATLAS detector". *Eur. Phys. J.* C76.11 (2016), p. 581. DOI: 10.1140/epjc/s10052-016-4395-z. arXiv: 1510.03823 [hep-ex].

[50] ATLAS Collaboration. "Tagging and suppression of pileup jets with the ATLAS detector". *ATLAS-CONF-2014-018* (2014). URL: https://cds.cern.ch/record/1700870.

[51] ATLAS Collaboration. "Measurement of the muon reconstruction performance of the ATLAS detector using 2011 and 2012 LHC proton–proton collision data". *Eur. Phys. J. C* 74.11 (2014), pp. 1–34. DOI: 10.1140/epjc/s10052-014-3130-x. arXiv: 1407.3935 [hep-ex].

[52] ATLAS Collaboration. "Muon reconstruction performance of the ATLAS detector in proton–proton collision data at $\sqrt{s} = 13$ TeV". *CERN-EP-2016-033* (2016). arXiv: 1603.05598 [hep-ex].

[53] ATLAS Collaboration. "Standalone vertex finding in the ATLAS muon spectrometer". *JINST* 9 (2014), P02001. DOI: 10.1088/1748-0221/9/02/P02001. arXiv: 1311.7070 [physics.ins-det].

[54] T. Sjostrand et al. "A Brief Introduction to PYTHIA 8.1". *Comput. Phys. Commun.* 178 (2008), p. 852. DOI: 10.1016/j.cpc.2008.01.036. arXiv: 0710.3820 [hep-ph].

[55] D. J. Lange. "The EvtGen particle decay simulation package". *Nucl. Instrum. Meth.* A462 (2001), pp. 152–155. DOI: 10.1016/S0168-9002(01)00089-4.

[56] S. Agostinelli et al. "GEANT4: A Simulation toolkit". *Nucl. Instrum. Meth.* A506 (2003), pp. 250–303. DOI: 10.1016/S0168-9002(03)01368-8.

[57] H.-L. Lai et al. "New parton distributions for collider physics". *Phys. Rev.* D82.074024 (2010). DOI: 10.1103/PhysRevD.82.074024. arXiv: 1007.2241 [hep-ph].

[58] ATLAS colaboration. "Summary of ATLAS Pythia 8 tunes". *ATL-PHYS-PUB-2012-003* (Aug. 2012). URL: https://cds.cern.ch/record/1474107.

[59] R. D. Ball et al. "Parton distributions with LHC data". *Nucl. Phys.* B867 (2013), pp. 244–289. DOI: 10.1016/j.nuclphysb.2012.10.003. arXiv: 1207.1303 [hep-ph].

[60] S. Carrazza et al. "Parton Distributions and Event Generators". *Proceedings, 43rd International Symposium on Multiparticle Dynamics (ISMD 13)*. 2013, pp. 89–96. arXiv: 1311.5887 [hep-ph].

[61] A. Buckley. "ATLAS Pythia 8 tunes to 7 TeV data". *ATL-PHYS-PROC-2014-273* (Dec. 2014). URL: https://cds.cern.ch/record/1974411.

[62] Z. Marshall. "Re-defining the Standard QCD Di-Jet Samples". *ATL-COM-PHYS-2011-992* (July 2011). ATLAS internal. URL: https://cds.cern.ch/record/1370089.

[63] Z. Marshall. "Re-re-defining the Standard QCD Di-Jet Samples: Beginning to like event weights". *ATL-COM-PHYS-2015-417* (May 2015). ATLAS internal. URL: https://cds.cern.ch/record/2016630.

[64] ATLAS Collaboration. "Performance of b-Jet Identification in the ATLAS Experiment". *JINST* 11 (2016), P04008. DOI: 10.1088/1748-0221/11/04/P04008. arXiv: 1512.01094 [hep-ex].

[65] ATLAS Collaboration. "Performance of Impact Parameter-Based b-tagging Algorithms with the ATLAS Detector using Proton-Proton Collisions at $\sqrt{s} = 7\,\text{TeV}$". *ATLAS-CONF-2010-091* (2010). URL: https://cds.cern.ch/record/1299106.

[66] ATLAS Collaboration. "Performance of the ATLAS Secondary Vertex b-tagging Algorithm in 7 TeV Collision Data". *ATLAS-CONF-2010-042* (July 2010). URL: https://cds.cern.ch/record/1277682.

[67] ATLAS Collaboration. "Calibration of the performance of b-tagging for c and light-flavour jets in the 2012 ATLAS data". *ATLAS-CONF-2014-046* (July 2014). URL: https://cds.cern.ch/record/1741020.

[68] G. Piacquadio and C. Weiser. "A new inclusive secondary vertex algorithm for b-jet tagging in ATLAS". *Journal of Physics: Conference Series* 119.3 (2008). 032032. URL: http://stacks.iop.org/1742-6596/119/i=3/a=032032.

[69] ATLAS Collaboration. "Commissioning of the ATLAS high-performance b-tagging algorithms in the 7 TeV collision data". ATLAS-CONF-2011-102 (July 2011). URL: https://cds.cern.ch/record/1369219.

[70] A. Höcker et al. "TMVA - Toolkit for Multivariate Data Analysis with ROOT: Users guide". *CERN-OPEN-2007-007* (Mar. 2007). URL: https://cds.cern.ch/record/1019880.

[71] ATLAS Collaboration. "Expected performance of the ATLAS b-tagging algorithms in Run-2". *ATL-PHYS-PUB-2015-022* (July 2015). URL: https://cds.cern.ch/record/2037697.

[72] ATLAS Collaboration. "Optimisation of the ATLAS b-tagging performance for the 2016 LHC Run". *ATL-PHYS-PUB-2016-012* (June 2016). URL: https://cds.cern.ch/record/2160731.

[73] ATLAS Collaboration. "Performance of the ATLAS Trigger System in 2010". *Eur. Phys. J.* C72 (2012), p. 1849. DOI: 10.1140/epjc/s10052-011-1849-1. arXiv: 1110.1530 [hep-ex].

[74] V.M. Abazov et. al. "b-Jet identification in the D0 experiment". *Nuclear Instruments and Methods in Physics Research Section A: Accelerators, Spectrometers, Detectors and Associated Equipment* 620.2-3 (2010), pp. 490–517. DOI: 10.1016/j.nima.2010.03.118.

[75] ATLAS Collaboration. "b-Jet Tagging Efficiency Calibration using the System8 Method". *ATLAS-CONF-2011-143* (2011). URL: http://cds.cern.ch/record/1386703.

[76] ATLAS Collaboration. "Measurement of the b-tag Efficiency in a Sample of Jets Containing Muons with 5 fb^{-1} of Data from the ATLAS Detector". *ATLAS-CONF-2012-043* (Mar. 2012). URL: https://cds.cern.ch/record/1435197.

[77] ATLAS Collaboration. "Measuring the b-tag efficiency in a top-pair sample with 4.7 fb^{-1} of data from the ATLAS detector". *ATLAS-CONF-2012-097* (2012). URL: https://cds.cern.ch/record/1460443.

[78] ATLAS Collaboration. "Calibration of b-tagging using dileptonic top pair events in a combinatorial likelihood approach with the ATLAS experiment". *ATLAS-CONF-2014-004* (Feb. 2014). URL: https://cds.cern.ch/record/1664335.

[79] T. Aaltonen et.al. "Observation of the Production of a W Boson in Association with a Single Charm Quark". *Phys. Rev. Lett.* 110.071801 (7 Feb. 2013). DOI: 10.1103/PhysRevLett.110.071801.

[80] ATLAS Collaboration. "b-jet tagging calibration on c-jets containing D^{*+} mesons". *ATLAS-CONF-2012-039* (2012). URL: http://cds.cern.ch/record/1435193.

[81] ATLAS Collaboration. "Calibration of the performance of b-tagging for c and light-flavour jets in the 2012 ATLAS data". *ATLAS-CONF-2014-046* (2014). URL: https://cds.cern.ch/record/1741020.

[82] ATLAS Collaboration. "Measurement of the Mistag Rate with 5 fb^{-1} of Data Collected by the ATLAS Detector". *ATLAS-CONF-2012-040* (Mar. 2012). URL: https://cds.cern.ch/record/1435194.

[83] B. Lenzi et al. "TrackInCaloTools: A package for measuring muon energy loss and calorimetric isolation in ATLAS". *Journal of Physics: Conference Series* 219.3.032049 (2010). URL: http://stacks.iop.org/1742-6596/219/i=3/a=032049.

[84] ATLAS Collaboration. "Object selections for the SM VH and $A \to Zh$ search with V decaying leptonically and $h \to b\bar{b}$ with Run-2 data collected with the

ATLAS detector at $\sqrt{s} = 13$ TeV - Supporting Document -". ATL-COM-PHYS-2015-1467 (Dec. 2015). ATLAS internal. URL: https://cds.cern.ch/record/2110713.

[85] S. Greder. "Beauty quark tagging and cross-section measurement in Top quark pair production at $\sqrt{s} = 1.96$ TeV with the D0 experiment". PhD thesis. Louis Pasteur U., Strasbourg I, 2004. URL: https://inspirehep.net/record/665815.

[86] T. Wright. "B-Tagging at CDF and D0, lessons for LHC". *17th Symposium on Hadron Collider Physics 2006 (HCP 2006) Durham, North Carolina, May 22-26, 2006*. 2006. arXiv: 0707.1712 [hep-ex].

[87] F. Hirsch. "B-Tagging Calibration at the ATLAS Experiment". PhD thesis. Technische Universität Dortmund, 2011.

[88] C. Jung. "Measurement of the mass of the top quark using the transverse decay length and lepton transverse momentum techniques". PhD thesis. Technische Universität Dortmund, 2014. DOI: 10.17877/DE290R-780.

[89] H. Esch. "Measurement of the top quark mass in topologies enhanced with single top-quarks produced in the t-channel using flavour-tagging and a neural network with ATLAS data at $\sqrt{s} = 8$ TeV". PhD thesis. Technische Universität Dortmund, 2015. DOI: 10.17877/DE290R-6947.

[90] ATLAS Collaboration. "Jet energy resolution in proton-proton collisions at $\sqrt{s} = 7$ TeV recorded in 2010 with the ATLAS detector". *Eur. Phys. J.* C73.3 (2013), p. 2306. DOI: 10.1140/epjc/s10052-013-2306-0. arXiv: 1210.6210 [hep-ex].

[91] ATLAS Collaboration. "Jet energy measurement and its systematic uncertainty in proton-proton collisions at $\sqrt{s} = 7$ TeV with the ATLAS detector". *Eur. Phys. J.* C75 (2015), p. 17. DOI: 10.1140/epjc/s10052-014-3190-y. arXiv: 1406.0076 [hep-ex].

[92] ATLAS Collaboration. *Jet energy scale measurements and their systematic uncertainties in proton-proton collisions at $\sqrt{s} = 13$ TeV with the ATLAS detector.*

Tech. rep. ATL-COM-PHYS-2016-213. ATLAS internal. Geneva: CERN, Mar. 2016. URL: https://cds.cern.ch/record/2136864.

[93] K. Nakamura et al. (Particle Data Group). "Review of Particle Physics". *J. Phys. G* 37 (2010). 075021.

[94] J. Abdallah et al. "Determination of heavy quark non-perturbative parameters from spectral moments in semileptonic B decays". *Eur. Phys. J.* C45 (2006), pp. 35–59. DOI: 10.1140/epjc/s2005-02406-7. arXiv: hep-ex/0510024 [hep-ex].

[95] B. Aubert et al. "Measurement of the electron energy spectrum and its moments in inclusive $B \to Xe\nu$ decays". *Phys. Rev. D* 69.111104 (11 June 2004). DOI: 10.1103/PhysRevD.69.111104.

[96] A. H. Mahmood et al. "Measurement of lepton momentum moments in the decay $\overline{B} \to Xl\overline{\nu}$ and determination of the heavy quark expansion parameters and $|V_{cb}|$". *Phys. Rev. D* 67.072001 (7 Apr. 2003). DOI: 10.1103/PhysRevD.67.072001.

[97] CDF Collaboration. "Measurement of Ratios of Fragmentation Fractions for Bottom Hadrons in $p\bar{p}$ Collisions at $\sqrt{s} = 1.96$-TeV". *Phys. Rev.* D77.072003 (2008). DOI: 10.1103/PhysRevD.77.072003. arXiv: 0801.4375 [hep-ex].

[98] A. S. Bell. *Calibration of b-tagging using di-leptonic $t\bar{t}$ events produced in pp collisions at $\sqrt{s} = 13$ TeV and a combinatorial likelihood approach.* Tech. rep. ATL-COM-PHYS-2016-1598. ATLAS internal. Nov. 2016. URL: https://cds.cern.ch/record/2231568.

[99] D. Guest et al. *Identification of Jets Containing b-Hadrons with Recurrent Neural Networks at the ATLAS Experiment.* Tech. rep. ATL-COM-PHYS-2017-102. ATLAS internal. Feb. 2017. URL: https://cds.cern.ch/record/2244762.

Acknowledgment

At this point I want to seize the opportunity to express my gratitude towards all the people who supported me in various ways during my time in Dortmund and Geneva and during my work within E4 and the ATLAS Collaboration.

First of all I want to thank PD Dr. Reiner Klingenberg for all the support during this thesis. I really appreciate the time working together and I am grateful that you were always available for any kind of discussion, which always were incredibly enlightening and educative.

I also want to thank Dr. Johannes Albrecht and all members of the examination committee for agreeing to read and grade my thesis and attending my thesis defends.

During my time at E4, there were a lot of people I got the pleasure to work with. First I want to thank Prof. Dr. Claus Gößling for accepting me as a PhD candidate at E4 and giving me the chance to be a part of the ATLAS collaboration at CERN. And of course, I want to express my gratitude to Prof. Dr. Kevin Kröninger for not firing me (at least not too often). Special thanks also go to the unofficial head of the chair, Andrea Teichmann, for helping with all the organizational issues and always brighten up the atmosphere at work. In addition, I want to thank Markus Alex for keeping such good care of our IT infrastructure and helping with computing issues.

A lot of thanks also go to all members of the analyzers group at E4, which I had the pleasure to team up with. Most importantly I want to express my appreciation to my former colleagues Dr. Christian Jung and Dr. Hendrik Esch for the awesome time working together in Geneva and Dortmund and thanks a lot for all the help and for being so patient with me all the time. I am not only gracious for the great time at work, but also for all the time spent together after office. Another special thanks goes to Tobias Kupfer and Gregor Geßner for taking me in whenever I was in Geneva lately and for all the good times we have spent together. I also want to add Isabel Nitsche to this list and I am really happy that I recruited you all into joining the ATLAS analysis team. Things would not have been the same without you. But of course I also want to thank the rest of the analysis group. This of course includes our Post-Docs Dr. Johannes Erdmann and Dr. Diane Cinca for providing a nice atmosphere in the offices in Dortmund and Geneva, respectively. I also want to thank the rest of

the PhD candidates Michael Homann, Sonja Bartkowski and Elena Freundlich. Since I will probably forget half the people anyways I just want to thank all the students working with us during my time here. In addition, thanks go to Lennart Rustige for all the help provided especially on all the coding issues. Another special thanks belongs to Stella Oppermann on behalf of the "Kinderzimmer"-group for contributing a lot of good mood during their time at E4. Of course, there are a lot more people that work or have been working at E4 besides the ATLAS analysis group I want to thank for this awesome time.

This thesis would not have been possible without the colleagues of the ATLAS group. Special thanks go to Rachael Craeger for her support and for doing some of the really unpleasant work. I would also like to thank Dr. Bingxuan Liu for his help during the most busy phase of the analysis. Also thanks to Prof. Dr. Joseph Kroll for a lot of inspiring discussions. Let me also add Prof. Dr. Marjorie Shapiro and Prof. Dr. James Mueller for all the fruitful discussions especially in the final steps of the analysis. I would also like to thank Dr. Kristian Gregersen on behalf of all the ATLAS flavor tagging group. Finally, I also want to express my gratitude to all the other colleagues working within ATLAS, without whom all this would not have been possible.

At this point, I would also like to add special thanks to all my friends that are not involved in my work life for being such an incredible support all the time. Except for Dr. Kai Walter. You clearly planed your wedding during this final time of my thesis to mess up my schedule. So, thanks for that. I also love to express my appreciation to Dr. Patrick Dedie, Robin Dedie, Jan Schulze Köhling, Robert Wolffgang and Patrick Thöne. Again, I probably forget a lot of people at this point, so big thanks to everyone who accompanied me during this time.

Last but not least, I want to express my gratefulness to my family. Very special thanks to my parents, who supported me in every way. Thanks also to my brother Thorsten Burmeister, who always provided me with steak, when I was visiting DESY for a conference or science school. And of course, thanks to my aunt Heike Burmeister for all the support and for being available for phone talks whenever I needed to keep my mind of work for some time.